

The Turbulent Magnetohydrodynamic Cascade:
Applications of Third-Moment Theory
to the Solar Wind at 1 AU

Joshua E. Stawarz
Department of Physics
University of New Hampshire
Durham, NH 03824

May 27, 2011

Abstract

Velocity and magnetic field fluctuations in the solar wind show evidence that non-linear turbulent dynamics are present in the interplanetary medium. The cascade of energy created by these turbulent processes may provide a mechanism for in situ heating of the solar wind plasma. We perform three studies analyzing the turbulent energy cascade at 1 AU using 10 years of data from the Advanced Composition Explorer spacecraft. These studies employ magnetohydrodynamic analogues to traditional hydrodynamic third-moment expressions.

In the first analysis, we compute energy cascade rates and compare them to proton heating rates as inferred from the radial gradient of the solar wind proton temperature. We find good agreement between energy cascade rates and proton heating rates. There is a moderate excess of energy in the cascade ($\sim 25\text{--}50\%$) which is consistent with previous estimates for thermal electron heating in the solar wind.

In the second analysis, we apply third-moment theory to compute energy cascade rates as a function of the normalized cross-helicity. We find, in contrast to intervals of smaller cross-helicity forming the bulk of the observations, large cross-helicity intervals experience a significant back-transfer of energy from small to large scales. This occurs in such a way as to reinforce the dominance of outward-propagating fluctuations. We conclude this back-transfer process must be a short-lived, transient phenomena in order to be in keeping with solar wind observations.

Finally, we extend newly developed magnetohydrodynamic third-moment expressions, which take into account the effects of large-scale velocity shear, to the solar wind. Limited success is achieved with the new formalism when applied to solar wind data. The best agreement is found for rarefaction intervals where the solar wind speed is decreasing as it passes the spacecraft. We find that cascade rates increase with increasing shear magnitude and that only a small amount of shear induced anisotropy is necessary to be consistent with proton heating rates. We conclude the shear formalism is necessary when analyzing data with a persistent shear of a single sign, but unnecessary when considering equal amounts of positive and negative shear.

Contents

1	Introduction	3
2	The Solar Wind	5
2.1	Solar Wind Overview	5
2.2	The Solar Cycle	6
2.3	Heliospheric Missions	8
2.4	The Advanced Composition Explorer	9
3	Solar Wind Structures and Transients	11
3.1	Coronal Mass Ejections	11
3.2	Shocks	15
3.3	The Interplanetary Magnetic Field	15
3.4	The MHD Equations	16
3.5	The Parker Spiral	18
3.6	Waves in Interplanetary Space	20
3.7	Solar Wind Heating	23
4	Solar Wind Turbulence	25
4.1	Interplanetary Power Spectra	25
4.2	Energy-Containing Range	26
4.3	Inertial Range Spectra	30
4.4	Dissipation Range Spectra	32
4.5	Problems	33
5	Third-Moment Theory	35
5.1	Hydrodynamic Third-Moment Theory	35
5.2	Isotropic MHD Third-Moment Theory	38
5.2.1	Isotropic Application to the Solar Wind	39
5.3	Anisotropic MHD Third-Moment Theory	39
5.3.1	Anisotropic Application to the Solar Wind	41
6	Early Third-Moment Applications in the Solar Wind	43
6.1	MacBride et al. 2005	43
6.2	MacBride et al. 2008	45
7	Advanced Heating Test	51
7.1	Convergence of Third-Order Structure Functions	51
7.2	Energy Cascade vs. Heating Rates	54

7.3	Heating Discussion	56
7.3.1	A Small Correction	60
8	High Cross-Helicity	61
8.1	Cross-Helicity	61
8.2	Isotropic Analysis	62
8.3	Hybrid Analysis	67
8.4	Selecting for Heating Rate	73
8.5	Solar Minimum	75
8.6	Cross-Helicity Discussion	78
9	Large-Scale Velocity Shear	81
9.1	Theoretical Approach to Large-Scale Velocity Shear	81
9.1.1	Velocity Shear in Hydrodynamic Third-Moments	82
9.1.2	Velocity Shear in MHD Third-Moments	85
9.1.3	Application of Velocity Shear Formalism to the Solar Wind	86
9.2	Shear Analyses	90
9.2.1	Sorting Results by Local Velocity Shear	91
9.2.2	Sorting Results by $\mathbf{V_{sw}T_P}$	98
9.3	Velocity Shear Discussion	101
10	Summary	102

Acknowledgements:

I would like to give a special thanks to Prof. Charles W. Smith, who first introduced me to the field of magnetohydrodynamic turbulence and who has worked with me over the past three years on the research projects presented herein. I also appreciate the opportunities I have had over the course of performing this research to work with Prof. Bernard J. Vasquez, here at the University of New Hampshire, and Prof. Miriam A. Forman at the State University of New York at Stony Brook. I would also like to thank my Mom, Dad, Brother, and Fiancée, who have always supported me in my educational endeavors (even when they didn't fully understand the work I was doing).

Preamble:

This thesis is the culmination of three years of research that I have performed under the supervision of Prof. Charles W. Smith while perusing my undergraduate degree in physics at the University of New Hampshire. This research builds on the work of former University of New Hampshire physics undergraduate, Benjamin T. MacBride (see Chapter 6). I inherited the code used by Benjamin MacBride to compute third-moments and evolved it for use in several studies. This research has resulted in the publication of three papers, on which I have been first author (Stawarz et al., 2009, 2010, 2011). These studies form the basis of this thesis. I have also been co-author on four additional journal articles or conference proceedings and am preparing to attend my third Solar Heliospheric and Interplanetary Environment (SHINE) conference. This conference has afforded me the opportunity to present my research to others in the field and broaden my understanding of space physics.

This thesis relates to magnetohydrodynamic turbulence in the space physics setting. Over the course of performing my research and writing this thesis, several books have provided particularly useful background knowledge. Kivelson and Russell (1995) provides an overview on a variety of space plasma physics topics, including the magnetohydrodynamic equations, the structure of the solar wind, and wave damping phenomena. Frisch (1995) and Pope (2000) provide detailed descriptions of turbulence concepts as they pertain to hydrodynamics. Biskamp (2003) details the concepts of magnetohydrodynamic turbulence. Smith (2009) also provides an overview of turbulence concepts and their applications in the solar wind. I refer the reader to these references for further reading on the topics discussed in this thesis.

Funding for this work was provided, in part, by Caltech subcontract 44A1085631 to the University of New Hampshire in support of the ACE/MAG instrument and by NASA Sun-Earth Connection Guest Investigator grants NNX08AJ19G and NNX09AG28G. Additional support was obtained by NSF SHINE grant ATM0850705 and NASA Solar and Heliospheric Physics SRT grants NNX07AI14G and NNX10AC18G.

Chapter 1

Introduction

This thesis pursues the ideas of hydrodynamic turbulence theory as they are extended to include magneto-dynamics and the magnetohydrodynamic (MHD) equations. We apply these concepts to the solar wind, a supersonic gas of electrically charged particles that fills interplanetary space. In essence, the solar wind forms the perfect MHD wind tunnel to the extent that any such system exists: There is a localized source, vast room to evolve, and sensors (called spacecraft) placed at various points in the system.

A turbulent system is created through the non-linear interactions between fluctuations within a fluid flow and is characterized by the movement of energy in a conservative fashion from large to small scales. This concept is known as the “cascade” of energy. We focus on third-moment theory (Kolmogorov, 1941b; Politano and Pouquet, 1998a,b), which provides one of the few “exact” relationships in the field of turbulence. Third-moment theory has a long standing history in hydrodynamics and allows one to compute the rate of energy cascade in a turbulent system. The exploration of the MHD analogues to these expressions, as they pertain to the solar wind, form the basis of the analyses within this thesis.

Turbulence plays a significant role in understanding the dynamics of the solar wind. Observations show in situ heating is present as the solar wind plasma expands from the Sun. The ultimate fate of cascading energy, when it reaches the smallest scales in the turbulent system, is dissipation into heat. It is, therefore, suggested that turbulence can provide sufficient energy to account for the observed heating in the solar wind. In this thesis, we utilize third-moment theory to explore this problem, as well as, to build a deeper, fundamental understanding of the magnetohydrodynamic turbulence present in the solar wind.

In Chapter 2, we provide a broad context for the analyses described in this thesis. We discuss the basic nature of the solar wind as a fast moving flow of plasma emanating from the Sun. The solar wind is a dynamic and variable environment and we begin a discussion of this variability by considering the solar activity cycle. We also discuss the variety of spacecraft that make in situ measurements of the solar wind, including the Advanced Composition Explorer which provides the plasma and magnetic field measurements used in our analyses.

In Chapter 3, we continue the examination of the variability of the solar wind in greater detail. We consider transient phenomena, such as coronal mass ejections and shocks, which are outside the scope of the theories we aim to analyze and must be removed from the solar wind data. We also consider the variability and large-scale structure of the Interplanetary Magnetic Field (IMF) and discuss the magnetohydrodynamic description of a plasma, which gives rise to wave phenomena and turbulence in the solar wind. We finally consider the in

situ heating of the solar wind protons.

Chapter 4 provides an overview of turbulence concepts from an observational viewpoint. Drawing from well understood hydrodynamic concepts, we consider the three major sub-ranges of the power spectrum in a turbulent system and discuss the dynamics that are believed to be important in each range. These sub-ranges include: 1) energy-containing range, where the large-scale fluctuations that drive the turbulence are generated, 2) the inertial range, where energy cascades from large-scale fluctuations to small-scale fluctuations, and 3) the dissipation range, where turbulent energy is finally dissipated into heat. In doing this, we develop a picture of interplanetary turbulence.

In Chapter 5, we examine the derivation of the third-moment expressions, which are the main focus of this thesis. These third-moments are generalizations of third-order structure functions and arise from rigorous derivations of turbulent dynamics. We consider both hydrodynamic and magnetohydrodynamic third-moment theories and discuss the modifications needed to apply them to the solar wind.

Chapter 6 discusses two early applications of third-moment theory to the solar wind by MacBride et al. (2005) and MacBride et al. (2008). These analyses reveal cascade rates in general agreement with solar wind heating rates and provide evidence for the evolution of solar wind turbulence to a 2D geometry, which is expected by many authors. The MacBride et al. (2005, 2008) analyses form the basis of our third-moment studies.

Chapters 7–9 outline the three main analyses of this thesis. In Chapter 7, we first refine the error analysis techniques used in previous solar wind third-moment analyses in order to examine the convergence of third-moment expressions in the solar wind. We find results that are in keeping with the analysis of Podesta et al. (2009) and demonstrate one of the major limitations of third-moment analysis: the large amount of data required to converge to a statistically significant result. In Chapter 7, we also perform an in depth comparison between proton heating rates in the solar wind and turbulent energy cascade rates. We find compelling evidence that there is enough energy present in the turbulent cascade to heat both solar wind protons and electrons.

In Chapter 8, we attempt to better understand the nature of MHD turbulence, by using third-moments to examine the dependence of the energy cascade rate on cross-helicity. The cross-helicity provides a quantitative measure of the degree of correlation between magnetic and velocity fluctuations and, in turbulence theory, acts as a “throttling” mechanism for the energy cascade. We find the expected general decrease in the cascade rate with increasing cross-helicity; however, at high cross-helicities we observe an unexpected back-transfer of energy from small to large-scales.

Wan et al. (2009) criticize the results of Chapters 7 and 8, arguing they do not take into account the large-scale shears present in the solar wind. They draw on hydrodynamic concepts to develop a third-moment-like MHD formalism, which involves two additional terms describing the effects a linear velocity shear has on the cascade. In Chapter 9, we review the concepts, in both hydrodynamics and MHD, involved in developing a third-moment shear formalism. We develop a basic model to apply these concepts to the solar wind and perform a preliminary analysis of Advanced Composition Explorer data. We conclude that while the velocity shear formalism is necessary when considering data with a single shear direction, the results of Chapters 7 and 8, which consider both increases and decreases in solar wind speed, are still valid.

Chapter 10 summarizes our results.

Chapter 2

The Solar Wind

In order to provide a context for our studies of magnetohydrodynamic turbulence, we describe the solar wind environment in which the turbulence evolves. The solar wind is a super-sonic and super-Alfvénic (see Section 3.6) flow of plasma emanating in all directions and at all times from the Sun. The solar wind is affected by the dynamics at its source (the Sun) and, as such, we briefly discuss the solar activity cycle. Numerous spacecraft have been launched to study this environment, providing a wealth of data. Several of these spacecraft are discussed here, including the Advanced Composition Explorer which is extensively used in this thesis.

2.1 Solar Wind Overview

Astronomical studies of near-Earth objects prior to the start of the space age gave hints that there did exist some form of corpuscular radiation within interplanetary space. At the very least, there seemed to be such material and dynamics at times of solar activity (flares, in particular). As early as the 1700’s, it was suspected that aurora were linked with solar activity in some fashion and, in particular, the periods of heightened sunspot numbers. However, direct evidence for this link to the Sun was not obtained until Richard Carrington’s landmark observation of a solar flare on September 1, 1859. This burst of radiation was followed 18 hrs later by brilliant aurora and one of the strongest geomagnetic storms ever recorded (Kivelson and Russell, 1995). This observation lent support to the idea that charged material was ejected from the Sun during these active periods. In the mid-1900s, it was observed that the orientation of cometary tails could be attributed to the presence of a “solar wind” of particles emanating in all directions and at all times from the Sun. In addition, it was observed that cometary tails could become disconnected by some unknown means acting in interplanetary space. Not long after, Parker (1958) provided the current theoretical understanding of the mechanisms producing this “wind” of charged particles.

The earliest missions of the space age explored the very-near-Earth region now known as the magnetosphere, where the Earth’s magnetic field dominates the structure and dynamics of space. Several key early missions opened the door to interplanetary space. The Russian spacecraft Luna 1 in 1959¹ and the American spacecraft Mariner 2 in 1962 (Neugebauer and Snyder, 1962) provided the first measurements of an apparent supersonic flow of ions moving

¹<http://nssdc.gsfc.nasa.gov/nmc/masterCatalog.do?sc=1959-012A>

away from the Sun. This flow is now known as the solar wind. In 1960, Pioneer 5 (Coleman et al., 1960) provided the first measurements of the IMF and confirmed the prediction of Parker (1958, 1963) that the IMF was wound into a spiral pattern and rooted in the solar photosphere.

Many missions have flown since. We have explored the high latitudes above the Sun and reached the distant outer heliosphere where the solar wind meets the interstellar plasma. We have found the solar wind to be quite variable, but never absent. Barnes (1979) characterizes the low-speed and high-speed wind at 1 AU, as well as, the variation of several parameters with heliocentric distance R . Reproducing some of Table 1 from Barnes (1979):

Table 2.1: Partial Table 1 from Barnes (1979) showing typical solar wind properties at 1 AU.

Measured Parameter	Typical 1 AU Value	High-speed streams	Variation with R
Ion Composition	$\sim 96\% \text{ H}^+$	$\sim 96\% \text{ H}^+$	Constant
	$\sim 4\% \text{ He}^{2+}$	$\sim 4\% \text{ He}^{2+}$	
Flow Velocity	$\sim 400 \text{ km/s}$	$\sim 750 \text{ km/s}$	Constant
	radially directed	radially directed	
Density	$\sim 6 \text{ proton/cm}^3$	$\sim 4 \text{ protons/cm}^3$	$\propto R^{-2}$
Magnetic Field	$\sim 5 \times 10^{-5} \text{ G}$??	radial
	oriented in		component $\propto R^{-2}$
	ecliptic plane at		azimuthal
	about 45° to		component $\propto R^{-1}$
	radial direction		
Proton Temperature	$\sim 4\text{--}10 \times 10^4 \text{ K}$	$\sim 2 \times 10^5 \text{ K}$	$\propto R^{-a}, 2/7 \leq a \leq 4/3$
Electron Temperature	$\sim 10\text{--}20 \times 10^4 \text{ K}$	$\sim 10^5 \text{ K}$	$\propto R^{-b}, 2/7 < b \leq 4/3$

Many of the values above have been further illuminated in more recent studies and are pursued below. The Sun has been shown to be highly variable, but on long time scales highly systematic passing through periods of greater or lesser activity. There is strong latitudinal structure to the solar wind and numerous evolutionary developments in the outer heliosphere as fast and slow wind collide. We discuss these topics in Section 2.2 and Chapter 3 as they pertain to the central theme of this thesis.

2.2 The Solar Cycle

The solar cycle plays a minor role in the work to come, so we briefly discuss it now. The Sun goes through an 11 yr cycle of activity from peak activity (solar maximum) to remarkably quiet conditions (solar minimum). “Activity” and “quiet” refer largely to photospheric dynamics where sunspots form, flares erupt, etc. Some activity, such as interplanetary shocks reach out into interplanetary space and have a direct influence on in situ conditions. Figure 2.1 shows a fairly typical image of the active Sun at solar maximum as observed by the Solar and Heliospheric Observatory (SOHO) spacecraft. Figure 2.2 shows a typical image of the Sun at solar minimum from the SOHO spacecraft. Notice the stark difference in the amount of bright active regions between the two images. Both images are taken from

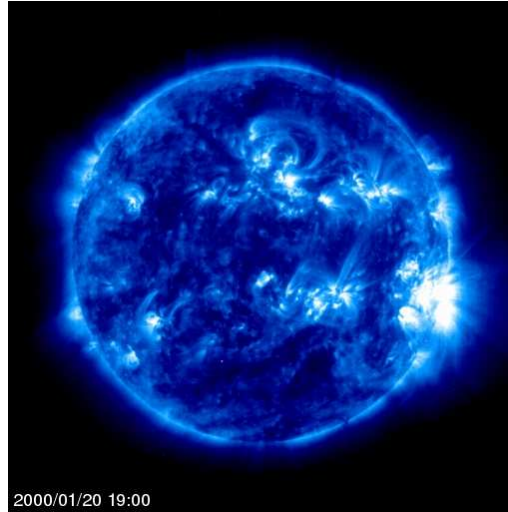


Figure 2.1: Image of the Sun recorded by the SOHO spacecraft on January 20, 2000. The image shows the Sun near solar maximum and a number of bright active regions are apparent. The image was taken by the Extreme Ultraviolet Imaging Telescope (EIT) at a wavelength of 171 \AA .

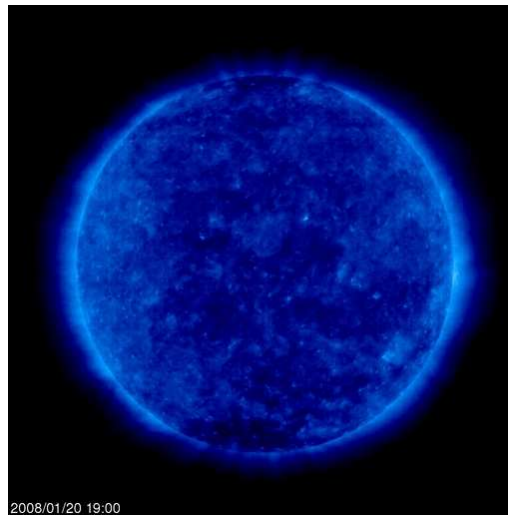


Figure 2.2: Same as the image from Figure 2.1 but recorded on January 20, 2008. This data is near solar minimum. Notice the absence of bright active regions as compared to Figure 2.1.

the SOHO website².

During solar minimum, the Sun and solar wind are highly structured. Two large coronal holes dominate the Sun's photosphere and these holes are a source of high-speed winds seen predominantly and most notably at high heliographic latitudes. These high-speed winds can extend to low latitudes such that during solar minimum the near-ecliptic wind is a variation between fast and slow-wind conditions. This produces Interaction Regions where the fast wind impinges on the slow wind and compresses the flow. As there is little other solar activity and these wind sources are long-lived, the interaction regions can be seen periodically each solar rotation, making them Corotating Interaction Regions (CIRs).

During solar maximum the Sun and solar wind are disordered. Transient activity defines the observations with many solar eruptions, flares, etc. The solar wind shows highly transient behavior and the high-latitude wind is largely similar to the low-latitude wind. Notably present during solar maximum are Coronal Mass Ejections (CMEs) which are large eruptions of solar material that plow through the surrounding solar wind at high speeds. These eruptions can create shocks in interplanetary space and drive geomagnetic activity, such as the aurora discussed above, making solar maximum an active period throughout the heliosphere.

The solar maximum phase is created by the reversal of the solar dynamo and its effects on the solar photosphere and corona. As such, the solar magnetic field possesses a 22 yr cycle spanning two 11 yr cycles in activity. In general, the Sun's magnetic field is nearly dipolar, reversing polarity every 11 yrs. The most "pure" dipolar structure is observed during solar minimum and the structure becomes more complex as solar maximum approaches. Overall, open magnetic flux dominates the polar regions of the Sun and extends to the edges of the heliosphere, while the equatorial regions are dominated by closed magnetic loop structures near the solar photosphere. In the hemisphere where magnetic field lines emanate from the Sun, interplanetary space is dominated by outward directed field lines. Likewise, in the hemisphere where field lines are directed towards the Sun, interplanetary space is dominated by inward directed field lines. Further details of the Sun's magnetic field structure are discussed in the next chapter.

2.3 Heliospheric Missions

Many spacecraft have made direct measurements of the solar wind and heliospheric environment since the early 1960's, providing a variety of in situ measurements at various positions. Measurements are available ranging from the near-Earth environment of the magnetosphere to the termination shock at the edge of the heliosphere. There are direct measurements as close as 0.3 AU from the Sun (and even closer in the near future with the launch of Solar Probe). Many measurements are available in the ecliptic plane (in which the planets revolve around the Sun), while only four have ventured outside the ecliptic region: Ulysses, Pioneer 11, and Voyagers 1 & 2. The latter moved to high northern and southern latitudes only after completing their planetary encounters. Ulysses is fundamentally and by design a high-latitude mission.

A multitude of missions, since the early days of space flight, have made measurements in the near-Earth solar wind environment. The data from many of these missions has been

²<http://sohowww.nascom.nasa.gov/>

merged into the National Space Science Data Center (NSSDC) Omni dataset³, first created in the mid-1970's, which provides a unique 30+ years of continuous data.

The Voyager 1 & 2 missions⁴, launched in 1977, provide solar wind measurements well into the outer heliosphere. The Voyagers were more extensively instrumented than the Pioneer 10 & 11 spacecraft⁵, launched in 1972 and 1973 respectively. They followed the Pioneers to Jupiter, where Pioneer 10 was redirected across the inner heliosphere. The Voyagers followed Pioneer 11 to Saturn, where Pioneer 11 was directed out of the ecliptic. Voyager 1 was likewise directed out of the ecliptic after its encounter with Saturn, but in the opposite latitudinal direction. Voyager 2 was the first spacecraft to reach Uranus and Neptune and, was soon after, also redirected out of the ecliptic. The Pioneer 10 & 11 spacecraft died late in the last century due to a lack of electrical power; however, the Voyagers have lived on and provide us with the only in situ measurements of the termination region where the solar wind becomes sub-Alfvénic near the edge of the heliosphere. These three missions (Pioneer 11, Voyager 1, and Voyager 2) provide the only view of the high latitudes at large heliocentric distance and only at modest latitudes ~ 30 to 40° .

The Ulysses spacecraft was launched in 1990 and following a close encounter with Jupiter was swung by gravitational assist Sunward to pass over the Sun's south pole (Wenzel et al., 1992). It reached a highest latitude of 80° and completed 3 passes before losing power and ceasing communication in June of 2009. Ulysses provided the first direct evidence of the existence of a steady fast wind at high latitudes during solar minimum (McComas et al., 1995).

2.4 The Advanced Composition Explorer

The analyses described in Chapters 6–9 of this thesis utilize data from the Advanced Composition Explorer (ACE) spacecraft (Stone et al., 1998). The ACE spacecraft orbits around the L1 Lagrangian point of the Sun-Earth system. This selection of orbit means the spacecraft remains at an approximately stationary position between the Sun and the Earth relative to the motion of the two bodies. The L1 point is located $\sim 1.5 \times 10^6$ km towards the Sun from the Earth which puts the spacecraft approximately 1 AU (1.5×10^8 km) away from the Sun.

The spacecraft was launched in 1997 and data collection began on January 21, 1998. Magnetic field data collection began just a few hours after launch. The ACE data set, therefore, provides nearly continuous coverage of the near-Earth solar wind environment for more than 13 years. This data spans a variety of solar wind conditions during both solar maximum and solar minimum. The spacecraft continues to collect data as of today.

The primary objective of the ACE spacecraft is to measure the elemental and ion composition of energetic particles from a variety of sources (i.e. Solar Energetic Particles, Anomalous Cosmic Rays, and Galactic Cosmic Rays), as well as, the composition of the solar wind plasma. The position of the spacecraft between the Sun and the Earth also makes ACE an ideal platform for monitoring the solar wind for space weather purposes. As such, the spacecraft provides real-time in situ measurements of the solar wind plasma and interplanetary magnetic field. Nearly continuous plasma and magnetic field measurements also makes ACE data ideal for solar wind turbulence studies. Nine scientific instruments designed to achieve

³<http://omniweb.gsfc.nasa.gov/ow.html>

⁴<http://voyager.jpl.nasa.gov/>

⁵http://www.nasa.gov/mission_pages/pioneer/

these objectives are carried on ACE.

The two instruments most pertinent to turbulence studies, and utilized in the analyses presented in this thesis, are the Solar Wind Electron Proton Alpha Monitor (SWEPAM) and the ACE Magnetic Fields Experiment (MAG) (McComas et al., 1998; Smith et al., 1998). The SWEPAM instrument is the refurbished spare for the Solar Wind Over the Poles of the Sun (SWOOPS) instrument from the Ulysses spacecraft. It consists of two electrostatic analyzers, one for ions and the other for electrons, which make 3D measurements of protons, electrons, and alpha particles every 64s. The MAG instrument is the refurbished spare of the Magnetic Field Investigation (MFI) instrument on the WIND spacecraft consisting of two triads of fluxgate magnetometers. Each triad of fluxgates is arranged in an orthogonal fashion along three axes and is capable of producing 24 vector measurements of the magnetic field every second.

SWEPAM plasma and MAG magnetic field data are provided in a merged dataset with 64s resolution. The data is available online to all at the ACE Science Center⁶. The cadence of the data is limited by the measurement rate of the SWEPAM instrument. Data from the MAG instrument are averaged over the 64s interval of the SWEPAM measurement. In this dataset, relevant plasma data include the proton number density, proton temperature, proton speed, and the proton velocity components in RTN coordinates. Relevant magnetic field data include the magnetic field strength and components of the magnetic field in RTN coordinates.

The RTN coordinate system is defined such that $\hat{\mathbf{R}}$ is the direction radially away from the Sun, $\hat{\mathbf{T}}$ is coplanar with the Sun's rotational equator and pointed in the direction of the Sun's rotation, and $\hat{\mathbf{N}}$ is orthogonal to both $\hat{\mathbf{R}}$ and $\hat{\mathbf{T}}$ so that $\hat{\mathbf{R}} \times \hat{\mathbf{T}} = \hat{\mathbf{N}}$. The RTN coordinate system is used extensively in this thesis.

⁶<http://www.srl.caltech.edu/ACE/ASC/>

Chapter 3

Solar Wind Structures and Transients

As we allude to above, the solar wind is highly variable in many parameters. It has a single source, the Sun, but many smaller, localized sources on the Sun that produce different forms of wind (variable wind speed, density, magnetic field intensity, composition, etc.). This chapter briefly describes some of the in situ dynamics that are seen to be active in the solar wind. We describe them so that they may either be used or discarded as needed in the studies to come.

3.1 Coronal Mass Ejections

Many transient structures are present in the solar wind and several of these exhibit conditions that are unsuited for the analyses described in Chapters 7–9. One such structure is the Interplanetary Coronal Mass Ejection (ICME). ICMEs form as bubble-like disturbances in the solar corona known as Coronal Mass Ejections (CMEs). When these disturbances magnetically detach from the Sun, creating a closed magnetic loop, they are ejected into interplanetary space and become known as ICMEs. These structures have strong magnetic signatures, often including twisted magnetic field lines known as flux ropes (or magnetic clouds in interplanetary space) (Moldwin et al., 2009).

ICMEs are observed frequently in spacecraft data; occurring more frequently at solar maximum and less frequently at solar minimum. Figure 3.1 shows an example of two consecutive ICMEs observed by the ACE spacecraft during solar maximum. These two structures are seen beginning on days 274 and 277 of the plot. Rotations in the magnetic field indicating flux ropes can be seen in the second panel of the figure.

ICMEs travel at speeds that are often much larger than the surrounding solar wind speed and, as such, plow through the slower moving plasma creating shocks (see next section) upstream of the disturbance. One such shock is seen in Figure 3.1 on day 277 and is discussed in the next section. The shock associated with the ICME on day 274 is missing density data, which makes it difficult to pinpoint. The variability of the magnetic field and compressive nature of the associated shocks, make these objects difficult to include in the turbulence formalism described in this thesis.

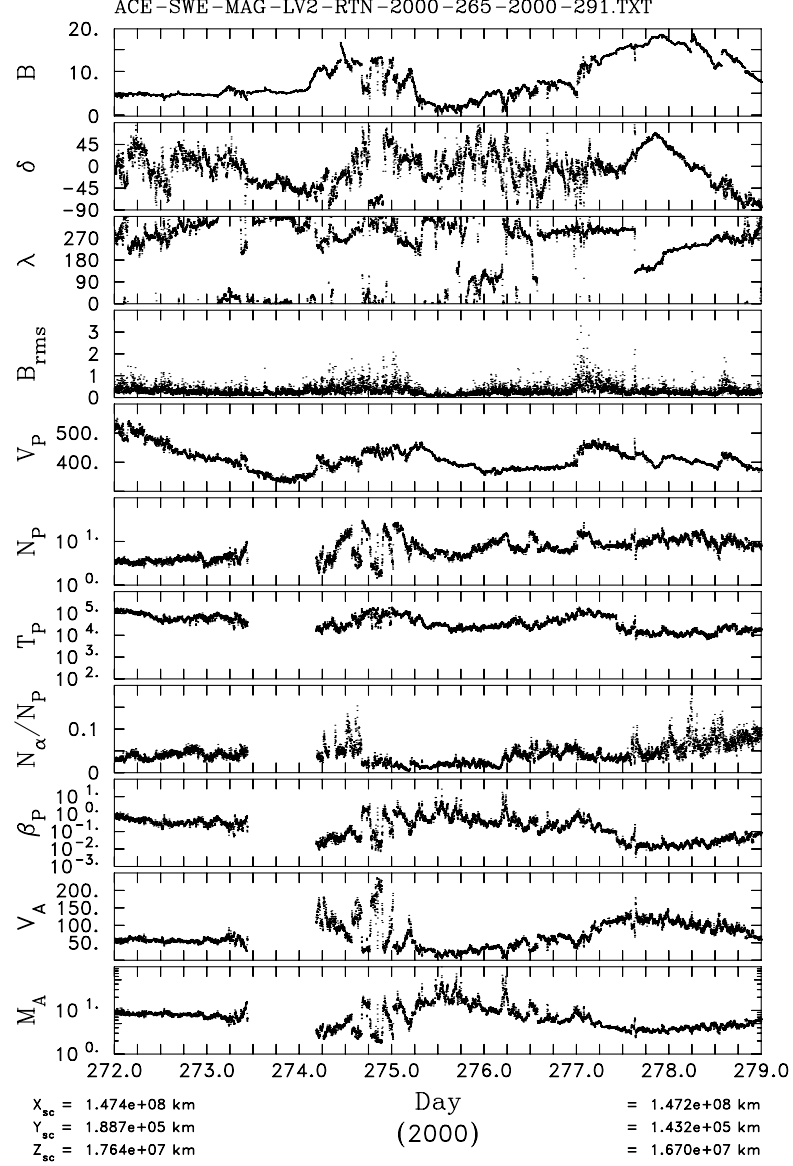


Figure 3.1: (from the top) Magnetic field intensity [nT], magnetic latitude angle [deg], magnetic longitude angle [deg], rms magnetic vector fluctuation based on a 16 s mean [nT], solar wind speed [km/s], proton density [$\#/\text{cm}^3$], proton temperature [K], alpha particle density [N_α/N_p], proton plasma beta ($\beta = 2\mu_0 N_p k_B T_p / B^2$), Alfvén speed ($V_A = B_0 / \sqrt{(\mu_0 \rho)}$) [km/s], and Mach number for the flow (V_p/V_A) as recorded by the ACE spacecraft from days 272 through 278 in year 2000. Note two ICMEs from day 274 to 275.5 and from day 277 until later than the plot shows. Note interplanetary shock ahead of second ICME at the start of day 277. An earlier shock is apparent shortly after the start of day 274, but the shock lacks density and temperature information. Note strong rotations of the IMF (flux ropes) within both ICMEs with the second particularly evident. Last, note extreme variability of all parameters.

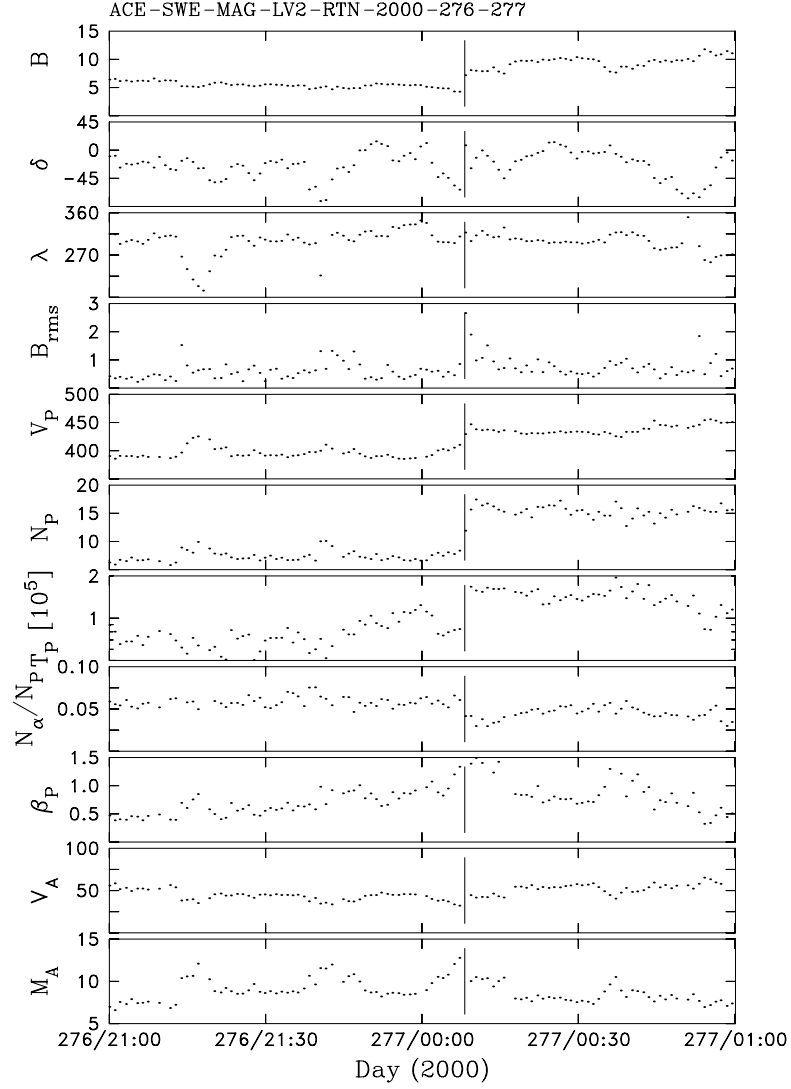


Figure 3.2: Same as Figure 3.1 plotted for day 277 of year 2000. Vertical lines mark the shock preceding the ICME on day 277 of Figure 3.1. Note sharp jumps in magnetic field strength, solar wind speed, proton density, and proton temperature indicating the presence of a shock.

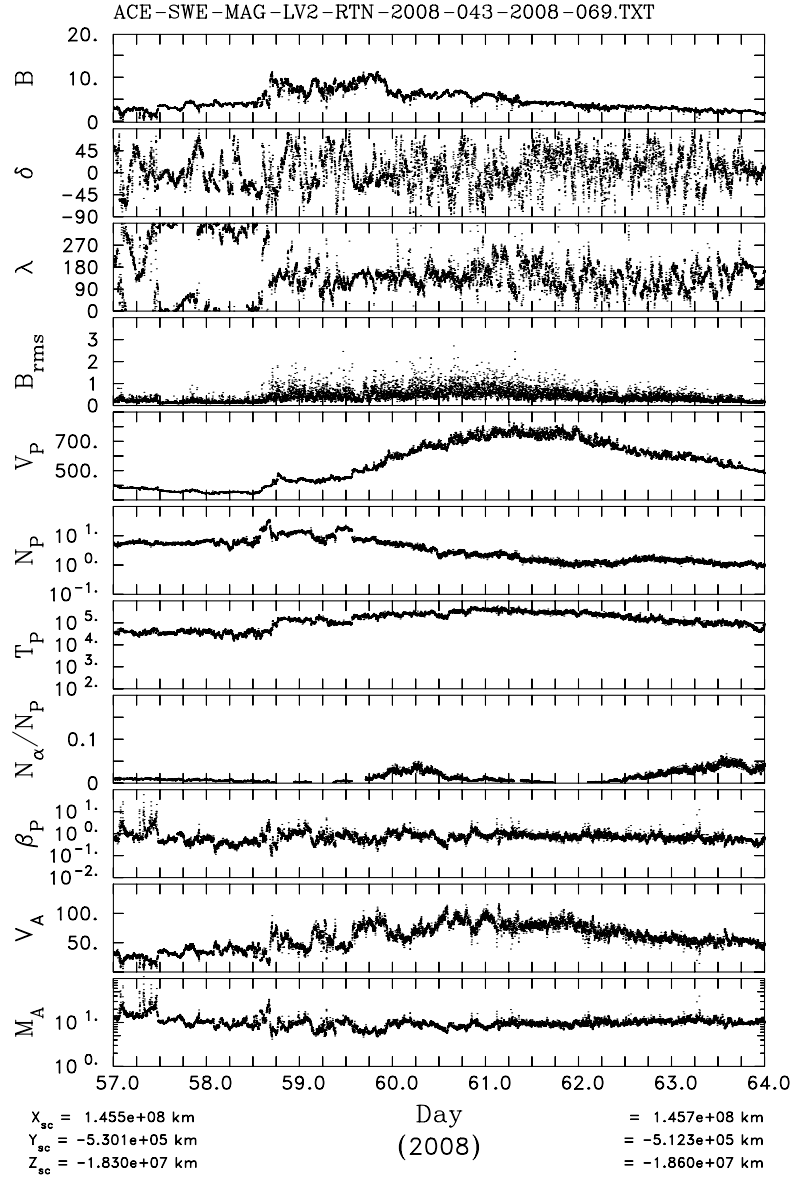


Figure 3.3: Same as Figure 3.1 but plotting the time period spanning days 57–63 of year 2008. Note the simple structure of the solar wind and associated thermal ion data. This is typical of solar wind conditions during solar minimum. Note CIR from days 58.5 until 61.25 with a pile-up of magnetic field at the leading edge. Note, too, that the IMF is highly variable about a well-defined mean throughout much of the period despite the quiet structure of the wind.

3.2 Shocks

Shocks are another feature often present in the solar wind. The solar wind travels at velocities greater than the sound speed and Alfvén speed within the medium and is susceptible to discontinuities in the flow speed. This process is similar to shock formation in air when an airplane breaks the sound barrier. The Alfvén speed refers to the propagation speed of one of the dominant wave modes in the solar wind and is further discussed in Section 3.6.

In the solar wind, shocks are characterized by abrupt changes in the magnetic field strength, velocity, density, and temperature. As discussed in the previous section, one method of shock formation occurs when fast moving ICMEs push through the ambient solar wind. The ACE spacecraft observes many of these shocks. Figure 3.2 shows the shock produced by the second ICME in Figure 3.1. A vertical line is placed to show the approximate position of the shock on the plot. Note the discontinuities present in the above mentioned parameters. This shock is noted by the ACE Science Center¹, who characterize it as a forward shock meaning it is propagating away from the Sun. The velocity of shock propagation in the spacecraft frame is computed to be 347 ± 47 km/s, the ratio of densities across the shock is 2.1 ± 0.1 , the ratio of the magnetic field strengths across the shock is 2.1 ± 0.2 , and the Alfvén mach number is 2.6 ± 0.6 . These values are typical of those seen at 1 AU. In the analyses presented here, we typically remove these shocks along with the driving CMEs because they introduce compressible effects not included in the theory we describe in Chapter 5.

Another class of objects that can lead to shock formation are Corotationg Interaction Regions (CIRs). As we briefly describe in Section 2.2, long lived sources on the Sun produce solar wind streams of a variety of speeds, both slow and fast. The rotation of the Sun can cause fast wind streams to come up behind slow wind streams and plow through the slower moving plasma. This process can lead to compression of the plasma between the slow and fast moving streams. If the velocity difference is great enough (i.e greater than the Alfvén speed), a shock can be produced. Shock formation due to CIRs typically occurs beyond 1 AU; however, the steepening of the velocity, magnetic field, etc., leading to the shock formation, can be seen at 1 AU (Kivelson and Russell, 1995). Figure 3.3 shows an example of a CIR recorded by ACE from days 58 to 61 of 2008. This plot also provides a good example of typical solar wind conditions at solar minimum.

The reverse situation, where a slow wind stream is behind a fast wind stream, is also seen in the solar wind. In this situation, the fast wind pulls away from the slow wind creating a region known as a rarefaction. Rarefactions are typically characterized by lower densities and cooler temperatures due to the expansion of the plasma.

Both the compressional CIRs and rarefaction intervals are further discussed in the analysis of Chapter 9. In particular, the effects that compression intervals can have on that analysis are discussed.

3.3 The Interplanetary Magnetic Field

Due to dynamic processes collectively known as the solar dynamo, the Sun produces a magnetic field. As discussed in the previous chapter, this magnetic field consists of both open magnetic field lines (which extend into the outer heliosphere) and closed magnetic field

¹http://www.ssg.sr.unh.edu/mag/ace/ACElists/obs_list.html

lines (which are doubly connected to the Sun); the overall structure of which, varies over the course of the solar cycle. However, throughout the solar cycle open solar magnetic flux permeates interplanetary space. This is what is known as the Interplanetary Magnetic Field.

The IMF is coupled to the solar wind plasma due to the high conductivity of the system. The mathematical description and consequences of this coupling are described in greater detail in Sections 3.4–3.6. In particular, the magnetic field is said to be “frozen-in” to the plasma, or in other words the magnetic field moves with the solar wind (see Section 3.5). As a result, a variety of transient phenomena, including the CMEs, CIRs, and shocks discussed previously, induce fluctuations in the magnetic field. Note the variability of the field in the top four panels of Figures 3.1 and 3.3. The closed magnetic loop structures of ICMEs and discontinuities of shocks are also readily evident in observations and, in their own right, represent a significant variability in the IMF.

The main focus of this thesis deals with the evolution of both the IMF fluctuations and the coupled plasma fluctuations in the form of turbulence. While the transient phenomena drive the fluctuations we study herein, they themselves represent a contamination to the data that is outside the theories we employ. As a result, we aim to remove these in our analyses.

3.4 The MHD Equations

As discussed, the solar wind is a mass of ionized gas known as plasma which flows radially from the Sun and is permeated by a large scale magnetic field. The dynamics of the solar wind can be viewed in several contexts. The most straight forward of these views, which lends insight into the behavior at the smallest scales in the plasma, is to view the solar wind as a collection of charged particles moving in the presence of a magnetic field. The dominant force governing the dynamics of this system is the Lorentz force, which acts on a moving charged particle in the direction perpendicular to both the particle’s motion and the direction of the magnetic field. If the particle’s motion has some angle to the magnetic field, this force results in a spiraling motion of the particle along the magnetic field line. The radius r_c of the spiral, known as the gyro-radius or cyclotron radius, is given by the relationship (Kivelson and Russell, 1995):

$$r_c = \frac{mv_{\perp}}{qB} \quad (3.1)$$

where m is the mass of a particle with charge q , v_{\perp} is the component of the particles velocity in the direction perpendicular to the magnetic field, and B is the magnitude of the magnetic field. The solar wind is predominantly made up of protons and electrons with typical gyro-radii of ~ 50 – 100 km and ~ 1 – 2 km respectively (Barnes, 1979). Further effects which follow from this view of plasma dynamics and relate to the dissipation of turbulent energy are discussed in Section 4.4.

A second description of plasma dynamics, which is valid for scales greater than the gyro-radii, where we are only concerned with the bulk motions of the plasma, can be developed if we consider the plasma to be a fluid. In hydrodynamics, an expression describing the motion of a fluid (i.e. water, air in the limit where velocities are much less than the sound speed, etc.) can be constructed by considering Newton’s second law and relating the momentum of the particles within the fluid to the forces acting on the fluid as a whole. Under the assumption of incompressibility (or in other words, a constant density within an arbitrary

volume moving with the fluid), the resulting momentum evolution is given by the Navier-Stokes (N-S) equation:

$$\frac{\partial \mathbf{v}(\mathbf{x}, t)}{\partial t} + (\mathbf{v} \cdot \nabla) \mathbf{v} = -\frac{1}{\rho} \nabla P + \nu \nabla^2 \mathbf{v} \quad (3.2)$$

where \mathbf{v} is the velocity field, ρ is the mass density, P is the fluid pressure, ν is the kinematic viscosity, and the incompressibility condition is given by $\nabla \cdot \mathbf{v} = 0$ (Frisch, 1995; Pope, 2000).

For a fluid consisting of charged ions and electrons, the presence of a magnetic field plays a significant role in governing the dynamics of the system. As such, Eq. (3.2) must be modified using Maxwell's equations, Ohm's law, and the Lorentz force. Analogous to the incompressible N-S equation, the incompressible magnetohydrodynamic equations, governing the large-scale motion of a plasma in a magnetic field, are given by (Kivelson and Russell, 1995; Smith, 2009):

$$\frac{\partial \mathbf{v}(\mathbf{x}, t)}{\partial t} + (\mathbf{v} \cdot \nabla) \mathbf{v} = -\frac{1}{\rho} \nabla P + \frac{1}{\mu_0 \rho} (\nabla \times \mathbf{B}) \times \mathbf{B} + \nu \nabla^2 \mathbf{v} \quad (3.3)$$

$$\frac{\partial \mathbf{B}(\mathbf{x}, t)}{\partial t} = \nabla \times (\mathbf{v} \times \mathbf{B}) + \eta \nabla^2 \mathbf{B} \quad (3.4)$$

$$\nabla \times \mathbf{B} = \mu_0 \mathbf{j} \quad (3.5)$$

$$\nabla \cdot \mathbf{B} = 0 \quad (3.6)$$

$$\nabla \cdot \mathbf{v} = 0 \quad (3.7)$$

where \mathbf{B} is the magnetic field, \mathbf{j} is the current density, and η is the magnetic diffusivity. The magnetic diffusivity is given by $\eta = 1/(\mu_0 \sigma)$ where μ_0 is the permeability of free space and σ is the electrical conductivity. Notice that the complete N-S equation is imbedded in Eq. (3.3). This is the modified momentum equation with the additional term $(\mu_0 \rho)^{-1} (\nabla \times \mathbf{B}) \times \mathbf{B}$, which describes the effect of the Lorentz force on the system. A slightly deeper understanding of how the magnetic field acts on the plasma is obtained if we rewrite this term as $(\mu_0 \rho)^{-1} (\nabla \times \mathbf{B}) \times \mathbf{B} = (\mu_0 \rho)^{-1} (\mathbf{B} \cdot \nabla) \mathbf{B} - \rho^{-1} \nabla B^2 / (2\mu_0)$, where the first term corresponds to a “magnetic tension” force acting on the plasma and the second term can be related to a “magnetic pressure” imposed on the system.

Just as the large-scale magnetic field influences the motion of the plasma, the moving charged particles also influence the magnetic field. As such, Eq. (3.4), (3.5) and (3.6) are all derived from Maxwell's equations and are used to describe the evolution of the \mathbf{B} field. Eq. (3.6) is the familiar expression stating that there are no magnetic monopoles and Eq. (3.5) is simply Ampère's law, where the displacement current has been taken to be negligible under the MHD assumptions. Eq. (3.4), known as the induction equation, explicitly describes the time evolution of the magnetic field and is a re-expression of Faraday's law, where the electric field \mathbf{E} has been computed using Ohm's law and Eq. (3.5) (Kivelson and Russell, 1995; Rempel, 2009). Finally, Eq. (3.7) is again the incompressibility condition. Compressible MHD equations are equally derivable as are multi-fluid MHD equations, treating ions and electrons as separate fluids, but the above are the simplest form and the logical starting point for the work developed here.

Further symmetry between hydrodynamics and MHD can be seen if we express Eq. (3.3) and (3.4) in terms of the Elsässer variables $\mathbf{Z}^\pm = \mathbf{v} \pm \mathbf{B}/\sqrt{\mu_0 \rho}$ (Elsässer, 1950):

$$\frac{\partial \mathbf{Z}^\pm}{\partial t} + (\mathbf{Z}^\mp \cdot \nabla) \mathbf{Z}^\pm = -\frac{1}{\rho} \nabla P_{\text{MHD}} + \left(\frac{\nu + \eta}{2} \right) \nabla^2 \mathbf{Z}^\pm \quad (3.8)$$

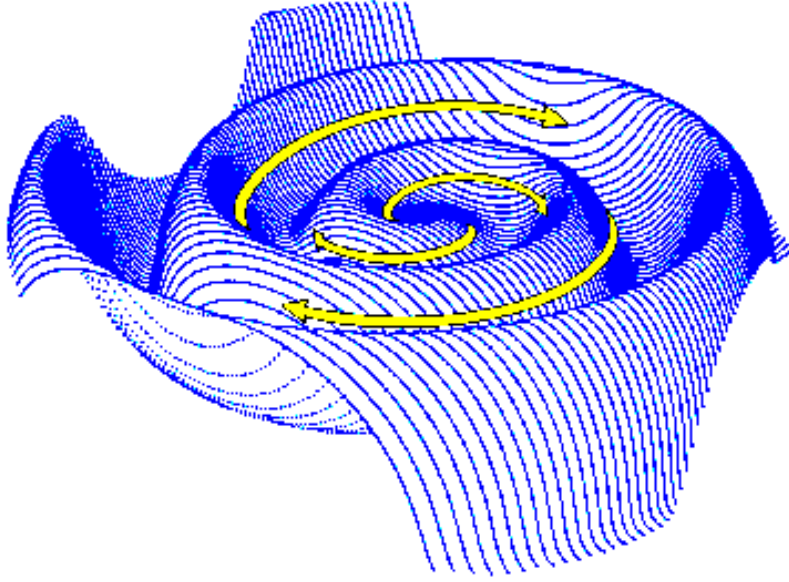


Figure 3.4: Image illustrating the Parker spiral structure of the IMF in 3 dimensions. Arrows show the path of outward directed magnetic field lines along the contour. In this thesis, we consider the 2 dimensional cut of this structure in the ecliptic plane. Figure reproduced from Ness and Wilcox (1965).

where P_{MHD} is the sum of the fluid pressure and the magnetic pressure, such that $P_{\text{MHD}} = P + \frac{B^2}{2\mu_0}$. Eq. (3.8) assumes $\eta = \nu$. Otherwise, the more general form is less compact. We also note that Eq. (3.6) and (3.7) lead to the incompressibility of the Elsässer variables (i.e $\nabla \cdot \mathbf{Z}^\pm = 0$). In this formulation, both the evolution of the velocity and magnetic field can be described using two equations, which are of the same form as the N-S equation. The Elsässer variables can be thought of as corresponding to “Alfvén” waves, which represent one of the dominant modes of fluctuation in MHD and will be further discussed in Section 3.6. However, this is not the only interpretation of the Elsässer variables and this formulation of the MHD equations is general regardless of the presence of Alfvén waves.

3.5 The Parker Spiral

The time varying structures of the IMF mentioned in Section 3.3 are superimposed upon a large-scale relatively time invariant structure to the field. The form of the large-scale IMF structure is derived in Parker (1958). Due to the rotation of the Sun, the field takes on the form of an Archimedean spiral (often referred to as the Parker spiral in this context) in the ecliptic plane. Because the Sun rotates differentially, with the solar equator rotating faster than the poles, the three-dimensional structure of the IMF takes on a more complex form often referred to as a “ballerina skirt.” Figure 3.4 illustrates this structure. In this section, we will focus on the two-dimensional structure in the ecliptic plane, as it is most directly relevant to the studies described in this thesis.

To understand this structure, we employ a useful simplification to the MHD equations known as Ideal MHD. In this approximation, it is assumed that the electrical conductivity σ of the plasma is infinite. In the solar wind, while the conductivity is certainly not infinite,

it is very high and the Ideal MHD approximation can lend some insight into an interesting feature of MHD plasma flows.

Recall that the magnetic diffusivity seen in the induction equation (see Eq. (3.4)) is related to σ^{-1} . As such, under Ideal MHD the induction equation becomes (Kivelson and Russell, 1995; Rempel, 2009):

$$\frac{\partial \mathbf{B}}{\partial t} = \nabla \times (\mathbf{v} \times \mathbf{B}) \quad (3.9)$$

From this equation, it can be shown that the magnetic flux through an arbitrary surface moving with the plasma is unchanging in time. It is, therefore, said that the magnetic field moves with the plasma in an Ideal MHD fluid or in other words, the field is “frozen-in” to the plasma.

Let us now consider a time invariant magnetic field and solar wind plasma flow emanating radially from the Sun. We take the plasma flow to have a constant radial velocity V_{SW} with respect to the heliocentric distance. In the reference frame rotating with the Sun, the plasma flow in the ecliptic plane has an apparent velocity in polar coordinates of $v_R = V_{SW}$ in the R-direction and $v_\phi = -\Omega R$ in the ϕ -direction, where Ω is the angular rotation rate of the Sun at its equator and R is the radial distance from the Sun. From the frozen-in-field condition described above, the two magnetic field components must be related in a similar fashion. We can, therefore, write (Kivelson and Russell, 1995):

$$\frac{B_R}{B_\phi} = \frac{v_R}{v_\phi} = -\frac{V_{SW}}{\Omega R} \quad (3.10)$$

The overall shape of any given magnetic field line can be determined by rewriting Eq. (3.10) in the following manner:

$$\frac{dR}{d\phi} = -\frac{V_{SW}}{\Omega} \quad (3.11)$$

where v_R has been rewritten as $\frac{dR}{dt}$ and v_ϕ has been rewritten as $R\frac{d\phi}{dt}$. Since V_{SW} and Ω are constants, the obvious solution to this differential equation, with boundary conditions applied, is the equation of an Archimedean spiral:

$$R - R_\odot = -\frac{V_{SW}}{\Omega} (\phi - \phi_0) \quad (3.12)$$

where R_\odot is the solar radius and ϕ_0 is the angular position of a particular magnetic field line at the surface of the Sun.

We can also determine the two components of the equatorial magnetic field. The fact that the magnetic flux from the Sun is constant, leads to the following equation for the radial magnetic field:

$$B_R = B \left(\frac{R_\odot}{R} \right)^2 \quad (3.13)$$

By combining this equation for the radial field strength with the frozen-in-field equation given by Eq. (3.10), we find that the longitudinal component to the field is given by:

$$B_\phi = -B \frac{\Omega R_\odot^2}{V_{SW} R} \quad (3.14)$$

Note, the radial magnetic field strength varies as R^{-2} , while the longitudinal component varies as R^{-1} .

From Eq. (3.13) and (3.14), the angle between the magnetic field direction and the radial direction, denoted by Θ_{BR} , in the ecliptic plane is given by:

$$\tan \Theta_{BR} = \frac{B_\phi}{B_R} = -\frac{\Omega R}{V_{SW}} \quad (3.15)$$

The Sun has a sidereal rotation period at the equator of ~ 25 days, with a synodic rotation period as viewed from the Earth (or the ACE spacecraft) of ~ 27 days. If we take the typical solar wind speed to be ~ 400 km/s and use the synodic rotation period of the Sun, this leads to a nominal angle between magnetic field and the radial direction of $\sim 45^\circ$ as viewed by the ACE spacecraft or an observer on Earth at 1 AU. However, it is important to remember that as discussed in Section 3.3, there is significant variation in the IMF and a whole range of angles can be measured depending on the interval of solar wind data.

3.6 Waves in Interplanetary Space

The MHD equations are capable of supporting a number of different wave modes, including slow mode waves, fast mode waves, and Alfvén waves (Barnes, 1979). Slow mode waves are highly compressive and generally damped in the solar wind. Observations of slow mode waves in the solar wind are, at the least, rare. Fast mode waves are comparable in many ways to Alfvén waves, but are compressive and weakly damped with opposing polarization. Of particular interest in the study of MHD turbulence in the solar wind, is the Alfvén mode, which features magnetic and velocity fluctuations that are transverse to the mean magnetic field. Alfvén waves exhibit no density fluctuations in first-order theory. They are non-dispersive (propagate at a fixed speed) and bear a strong resemblance to a broad class of solar wind observations.

We can begin to glean some insight into this particular wave mode by further analysis of the MHD equations. In general, wave behavior is caused by the leading order, linear, and non-dissipative dynamics of a system. As such, we consider the linearized versions of Eq. (3.3) and (3.4) by assuming:

$$\mathbf{B}(\mathbf{x}, t) = \mathbf{B}_0 + \varepsilon \mathbf{b}_1(\mathbf{x}, t) \quad (3.16)$$

$$\mathbf{v}(\mathbf{x}, t) = \varepsilon \mathbf{v}_1(\mathbf{x}, t) \quad (3.17)$$

where \mathbf{B}_0 is the spatially and temporally constant average magnetic field, \mathbf{b}_1 is the first order perturbation to the magnetic field such that the average of \mathbf{b}_1 is zero, and \mathbf{v}_1 is the first order perturbation on the velocity field such that the average of \mathbf{v}_1 is zero. ε is simply a parameter characterizing the “order” (i.e. first order, second order, etc.) of the terms. The fact there is no constant velocity term \mathbf{V}_0 in Eq. (3.17) indicates we are considering the frame of reference moving with the plasma. This can be done without loss of generality. Note, higher order perturbations to the \mathbf{B} and \mathbf{v} fields have been dropped.

By substituting Eq. (3.16) and (3.17) into Eq. (3.3) and (3.4), dropping any terms that are second order or higher, and neglecting the two dissipative terms $\nu \nabla^2 \mathbf{v}$ and $\eta \nabla^2 \mathbf{B}$, we are left with the linearized MHD equations:

$$\frac{\partial \mathbf{v}_1}{\partial t} = \frac{1}{\mu_0 \rho} (\nabla \times \mathbf{b}_1) \times \mathbf{B}_0 \quad (3.18)$$

$$\frac{\partial \mathbf{b}_1}{\partial t} = \nabla \times (\mathbf{v}_1 \times \mathbf{B}_0) \quad (3.19)$$

While not demonstrated here due to the complexity of the problem, it can be shown that Eq. (3.18) and (3.19) can be combined to produce a wave equation. We, therefore, assume wave solutions to the set of coupled linear equations:

$$\mathbf{v}_1 = \mathbf{v}'_1 e^{i(\mathbf{k} \cdot \mathbf{x} - \omega t)} \quad (3.20)$$

$$\mathbf{b}_1 = \mathbf{b}'_1 e^{i(\mathbf{k} \cdot \mathbf{x} - \omega t)} \quad (3.21)$$

where \mathbf{k} is the wave vector, related to the wave length and direction of propagation, and ω is the angular frequency of the wave. From Eq. (3.6) and (3.7), we see that $\mathbf{k} \cdot \mathbf{v}'_1 = 0$ and $\mathbf{k} \cdot \mathbf{b}'_1 = 0$.

We impose the conditions $\mathbf{v}'_1 \cdot \mathbf{B}_0 = 0$ and $\mathbf{b}'_1 \cdot \mathbf{B}_0 = 0$ to limit the analysis to transverse fluctuations. By inserting the wave solutions given by Eq. (3.20) and (3.21) into Eq. (3.18) and (3.19), we can solve for the Alfvén wave dispersion relation:

$$\omega = \frac{|\mathbf{k} \cdot \mathbf{B}_0|}{\sqrt{\mu_0 \rho}} \quad (3.22)$$

The group velocity of a wave is given by $\frac{\partial \omega}{\partial k}$, so we can write the Alfvén speed as:

$$V_A = \frac{B_0}{\sqrt{\mu_0 \rho}} \quad (3.23)$$

We can further determine the relationship between \mathbf{v}_1 and \mathbf{b}_1 in an Alfvén wave, by utilizing Eq. (3.16), (3.17), and (3.22):

$$\mathbf{v}_1 = -\frac{1}{\sqrt{\mu_0 \rho}} \frac{(\mathbf{k} \cdot \mathbf{B}_0)}{|\mathbf{k} \cdot \mathbf{B}_0|} \mathbf{b}_1 = \pm \frac{\mathbf{b}_1}{\sqrt{\mu_0 \rho}} \quad (3.24)$$

From this expression, we see that not only are Alfvénic fluctuations transverse to \mathbf{B}_0 , but \mathbf{v}_1 and \mathbf{b}_1 also fluctuate along the same axis. Note $\mathbf{v}_1 = +\mathbf{b}_1/\sqrt{\mu_0 \rho}$ corresponds to waves propagating anti-parallel to \mathbf{B}_0 and $\mathbf{v}_1 = -\mathbf{b}_1/\sqrt{\mu_0 \rho}$ corresponds to parallel wave propagation. This relationship between velocity and magnetic field fluctuations provides the motivation for the Elsässer variable formulation of the MHD equations seen in Eq. (3.8). (Note that the Alfvén speed is often expressed in CGS units as $V_A = B_0/\sqrt{4\pi\rho}$. Likewise, the Elsässer variables can be expressed in CGS units as $\mathbf{Z}^\pm = \mathbf{v} \pm \mathbf{B}/\sqrt{4\pi\rho}$.)

Observationally, the presence of wave like behavior in the interplanetary solar wind plasma has been known since the 1960's. From the earliest in situ measurements of interplanetary space, it was noted that small-scale irregular behavior is present in the solar wind. One explanation for this irregularity is the presence of the various MHD wave modes. Two major studies (Coleman, 1966; Belcher and Davis, 1971), attempt to analyze the observed fluctuations and determine the general properties of the wave modes present in the solar wind. In the study of Coleman (1966), it is determined that interplanetary solar wind fluctuations can be attributed to a superposition of randomly polarized and predominantly outward propagating Alfvén or fast mode waves. The presence of slow mode waves is not determined in this study. In a more in depth study, Belcher and Davis (1971) concluded that the small-scale fluctuations of the solar wind are largely made up of outward propagating Alfvén waves and that the “purest” instances of these waves are seen in fast solar wind streams.

Figure 3.5 shows an example of the Belcher and Davis (1971) results. Solar wind magnetic field and plasma velocity observations are plotted over a 24 hr period. The mean magnetic

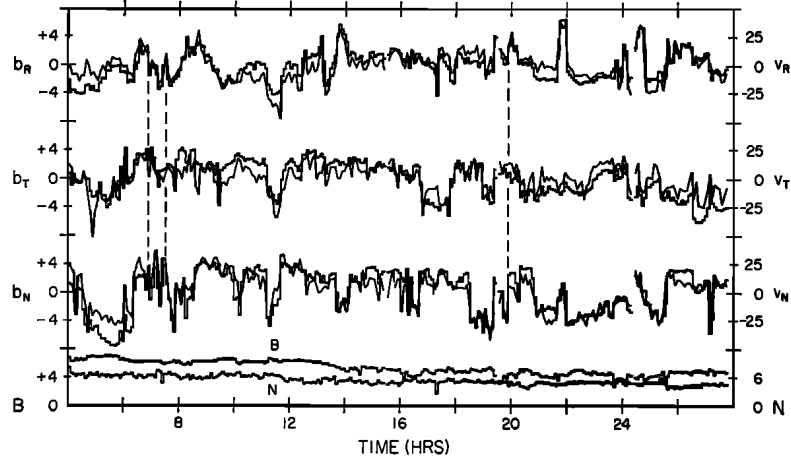


Figure 3.5: 24 hrs of magnetic field and plasma data from Mariner 5. The top six curves show the three components of the magnetic field and plasma velocity, while the bottom two curves show the magnetic field strength and proton number density. Note the strong positive correlation between velocity and magnetic field fluctuations, which demonstrate the presence of outward propagating Alfvén waves. Figure reproduced from Belcher and Davis (1971).

field over this interval is directed inward (towards the Sun) along the Parker spiral. Notice the high degree of positive correlation between the velocity and magnetic field (meaning fluctuations in \mathbf{v} follow fluctuations in \mathbf{b} or vice versa) for all three components of the two fields. This is consistent with the above definition of Alfvén waves. The scaling ratio used for plotting the velocity and magnetic field measurements is in accordance with Eq. (3.24) with an additional correction term accounting for anisotropies seen in the solar wind. Remember that positive correlation between \mathbf{v} and \mathbf{b} corresponds to Alfvén waves propagating anti-parallel to the magnetic field. Since the mean magnetic field in this interval is directed inward, the fluctuations seen in Figure 3.5 are propagating outward (away from the Sun) along the Parker spiral.

The wave description of interplanetary fluctuations is not the whole story. Coleman (1968) finds that the power spectra (see Section 4.1) of interplanetary fluctuations follows a reproducible power law scaling over a range of frequencies from $\sim 1.16 \times 10^{-4}$ Hz to $\sim 1.35 \times 10^{-2}$ Hz. This indicates that some “universal” process must be shaping the spectrum. Coleman (1968) proposes turbulence, which offers several predictions for universal power spectra scaling laws (see Section 4.3), can account for the observed interplanetary spectral form. In particular, Coleman (1968) suggests a turbulent process similar to that proposed by Kraichnan (1965), in which oppositely propagating Alfvén waves interact non-linearly, can account for the observed spectra.

It is important to note the key difference between the wave phenomenon and turbulence. Waves represent stable propagating structures in the MHD fluid, while turbulence represents an inherently chaotic and unstable process in which fluctuations are created and destroyed through the non-linear terms in the MHD equations.

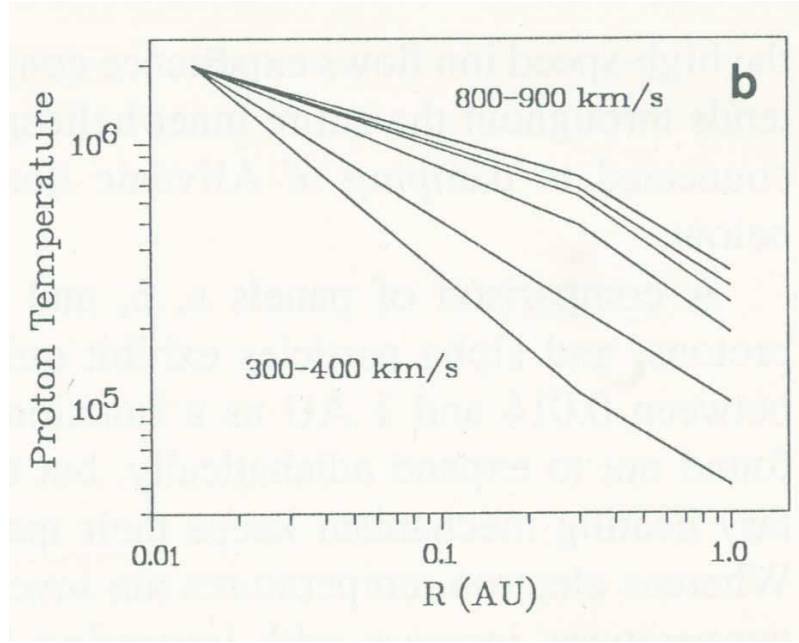


Figure 3.6: Fits of the average proton temperature measured by the Helios spacecraft as a function of distance from the Sun. Separate curves correspond to 100 km/s intervals in solar wind speed between 300 and 900 km/s. The region of the plot outside of 0.3 AU comes from actual Helios measurements, while the region inside of 0.3 AU is simply an extrapolation to a typical solar corona temperature of 2×10^6 K. The region inside of 0.3 AU is not pertinent to our discussion. When corrected for the continued acceleration of slow speed winds between 0.3 and 1 AU, all wind speed intervals experience a shallower cooling ($\sim R^{-0.9}$) than the $R^{-4/3}$ prediction of adiabatic expansion. Figure reproduced from Marsch (1991).

3.7 Solar Wind Heating

The simplest prediction for the temperature dependence of the solar wind as a function of heliocentric distance R is that it experiences an adiabatic cooling of the form $R^{-4/3}$ as the plasma expands into the heliosphere. Numerous spacecraft provide measurements of this radial temperature dependence, including the Voyager spacecraft in the outer heliosphere (Richardson et al., 1995; Richardson and Smith, 2003) and the Helios spacecraft in the inner heliosphere (Totten et al., 1995; Vasquez et al., 2007). These measurements show the solar wind cools at a rate slower than is expected by adiabatic expansion. This fact suggests additional heating (or in other words energy input) must be supplied to the plasma as it expands from the Sun.

Helios measurements, especially with an important correction for wind acceleration, show the radial component of the proton temperature T_P for all streams of various speeds follows an $R^{-0.9 \pm 0.1}$ form near 1 AU (Totten et al., 1995). This is considerably shallower than the adiabatic prediction of $R^{-4/3}$. Figure 3.6 shows fits of the average proton temperature as a function of distance from the Sun. The pertinent interval is between 0.3 and 1 AU, where data was actually measured by the Helios spacecraft. The values closer to the Sun than 0.3 AU are simply extrapolations to a common solar corona temperature. The gradients of these curves are related to the average local heating rate of solar wind protons. Verma et al.

(1995) and Vasquez et al. (2007) find the proton heating rate can be evaluated assuming an isotropic thermal distribution. One complication in the analysis is that slow winds continue to accelerate between 0.3 and 1 AU and this needs to be taken into account when comparing points on the figure. In particular, Vasquez et al. (2007) give an expression for the proton heating rate per unit mass at 1 AU once the correction for slow wind conditions is made:

$$\epsilon_{\text{heat}} = 3.6 \times 10^{-5} T_P V_{SW} \text{ [J/(kg s)]} \quad (3.25)$$

where V_{SW} is the solar wind speed in km/s and T_P is in units of Kelvin. This expression is based on an $R^{-0.9}$ radial dependence of T_P .

One possible source for this energy input is turbulence, which, at small scales, dissipates energy into heat. One of the main objectives of the analyses presented in Chapter 7 is determining if there is sufficient turbulent energy to account for this heating. In Chapters 7–9, we make use of Eq. (3.25) to compare energy cascade rates at 1 AU to proton heating rates.

Chapter 4

Solar Wind Turbulence

In this chapter, we explore the general concepts of turbulence theory including the existence of multiple “ranges” where different dynamics dominate the flow. We explore the observations that help support the assertion that the interplanetary medium is fundamentally turbulent in the sense of hydrodynamics with magneto-dynamic additions that we describe using magnetohydrodynamics.

4.1 Interplanetary Power Spectra

The Sun, and particularly the solar atmosphere, is a dynamic environment which evolves over a broad range of length and time-scales. As discussed above, there is a 22 yr solar cycle associated with the solar dipole magnetic field. In terms of solar activity, this can be divided into two 11 yr cycles, each possessing a solar activity minimum and maximum. At spatial scales on the order of the Sun’s radius ($\sim 7 \times 10^5$ km), solar oscillations (such as P-mode, G-mode, etc.) propagate through the solar interior (Zirker, 2003). These large-scale solar oscillation modes propagate into the depths of the Sun and are used in helioseismology studies, which probe the solar interior. At smaller scales, convective motions in the outer layers of the Sun cover the solar surface with supergranules on the order of $\sim 3 \times 10^4$ km in diameter and granules on the order of ~ 500 km in diameter with spicules showing movement and vibration along their borders (Kivelson and Russell, 1995). Reconnection causes abrupt topology changes for the magnetic field, flares, and the release of Coronal Mass Ejections. Everywhere and at all scales observed so far, there is dynamics on the Sun.

As discussed in Chapter 3, magnetic field lines lead out from the solar corona and are tied to the solar wind plasma, giving rise to the large scale structure of the interplanetary medium. However, both the solar wind and the imbedded magnetic field are far from steady. Magnetic field lines are rooted to the photosphere where dynamics on the Sun lead to “foot point motion” generating waves that propagate along the magnetic field lines, similar to waves on a string, and out into the interplanetary medium. The solar wind itself is also variable with “fast” and “slow” winds arising from various sources on the Sun. Large-scale ejecta (ICMEs) move through the solar wind, providing an added source of energy as the ambient plasma is forced to flow into or around the transient. Shocks inject energy into the flow in a similar manner. Within the solar wind, fluctuations in the ambient flow and magnetic field exist at all temporal and spatial scales.

Turbulence offers a method by which the energy input by these solar sources can move across scales and provide a mechanism for heating the solar wind. In order to study this

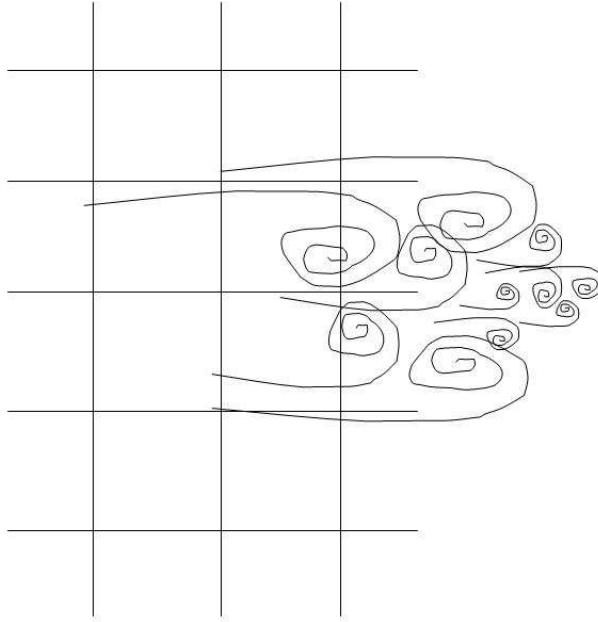


Figure 4.1: A sketch of turbulence forming behind a wire grid placed in a wind tunnel. Large-scale, energy-containing eddies form directly upstream of the grid. The scale of these eddies is on the order of the grid spacing. Through non-linear interactions the large-scale eddies break down into smaller eddies, “cascading” energy to smaller scales.

process, one needs a way of resolving the dynamics of solar wind fluctuations and understanding the extent to which an observation is the direct result of the solar input vs. in situ processes that remake the energy into different forms. Spectral analysis, in which the power (and thus the energy content) in each of the various spatial/temporal scales is determined, is one common way of characterizing the distribution of energy in solar wind measurements. Alone, the power spectrum says nothing about the underlying dynamics of the fluctuations. However, turbulence theory attempts to better understand the processes that move energy from one scale to another and evolve the spectrum into the observed form. Fortunately, several well-supported theories of “universal” dynamical processes lead to predictions for spectral forms that are observed in the solar wind.

4.2 Energy-Containing Range

We can divide the interplanetary spectrum into 3 ranges based on the terminology of traditional hydrodynamics: The energy-containing range, the inertial range, and the dissipation range. The energy-containing range contains large-scale dynamical objects that directly reflect their generation mechanism without additional in situ processing. To take an example from hydrodynamics, consider a wire grid placed in a wind tunnel. A sketch of this system is provided in Figure 4.1. Directly down stream of the grid, shear forces between the grid and the flow produce vortices (eddies) that are indicative of the scale size of the wire mesh. These are the turbulent structures of the energy containing range and they possess a strong correlation (memory) of the manner in which they were generated. As time progresses, non-

linear interactions between the eddies cause a breakdown of the large-scale energy containing structures and produce smaller eddies, which in turn interact to produce smaller eddies, until eddy size is sufficiently small that viscosity leads to dissipation. This is the concept called “cascade” in turbulence theory (Frisch, 1995).

The mechanisms behind the cascade process can be seen if we consider the N-S equation, which governs the dynamics of a hydrodynamic fluid flow. Although shown in the previous chapter, we again remind the reader of this important equation:

$$\frac{\partial \mathbf{v}(\mathbf{x}, t)}{\partial t} + (\mathbf{v} \cdot \nabla) \mathbf{v} = -\frac{1}{\rho} \nabla P + \nu \nabla^2 \mathbf{v} \quad (4.1)$$

where \mathbf{v} is the velocity field in the fluid, ρ is the mass density, P is the pressure, and ν is the kinematic viscosity. Recall, the incompressibility of the flow is given by $\nabla \cdot \mathbf{v} = 0$.

The dominant fluctuation mode in incompressible hydrodynamic flows is the vorticity or eddy-like structure. We, therefore, rewrite the N-S equation in terms of the vorticity defined as $\omega = \nabla \times \mathbf{v}$ by taking the curl of Eq. (4.1):

$$\frac{\partial \omega(\mathbf{x}, t)}{\partial t} = \nabla \times (\mathbf{v} \times \omega) + \nu \nabla^2 \omega. \quad (4.2)$$

For simplicity, we limit our discussion to a two-dimensional flow so that ω is exclusively in the third direction. By invoking the incompressibility of the flow and taking note that ω is always orthogonal to the 2D flow, we can rewrite the first term on the r.h.s. of Eq. (4.2) as $\nabla \times (\mathbf{v} \times \omega) = \mathbf{v} \cdot \nabla \omega$. This gives the term responsible for the advection of eddies and is the leading non-linear interaction term in the N-S equation. Two key conclusions can be drawn from this term: 1) if a “small” eddy interacts with a larger eddy (i.e. the fields are arranged in such a way that small spatial gradients are applied), then the “small” eddy will simply be circulated around the field of the first. However, 2) if the two interacting eddies are of comparable scale, then strong gradients will be placed across the interacting eddies resulting in the distortion and eventual “shredding” into smaller eddies (Kolmogorov, 1941a). Frisch (1995) and Smith (2009) provide reviews of this argument. It is this process which leads to the cascade of energy mentioned above and allows interacting vortices to destroy each other, driving turbulence at other scales.

It is assumed that MHD fluctuations undergo a similar process. However, it is an important observation that the incompressible MHD equations in three dimensions (see Section 3.4) can support additional types of fluctuations aside from eddies, such as the Alfvén waves discussed in Section 3.6. We, therefore, postulate that the large-scale transient objects discussed in the previous section, which move through the solar wind so as to create a clear and undeniable interaction with the background plasma, are capable of providing an energy source to drive turbulence and thus make up the energy containing range of MHD turbulence.

We can begin to express this non-linear driving of turbulence by looking at the evolution of the total energy density in the N-S equation. We compute the dot product of $\mathbf{v}(\mathbf{x}, t)$ with Eq. (4.1) and obtain

$$\mathbf{v}(\mathbf{x}, t) \cdot \frac{\partial \mathbf{v}(\mathbf{x}, t)}{\partial t} = \frac{1}{2} \frac{\partial v^2(\mathbf{x}, t)}{\partial t} = \frac{\partial E_v(\mathbf{x}, t)}{\partial t} = -\mathbf{v} \cdot [(\mathbf{v} \cdot \nabla) \mathbf{v}] - \mathbf{v} \cdot \left(\frac{1}{\rho} \nabla P \right) + \nu \mathbf{v} \cdot \nabla^2 \mathbf{v} \quad (4.3)$$

This reveals the basic third-order term $(-\mathbf{v} \cdot [(\mathbf{v} \cdot \nabla) \mathbf{v}])$ that drives the turbulent energy.

The turbulent dynamics are further illuminated if we recast the N-S equation in Fourier variables. The velocity and pressure can be rewritten as Fourier series in wave number such that $\mathbf{v}(\mathbf{x}) = \sum_{\mathbf{k}} \mathbf{v}_{\mathbf{k}} e^{i\mathbf{k}\cdot\mathbf{x}}$ and $P = \sum_{\mathbf{k}} P_{\mathbf{k}} e^{i\mathbf{k}\cdot\mathbf{x}}$. Note that we only expand these in terms of wave vector and not frequency. By substituting these into Eq. (4.1) and using the fact that the terms in a Fourier series form an orthogonal set, the N-S equation becomes:

$$\frac{\partial \mathbf{v}_{\mathbf{k}}}{\partial t} = - \sum_{\mathbf{k}=\mathbf{k}_1+\mathbf{k}_2} [(\mathbf{v}_{\mathbf{k}_1} \cdot i\mathbf{k}_2) \mathbf{v}_{\mathbf{k}_2}] - \frac{1}{\rho} i\mathbf{k} P_{\mathbf{k}} - \nu k^2 \mathbf{v}_{\mathbf{k}} \quad (4.4)$$

where $\mathbf{v}_{\mathbf{k}}$ and $P_{\mathbf{k}}$ are the velocity and pressure at a particular scale with wave vector \mathbf{k} and $\sum_{\mathbf{k}=\mathbf{k}_1+\mathbf{k}_2} [\dots]$ denotes the sum over all combinations of wave vectors \mathbf{k}_1 and \mathbf{k}_2 that add up to the wave vector \mathbf{k} . The incompressibility condition, when expressed in Fourier space, becomes $\mathbf{v}_{\mathbf{k}} \cdot \mathbf{k} = 0$. As with Eq. (4.3), we can examine the evolution of energy in Fourier space by taking the dot product of Eq. (4.4) with $\mathbf{v}_{\mathbf{k}}$. This gives the following relation:

$$\frac{\partial E_{\mathbf{k}}}{\partial t} = -\mathbf{v}_{\mathbf{k}} \cdot \sum_{\mathbf{k}=\mathbf{k}_1+\mathbf{k}_2} [(\mathbf{v}_{\mathbf{k}_1} \cdot i\mathbf{k}_2) \mathbf{v}_{\mathbf{k}_2}] - \mathbf{v}_{\mathbf{k}} \cdot \left(\frac{1}{\rho} i\mathbf{k} P_{\mathbf{k}} \right) - 2\nu k^2 E_{\mathbf{k}} \quad (4.5)$$

where $E_{\mathbf{k}}$ now denotes the energy at a particular scale with wave vector \mathbf{k} . The first term on the r.h.s. of this equation is the non-linear term that produces turbulent interactions in a fluid, the second term on the r.h.s. becomes zero due to the incompressibility of the flow, and the last term on the r.h.s. deals with the viscous dissipation of energy. It can be readily seen that as \mathbf{k} gets large (or in other words the length scale of eddies gets small), the dissipation term becomes arbitrarily large and dominates the dynamics of the system. Under these conditions, any energy put into eddies at large \mathbf{k} scales will be rapidly dissipated. However, if over a range of \mathbf{k} the dissipative term is small enough such that the non-linear term dominates Eq. (4.5), the flow is said to be turbulent (see Smith, 2009, for tutorial).

We take the above formalism to one higher degree of complexity and describe the two-point auto-correlation function:

$$R(\mathbf{x} + \mathbf{L}) \equiv \mathbf{v}(\mathbf{x}, t) \cdot \mathbf{v}(\mathbf{x} + \mathbf{L}, t). \quad (4.6)$$

where \mathbf{L} is the vector separating two arbitrary points in space. If the system is judged to be “homogeneous” so that statistical properties including derivatives of statistical properties are independent of location, R is not a function of \mathbf{x} . R is termed the two-point auto-correlation function for the velocity and it is most often written as a matrix function of components v_i and v_j

$$R_{ij} \equiv \langle v_i(\mathbf{x} + \mathbf{L}) v_j(\mathbf{x}) \rangle \quad (4.7)$$

where $\langle \dots \rangle$ denotes an ensemble average. In fact, the auto-correlation function is always discussed as a statistical quantity.

From the auto-correlation function, one sees the fundamental problem with turbulence theory: closure. The evolution of the second-order term involves a third-order term at two points which is unknown, the evolution of the third-order term involves a fourth-order form, etc. Specifically, if we assume homogeneity, we can write:

$$\begin{aligned} \frac{\partial}{\partial t} R_{ij}(\mathbf{L}) &= \frac{\partial}{\partial t} \langle v_i(\mathbf{x}) v_j(\mathbf{x} + \mathbf{L}) \rangle \\ &= \left\langle v_j(\mathbf{x} + \mathbf{L}) \frac{\partial}{\partial t} v_i(\mathbf{x}) + v_i(\mathbf{x}) \frac{\partial}{\partial t} v_j(\mathbf{x} + \mathbf{L}) \right\rangle \\ &\sim -\frac{\partial}{\partial x_k} \langle v_j(\mathbf{x} + \mathbf{L}) v_k(\mathbf{x}) v_i(\mathbf{x}) \rangle - \frac{\partial}{\partial \mathbf{L}_k} \langle v_i(\mathbf{x}) v_k(\mathbf{x} + \mathbf{L}) v_j(\mathbf{x} + \mathbf{L}) \rangle \end{aligned} \quad (4.8)$$

where summations are carried out over repeated indices in the last line. The last line of Eq. (4.8) is obtained by approximating the time derivatives in the second line with the non-linear term $(\mathbf{v} \cdot \nabla) \mathbf{v}$ from the N-S equation and invoking homogeneity. Using the full N-S equation to rewrite the time derivatives produces additional terms in Eq. (4.8); however, to demonstrate the turbulence closure problem, only the non-linear term is required. In general, these equations are known as the vonKármán-Howarth (vK-H) equations of N-S theory. The technique we use to obtain the energy cascade (see next chapter) avoids this problem because it asks a much smaller question: “How does the energy of the turbulent system evolve?” In contrast, the closure problem encountered above stems from the more difficult question: “How does the power spectrum of the turbulence evolve?”

The auto-correlation function also lends insight into an important scale within the energy-containing range: the correlation length. Conceptually, we can describe the correlation length as the spatial scale at which the destruction of energy-containing source objects leads to smaller fluctuations generated within the fluid. This is the smallest scale of the energy-containing range. At scales smaller than the correlation length, fluctuations reflect in situ generation by “random” dynamics so as to demonstrate no reproducible coherence between the fluctuations (strictly speaking coherence is important in the interactions; however, the fluctuations are random from one realization to another). Another way to think of this is as the minimum separation needed for fluctuations to lose “knowledge” of their source dynamics. One definition of the correlation length is the e-folding distance, or the value of L where $R_{ij}(L)/R_{ij}(0) = 1/e$ (see Matthaeus et al. (1999) for examples, also Smith et al. (2001, 2006)). This estimate should agree fairly well with the scale at which the spectrum breaks and forms the “inertial range”.

A single spacecraft in the solar wind can only make measurements of length scales in terms of the time it takes the super-Alfvénic solar wind to convect structures passed the spacecraft. It is typically assumed, the times scale on which fluctuations evolve is much longer than the time it takes the fluctuations to convect past the spacecraft. The Taylor frozen-in-flow assumption is then used to directly relate the time scales measured by the spacecraft to length scales by way of the average solar wind flow speed. At 1 AU, the time scale associated with the correlation length for most measurements is a few hours; however, the quantity is generally not well measured. Recent studies, using multiple spacecraft to overcome the limitations of the Taylor frozen-in-flow assumption, find an anisotropic correlation length which is $\sim 2.7 \times 10^6$ km along the magnetic field direction and $\sim 1.5 \times 10^6$ km in the direction perpendicular to the magnetic field (Weygand et al., 2009).

In the solar wind, the power spectra for both magnetic and velocity fluctuations, when plotted as a function of the fluctuation frequency f , are characterized by an f^{-1} power law form over the range from $\sim 2.7 \times 10^{-6}$ to 8.0×10^{-5} Hz. This is the energy-containing range of the solar wind. Figure 4.2 plots magnetic power spectra for 5 intervals of solar wind data. The spectra are multiplied by the frequency, so that horizontal regions of the spectra indicate f^{-1} power laws. Vertical lines mark f^{-1} regions. Matthaeus and Goldstein (1986) argue the f^{-1} spectrum seen in the interplanetary energy-containing range is the result of the superposition of uncorrelated energy-containing signals reminiscent of the f^{-1} “noise” present in other fields of study.

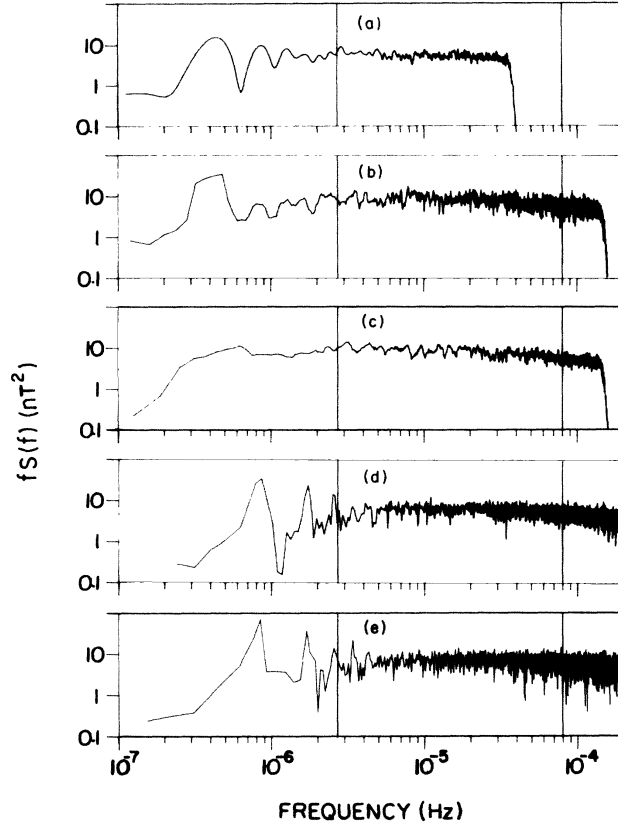


Figure 4.2: Plot of magnetic power spectra multiplied by frequency for 5 intervals of solar wind data. (from the top) The five intervals are 214 days and 184 days of International Sun-Earth Explorer-3 data from 1978 and 1979, an interval of data from the Interplanetary Monitoring Platform from years 1967–1968, and two intervals from the OMNI dataset spanning from 1964–1974 and 1974–1984. Vertical lines denote the range of frequencies where an f^{-1} spectrum is present. This range corresponds to the energy-containing range of the solar wind. Figure reproduced from Matthaeus and Goldstein (1986).

4.3 Inertial Range Spectra

The inertial range is the subset of the interplanetary spectrum at intermediate scales (i.e. scales smaller than the energy containing range where fluctuations still retain information about the source, but larger than the scales where dissipation plays a major role) where the main dynamic is the interaction of fluctuations and cascade of energy from scale to scale. Since dissipation of energy plays little to no role in this range and energy must be conserved, energy entering at one scale must subsequently be transmitted to another scale at a constant rate throughout the inertial range (Kolmogorov, 1941a). This rate is known as the energy cascade rate denoted by the symbol ϵ .

Many predictions exist for the spectrum of inertial range fluctuations in fluids and each predicted spectrum contains an associated prediction for the energy cascade rate. These predictions can be quite distinct. In hydrodynamics, Kolmogorov (1941a) predicts isotropic N-S turbulence should possess a spectrum in the form:

$$P(k) = C_K \epsilon^{2/3} k^{-5/3} \quad (4.9)$$

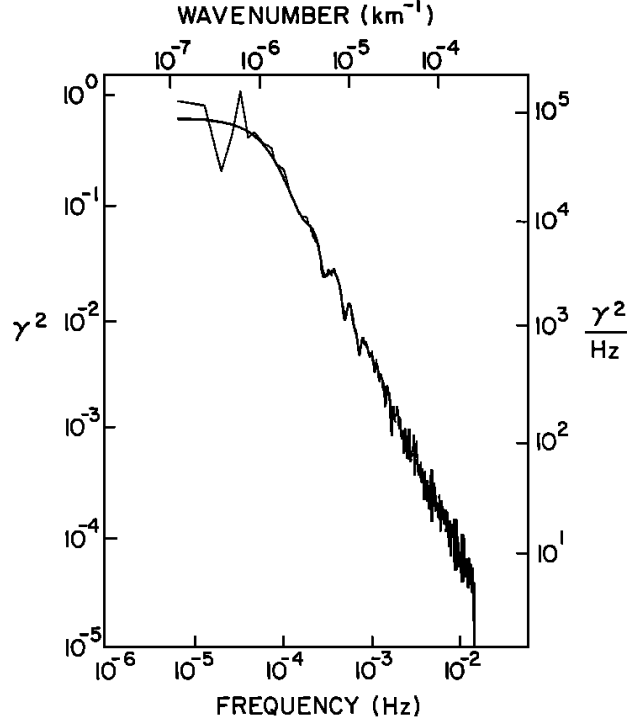


Figure 4.3: Example of a magnetic field power spectrum in the inertial range computed using Voyager 1 data. A power law index of -1.73 ± 0.08 is seen over the wave number range from 10^{-6} km^{-1} to $3 \times 10^{-4} \text{ km}^{-1}$. In terms of frequency this corresponds to $\sim 5 \times 10^{-5} \text{ Hz}$ to $\sim 10^{-2} \text{ Hz}$, which approximately matches up with the end of the energy containing range in Figure 4.2. Figure reproduced from Matthaeus and Goldstein (1982a).

where $P(k)$ is the turbulent power integrated over wave numbers with magnitude from $|k|$ to $|k+dk|$, $C_K \simeq 1.6$ is the so-called “Kolmogorov constant”, and ϵ is the rate of energy cascade per unit mass through the spectrum. The constant C_K has to be determined by experiment (e.g., Sreenivasan, 1995). The associated energy cascade rate is given by $\epsilon \sim u_k^2/\tau_{nl}$ where u_k is the characteristic velocity fluctuation associated with scale $k = 2\pi/L$. The characteristic nonlinear time is $\tau_{nl} \equiv (u_k k)^{-1}$.

It has been argued that MHD turbulence should follow the same spectral form as the Kolmogorov prediction (Fyfe et al., 1977; Biskamp and Müller, 2000; Mininni et al., 2005). Numerous authors have argued for a collapse to two-dimensions (2D) in MHD where only wave vectors perpendicular to the mean magnetic field contain significant amounts of turbulent energy (e.g., Shebalin et al., 1983; Ghosh et al., 1998b; Oughton et al., 1994; Matthaeus et al., 1996a) and that the 2D spectrum should be governed by Kolmogorov scaling (Montgomery and Turner, 1981; Goldreich and Sridhar, 1995). Dasso et al. (2005) shows that the large-scale fluctuations within the inertial range at 1 AU are quasi-2D in slow wind intervals and quasi-1D in fast wind intervals. Hamilton et al. (2008) show that the bulk of the magnetic fluctuation energy is quasi-2D at small scales within the inertial range.

However, unlike hydrodynamics and 2D MHD perpendicular to the mean magnetic field, 3D MHD is capable of supporting Alfvén waves. Iroshnikov (1964) and Kraichnan (1965) predict that the interaction of oppositely propagating Alfvén waves in isotropic MHD tur-

bulence should possess an inertial range spectrum of the form:

$$P(k) = A_{IK}(\epsilon V_A)^{1/2} k^{-3/2} \quad (4.10)$$

where $A_{IK} = C_K^{3/4} \simeq 1.4$ (Matthaeus and Zhou, 1989) and $V_A = B_0/\sqrt{\mu_0\rho}$ is the Alfvén speed seen in Eq. (3.23). The associated rate of energy cascade is given by E_k/τ_A where E_k is the characteristic total energy fluctuation (kinetic + magnetic) associated with scale k . The characteristic Alfvén time is $\tau_A \equiv (\mathbf{V}_A \cdot \mathbf{k})^{-1}$. Boldyrev (2005, 2006) predict a $-3/2$ spectral form for the cascade of energy in the direction perpendicular to the mean magnetic field.

Figure 4.3 shows an example of the power spectrum for magnetic field fluctuations. The spectrum is computed using data from the Voyager 1 spacecraft shortly after launch, when it was at approximately 1 AU. A power law spectrum of $k^{-1.73 \pm 0.08}$ is seen over the wave number range from 10^{-6} to $3 \times 10^{-4} \text{ km}^{-1}$ (Matthaeus and Goldstein, 1982a). This power law index is within one σ of the Kolmogorov prediction of $k^{-5/3}$. However, as is discussed in Section 4.5, the turbulent solar wind system is likely far more complex than either of these spectral predictions.

4.4 Dissipation Range Spectra

The high-frequency end of the inertial range spectrum terminates in a steepened form we call the dissipation range in analogy with traditional hydrodynamics. In hydrodynamics, dissipation is provided by the viscous term $\nu \nabla^2 \mathbf{v}$ in the N-S equation, which can be rewritten in wave vector notation as $-\nu k^2 \mathbf{v}_\mathbf{k}$. In a turbulent system, this dissipative term is negligible within the inertial range and only becomes dominant at small system scales leading to energy dissipation at the smallest spatial (largest k) scales. Hydrodynamics generally takes the viscosity ν to be constant and the resulting dissipation range spectrum is characterized by an exponential form (Frisch, 1995; Pope, 2000).

In the solar wind, the power spectrum begins to steepen from the inertial range predictions at scales comparable to the ion cyclotron frequency (Behannon, 1975; Goldstein et al., 1994). In Section 3.4, we state the MHD description of a plasma breaks down at scales where the cyclotron motions of the particles become important. As such, many argue dissipation in the solar wind is not provided by the viscosity ν and magnetic diffusivity η of the MHD equations, but instead by kinetic processes such as cyclotron and Landau damping. A review of the resonant and damping phenomena present in the kinetic description of a plasma is found in Chapter 12 of Kivelson and Russell (1995).

The kinetic dissipation processes are significantly more complicated than the simple form seen in hydrodynamics and there is no reason to expect the formation of an exponential dissipation spectrum in the solar wind. In fact, an exponential decay spectrum is not observed in the solar wind until electron scales and a general steepening of the spectrum to a new power law form is observed from ~ 0.2 to $\sim 3 \text{ Hz}$. This steepened power law is followed by a less steep spectrum that some have argued may be the onset of a second electron-based inertial range (Stawicki et al., 2001; Bale et al., 2005; Alexandrova et al., 2009; Sahraoui et al., 2009, 2010).

The top panel of Figure 4.4 shows an example of the steeping of the magnetic power spectrum from the inertial range to the dissipation range computed using data from the ACE spacecraft. The inertial range shows a power law form of $f^{-1.57 \pm 0.1}$, which steepens to

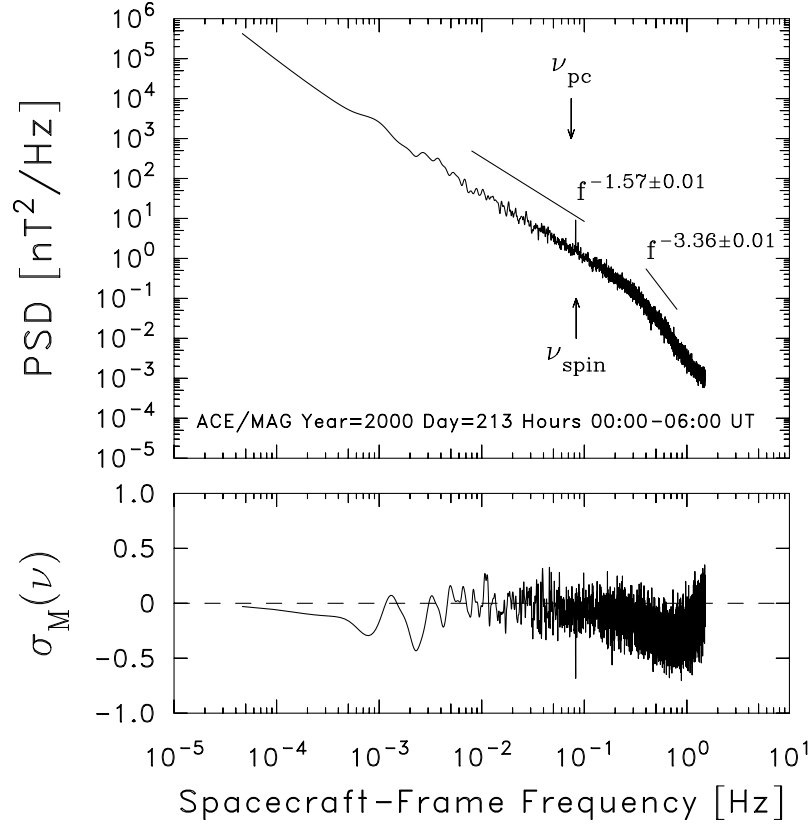


Figure 4.4: (top) Example of the steepening of the inertial range magnetic spectrum to the dissipation range spectrum. The spectrum is computed using ACE spacecraft data. The spectrum “breaks” from a power law index of -1.57 ± 0.01 to a power law index of -3.36 ± 0.01 at approximately 0.2 Hz. (bottom) The spectrum of magnetic helicity. The dip in the spectrum beginning at approximately 0.2 Hz is an indication of dissipation due to cyclotron damping. Figure reproduced from Hamilton et al. (2008).

a power law of $f^{-3.36 \pm 0.1}$ at ~ 0.2 Hz, indicating the onset of the dissipation range (Hamilton et al., 2008). The bottom panel shows a spectrum of the magnetic helicity. The dip in the spectrum present at ~ 0.2 Hz is an indication of the onset of dissipation due to cyclotron damping.

While the dissipative processes provide the mechanism through which solar wind heating occurs, for the remainder of this paper, we remain unconcerned with the exact mechanisms through which dissipation occurs. We instead assume dissipative processes are present and capable of transferring wave energy into heat and choose to ask the question, “Is the turbulent cascade of energy through the inertial range capable of providing the energy necessary for solar wind heating?”

4.5 Problems

None of the theoretical predictions for the turbulent power spectrum are seen in their true form in the solar wind at 1 AU for a great many reasons.

First, all of the above predictions address the total energy only, but implicitly assume

that the velocity and magnetic spectra possess a common form. They don't. Podesta et al. (2006, 2007) show that the velocity spectrum has, on average, a $-3/2$ index at 1 AU while the magnetic spectrum at 1 AU has the familiar $-5/3$ index (Coleman, 1968; Matthaeus and Goldstein, 1982b; Smith et al., 2006). Roberts (2007) argues that the velocity index approaches $-5/3$ by 5 AU. Borovsky (2008) argues that the spectral form is partially dictated by the presence of discontinuities that he argues are of solar origin and not arising from turbulence.

Second, the geometry of the underlying wave vectors have long been in question. Matthaeus et al. (1990) compare and combine correlation functions as a function of Θ_{BR} , the angle between the mean IMF and the radial direction (solar wind flow direction), under the assumption that a universal functional form exists spanning many solar wind conditions, and find the so-called “Maltese Cross” result showing that the turbulence is a combination of wave vectors approximately parallel and approximately perpendicular to the mean IMF. Dasso et al. (2005) breaks apart the Maltese Cross into fast and slow wind intervals, finding that the geometry of the large-scale inertial range component near the correlation length is approximately field-aligned in the fast wind and perpendicular in the slow wind. In truth, both conditions are a mixture of both wave vector types, but in each instance one vector orientation dominates.

Third, Goldreich and Sridhar (1995) argue that the perpendicular cascade will deplete the field-aligned wave vectors and produce a “notch” in the measured spectrum when the mean IMF is parallel to the flow. The theory of Goldreich and Sridhar (1995) builds on decades of research predicting the dominance of a perpendicular cascade (Fyfe et al., 1977; Shebalin et al., 1983; Higdon, 1984; Ghosh et al., 1998b; Oughton et al., 1994; Matthaeus et al., 1996a). Horbury et al. (2008) and Podesta (2009) claim to find this notch at frequencies from 0.01 to 0.1 Hz. Tessein et al. (2009) show that the velocity spectral index is centered on -1.4 and that both the magnetic and velocity forms are independent of Θ_{BR} , the angle between the mean magnetic field and the solar wind velocity, at larger inertial range scales (see also Sari and Valley, 1976). MacBride et al. (2008) shows a weak cascade of energy parallel to the mean magnetic field which reaches beyond the theory of Goldreich and Sridhar (1995).

Fourth, recent observations by Sahraoui et al. (2009, 2010) claim that the inertial range spectrum is comprised of highly perpendicular wave vectors that avoid both cyclotron and Landau damping to create an apparent “dissipation range” without dissipation until the cascade is eventually terminated at electron scales.

No theories currently predict a rate of energy cascade based on spectral properties with this high degree of complexity. These observations strongly suggest a non-stationary spectrum that is evolving toward something other than what it is and this is beyond the scope of present spectral-based predictions for the energy cascade rate.

Chapter 5

Third-Moment Theory

The simplest and most commonly used method for extracting ϵ , the rate of energy cascade per unit mass from large to small-scale fluctuations, has been to compute the power spectrum and obtain ϵ from theories that link it to the spectral amplitude. Due to the closure problem, the power spectra method for determining ϵ requires one to make assumptions on the underlying dynamics and geometry of the turbulence which can be poorly resolved and recent analyses have raised issues with the conclusions derived in this manner.

The third-moment method for determining ϵ , which relates ϵ to the third-order structure function of turbulent fluctuations, has had a long standing and well tested history in hydrodynamics dating back to the 1940's (Kolmogorov, 1941b). This method comes from examining the Navier-Stokes equation, which governs the fluid dynamics of a hydrodynamic system, and is true regardless of the underlying dynamics of the turbulent interaction process. This method is extended to MHD by Politano and Pouquet (1998a,b), which allows for the application of third-moment theory to the solar wind and a better understanding of the role turbulence plays in the heliosphere.

In this chapter, we begin by demonstrating one derivation of the simpler hydrodynamic third-moment expressions in order to demonstrate the basic principles of the theory and then move on to discuss how these concepts are applied to the more complex magnetohydrodynamic case, which is the main focus of this thesis. For both hydrodynamics and MHD, an isotropic geometry for the turbulent fluctuations is discussed and, in MHD, an anisotropic “hybrid” geometry with respect to the orientation of the mean magnetic field is also described. Basic considerations which are required for the application of the MHD expressions to the solar wind are also mentioned.

5.1 Hydrodynamic Third-Moment Theory

The aim of third-moment theory is to obtain an exact relationship for the rate of energy cascade through the inertial range. Recall from Section 4.3 that Kolmogorov (1941a) predicts, using phenomenological arguments, that the hydrodynamic energy cascade rate should be related to the velocity fluctuations u_k at scale L by the relationship:

$$\epsilon \sim u_k^2 / \tau_{nl} \sim u_k^3 / L \quad (5.1)$$

where $\tau_{nl} \equiv (u_k k)^{-1}$. It is, therefore, not unexpected that the energy cascade rate should be related to the “third-moment” or “third-order structure function” of velocity fluctuations.

There are a variety of methods, that can be used to explicitly derive the third-moment formalism. Here, we present one method, which is analogous to the technique used by Politano and Pouquet (1998b) for MHD turbulence and Wan et al. (2009) for the MHD shear formalism we use in Chapter 9.

We begin by obtaining an expression for the mean rate of energy dissipation in a hydrodynamic system by again considering the N-S equation seen in Eq. (4.1). We re-express the N-S equation in Einstein summation notation, where the subscripts i and j denote the components of vectors and sums are applied over repeated indices. In this notation, the N-S equation at the position \mathbf{x} becomes:

$$\frac{\partial v_i(\mathbf{x})}{\partial t} + v_j(\mathbf{x}) \frac{\partial}{\partial x_j} v_i(\mathbf{x}) = -\frac{1}{\rho} \frac{\partial}{\partial x_i} P(\mathbf{x}) + \nu \frac{\partial}{\partial x_j} \frac{\partial}{\partial x_j} v_i(\mathbf{x}) \quad (5.2)$$

We can also write the N-S equation at another position $\mathbf{x}' = \mathbf{x} + \mathbf{L}$, where \mathbf{L} is the “lag” vector separating the positions \mathbf{x} and \mathbf{x}' :

$$\frac{\partial v_i(\mathbf{x}')}{\partial t} + v_j(\mathbf{x}') \frac{\partial}{\partial x'_j} v_i(\mathbf{x}') = -\frac{1}{\rho} \frac{\partial}{\partial x'_i} P(\mathbf{x}') + \nu \frac{\partial}{\partial x'_j} \frac{\partial}{\partial x'_j} v_i(\mathbf{x}') \quad (5.3)$$

Note that the positions \mathbf{x} and \mathbf{x}' are any two arbitrary positions and the lag vector \mathbf{L} is simply the difference between these two positions.

We are interested in analyzing the turbulent fluctuations, so we consider the difference between Eq. (5.3) and Eq. (5.2):

$$\begin{aligned} \frac{\partial \delta v_i(\mathbf{L})}{\partial t} + v_j(\mathbf{x}') \frac{\partial}{\partial x'_j} \delta v_i(\mathbf{L}) + v_j(\mathbf{x}) \frac{\partial}{\partial x_j} \delta v_i(\mathbf{L}) \\ = -\frac{1}{\rho} \frac{\partial}{\partial x'_i} \delta P(\mathbf{L}) - \frac{1}{\rho} \frac{\partial}{\partial x_i} \delta P(\mathbf{L}) + \nu \frac{\partial}{\partial x'_j} \frac{\partial}{\partial x'_j} \delta v_i(\mathbf{L}) + \nu \frac{\partial}{\partial x_j} \frac{\partial}{\partial x_j} \delta v_i(\mathbf{L}) \end{aligned} \quad (5.4)$$

where $\delta v_i(\mathbf{L}) = v_i(\mathbf{x}') - v_i(\mathbf{x})$ and $\delta P(\mathbf{L}) = P(\mathbf{x}') - P(\mathbf{x})$. In Eq. (5.4), we note \mathbf{x} and \mathbf{x}' are independent of each other, meaning $\frac{\partial v_i(\mathbf{x}')}{\partial x_j} = 0$ and $\frac{\partial v_i(\mathbf{x})}{\partial x'_j} = 0$. The same is also true of the pressure terms. Therefore, the terms within the spatial derivatives in the above equation were written as derivatives of $\delta v_i(\mathbf{L})$ and $\delta P(\mathbf{L})$.

We now multiply Eq. (5.4) by $\delta v_i(\mathbf{L})$ and average to obtain an equation for the mean energy per unit mass in turbulent hydrodynamic fluctuations. By using the chain rule to manipulate the derivatives and noting derivatives are linear operators that can be pulled out of the averaging, we obtain the equation:

$$\begin{aligned} \frac{\partial}{\partial t} \langle [\delta v_i(\mathbf{L})]^2 \rangle + \left\langle v_j(\mathbf{x}') \frac{\partial}{\partial x'_j} [\delta v_i(\mathbf{L})]^2 \right\rangle + \left\langle v_j(\mathbf{x}) \frac{\partial}{\partial x_j} [\delta v_i(\mathbf{L})]^2 \right\rangle \\ = -\frac{2}{\rho} \left\langle \delta v_i(\mathbf{L}) \frac{\partial}{\partial x'_i} \delta P(\mathbf{L}) \right\rangle - \frac{2}{\rho} \left\langle \delta v_i(\mathbf{L}) \frac{\partial}{\partial x_i} \delta P(\mathbf{L}) \right\rangle \\ + \nu \frac{\partial}{\partial x'_j} \frac{\partial}{\partial x'_j} \langle [\delta v_i(\mathbf{L})]^2 \rangle + \nu \frac{\partial}{\partial x_j} \frac{\partial}{\partial x_j} \langle [\delta v_i(\mathbf{L})]^2 \rangle \\ - 2\nu \left\langle \left[\frac{\partial}{\partial x'_j} v_i(\mathbf{x}') \right]^2 \right\rangle - 2\nu \left\langle \left[\frac{\partial}{\partial x_j} v_i(\mathbf{x}) \right]^2 \right\rangle \end{aligned} \quad (5.5)$$

where $\langle \dots \rangle$ denotes an ensemble average and the last four terms on the r.h.s. of this equation are derived from the last two terms on the r.h.s. of Eq. (5.4).

By applying the condition of incompressibility ($\frac{\partial}{\partial x_j} v_j(\mathbf{x}) = 0$), we can pull the derivatives out of the averages in the last two terms on the l.h.s. and first two terms on the r.h.s. of Eq. (5.5). We can make use of homogeneity to say $\frac{\partial}{\partial x'_j} \langle \dots \rangle = -\frac{\partial}{\partial x_j} \langle \dots \rangle = \frac{\partial}{\partial L_j} \langle \dots \rangle$. Homogeneity also allows us to combine the last two terms on the r.h.s. of Eq (5.5) and results in the cancellation of the two pressure terms, resulting in the equation:

$$\frac{\partial}{\partial t} \langle [\delta v_i(\mathbf{L})]^2 \rangle + \frac{\partial}{\partial L_j} \langle \delta v_j(\mathbf{L}) [\delta v_i(\mathbf{L})]^2 \rangle = 2\nu \frac{\partial}{\partial L_j} \frac{\partial}{\partial L_j} \langle [\delta v_i(\mathbf{L})]^2 \rangle - 4\nu \left\langle \left[\frac{\partial}{\partial L_j} v_i(\mathbf{x}) \right]^2 \right\rangle \quad (5.6)$$

As it turns out, $\nu \left\langle \left[\frac{\partial}{\partial L_j} v_i(\mathbf{x}) \right]^2 \right\rangle$ is identified as the mean rate of energy dissipation, so that the last term on the r.h.s. of Eq. 5.6 is equivalent to -4 times the mean energy dissipation rate (Frisch, 1995). We are interested in determining the turbulent energy cascade rate ϵ in the inertial range, which should be equivalent to the mean energy dissipation rate for turbulence that has reached a statistically steady state. This is simply a statement that, if the average energy at each scale is unchanging in time, then the energy entering the inertial range should be equivalent to the energy leaving the inertial range.

We, therefore, enforce the following two constraints: 1) We assume that the turbulence has reached a steady state, so that the first term on the l.h.s. becomes zero and the last term on the r.h.s. becomes -4ϵ . 2) We constrain ourselves to only consider the inertial range, so that the remaining dissipative term (the first term on the r.h.s.) is zero. Recall that a key feature of turbulence is an extended inertial range where dissipation is negligible. These constraints leave us with the following equation for the energy cascade rate:

$$-4\epsilon = \frac{\partial}{\partial L_j} \langle \delta v_j(\mathbf{L}) [\delta v_i(\mathbf{L})]^2 \rangle \quad (5.7)$$

Re-expressing the above equation in vector notation, gives us the Kármán-Howarth-Monin (KHM) relation for homogeneous hydrodynamic turbulence (Monin, 1959; Monin and Yaglom, 1975):

$$-4\epsilon = \nabla_{\mathbf{L}} \cdot \langle \delta \mathbf{v}(\mathbf{L}) |\delta \mathbf{v}(\mathbf{L})|^2 \rangle \quad (5.8)$$

where $\nabla_{\mathbf{L}} \cdot$ is a divergence with respect to the lag vector \mathbf{L} . This is general and true for spatial scales nominally regarded to be within the inertial range without regard for spectral form, wave vector anisotropy, or fluctuation anisotropy (page 78 of Frisch, 1995).

In the limit of isotropic turbulence, one can integrate Eq. (5.8) over a sphere of radius $L = |\mathbf{L}|$ and obtain a “4/3 Law” of the Yaglom (1949) form for the energy cascade rate:

$$\langle \delta v_L(\mathbf{L}) |\delta \mathbf{v}(\mathbf{L})|^2 \rangle = -\frac{4}{3} \epsilon^{HD} |\mathbf{L}| \quad (5.9)$$

where v_L is the component of the velocity fluctuation along the separation vector \mathbf{L} such that $v_L \equiv \mathbf{v} \cdot \mathbf{L}/L$ and ϵ^{HD} is the hydrodynamic rate of energy cascade. The r.h.s of Eq. 5.9 is often referred to as a “third-moment” and is a generalization of the third-order structure functions traditionally used in hydrodynamics. This form of hydrodynamic third-moment theory is most analogous to the MHD formalism discussed in the remaining sections of this chapter.

Historically, in hydrodynamics, third-moment derivations proceed by examining the time derivative of the two-point auto-correlation function in a similar manner to the analysis in Eq. (4.8). While not shown here, Kármán and Howarth (1938) obtain the so called

“Kármán-Howarth” equation relating the energy cascade rate to correlation functions of the velocity. This expression is true for homogeneous, isotropic turbulence. The KHM relation seen in Eq. (5.8) is simply a generalization of the Kármán-Howarth equation to anisotropic hydrodynamics.

Kolmogorov (1941b) uses the Kármán-Howarth equation to obtain the “Kolmogorov 4/5 Law” relating the inertial range energy cascade rate in homogeneous, isotropic turbulence to a third-order structure function of velocity fluctuations:

$$S_3^{HD}(\mathbf{L}) \equiv \langle [v_L(\mathbf{x} + \mathbf{L}) - v_L(\mathbf{x})]^3 \rangle = -\frac{4}{5}\epsilon^{HD}|\mathbf{L}| \quad (5.10)$$

Unlike Eq. (5.9), this expression is only written in terms of $\delta v_L(\mathbf{L})$. It can be shown that both this equation and Eq. (5.9) are consistent expressions for isotropic, hydrodynamic turbulence. The Kolmogorov 4/5 Law is the more traditional expression for hydrodynamic turbulence and, for the remainder of this paper, the Kolmogorov Law is what is meant when we refer to the hydrodynamic third-moment expression.

5.2 Isotropic MHD Third-Moment Theory

Politano and Pouquet (1998a,b) extend Eq. (5.8)–(5.10) to incompressible MHD turbulence using the Elsässer variables. Recall the MHD equations written in terms of the Elsässer variables seen in Eq. (3.8). These equations are of the same form as the N-S equation and it, therefore, stands to reason that the same derivation performed in Eq. (5.2)–(5.7) can equivalently be applied to this formulation of the MHD equations. The only difference is that the MHD version involves two separate equations for \mathbf{Z}^+ and \mathbf{Z}^- instead of one equation for \mathbf{v} . By defining the vector:

$$\mathbf{D}_3^\pm(\mathbf{L}) \equiv \langle \delta \mathbf{Z}^\mp(\mathbf{L}) |\delta \mathbf{Z}^\pm(\mathbf{L})|^2 \rangle \quad (5.11)$$

we can derive from the MHD equations, the MHD analog of the KHM relation, using the same method we describe for hydrodynamics:

$$\nabla_{\mathbf{L}} \cdot \mathbf{D}_3^\pm(\mathbf{L}) = -4\epsilon^\pm \quad (5.12)$$

where $\delta \mathbf{Z}^\pm(\mathbf{L}) \equiv \mathbf{Z}^\pm(\mathbf{x} + \mathbf{L}) - \mathbf{Z}^\pm(\mathbf{x})$ and ϵ^\pm denote the rate of cascade of the fluctuation energy related to $|\delta \mathbf{Z}^\pm|^2$. Due to this convention, the total energy cascade rate per unit mass, ϵ^T , is given by

$$\epsilon^T = (\epsilon^+ + \epsilon^-)/2. \quad (5.13)$$

We will generally suppress the superscript “ T ”.

The Politano and Pouquet (1998b) expression for energy cascade in isotropic MHD turbulence follows from application of the divergence in spherical coordinates:

$$-4\epsilon^\pm = \left(\frac{1}{L^2}\right) \frac{\partial}{\partial L} \left(L^2 D_3^\pm(L)\right) + \frac{1}{L \sin \Theta} \frac{\partial}{\partial \Theta} \left(\sin \Theta D_3^\pm(\Theta)\right) + \frac{1}{L \sin \Theta} \frac{\partial}{\partial \Phi} D_3^\pm(\Phi) \quad (5.14)$$

In isotropy, the angular dependence is zero and Eq. (5.14) integrates to a “4/3 law”:

$$\begin{aligned} D_{3,ISO}^\pm(L) &\equiv \langle \delta Z_L^\mp(L) |\delta \mathbf{Z}^\pm(L)|^2 \rangle \\ &= -(4/3)\epsilon_{ISO}^\pm L \end{aligned} \quad (5.15)$$

where Z_L^\mp is the component of \mathbf{Z}^\mp in the direction of the lag separation vector. Using Eq. (5.13) and (5.15), we define a total third-moment in the isotropic MHD formalism as:

$$D_3(L) \equiv \frac{D_{3,ISO}^+(L) + D_{3,ISO}^-(L)}{2} = -(4/3)\epsilon_{ISO}L \quad (5.16)$$

5.2.1 Isotropic Application to the Solar Wind

In the solar wind, it is difficult to obtain measurements of the velocity and magnetic field at many different positions as is required to evaluate Eq. (5.15). However, for single spacecraft measurements, we can make use of fact that the solar wind flows past the spacecraft in the radial direction with a super-Alfvénic velocity V_{SW} , carrying velocity and magnetic field fluctuations along with it. Using the Taylor frozen-in-flow assumption, we postulate that the time it takes for fluctuations to significantly evolve is much longer than the time it takes for the bulk solar wind velocity to carry them past the spacecraft. As a result, measurements separated by a positive time lag τ can be associated with measurements separated in position by a lag vector with magnitude $L = V_{SW}\tau$ and directed in the radial direction. Eq. (5.15) can be modified in the following way:

$$\begin{aligned} D_{3,ISO}^\pm(\tau) &\equiv \langle \delta Z_R^\mp(\tau) |\delta \mathbf{Z}^\pm(\tau)|^2 \rangle \\ &= +(4/3)\epsilon_{ISO}^\pm V_{SW}\tau \end{aligned} \quad (5.17)$$

where the subscript “ R ” denotes the radial component directed from the Sun’s center to the point of measurement and the sign change results from positive time lags corresponding to negative spatial lags relative to the radial direction.

We also add one more complication to the analysis: Z^- (Z^+) refers to propagation parallel (anti-parallel) to the mean magnetic field. In the solar wind, the mean field can be directed sunward (in) or anti-sunward (out), but the dominant propagation direction is consistently anti-sunward (Belcher and Davis, 1971; Smith et al., 1995). Therefore, we choose to collect D_3^\pm so as to average D_3^{out} and D_3^{in} according to the direction of propagation relative to the Sun. As a result $D_{3,ISO}^\pm \rightarrow D_{3,ISO}^{out/in}$, $\epsilon_{ISO}^\pm \rightarrow \epsilon_{ISO}^{out/in}$, etc.

5.3 Anisotropic MHD Third-Moment Theory

Matthaeus et al. (1990), Dasso et al. (2005), and Hamilton et al. (2008) all reveal significant anisotropies associated with the multi-dimensional correlation function or spectrum of wave vectors. For this reason, and because of the theoretical considerations predicting anisotropic spectra outlined in Chapter 4, MacBride et al. (2008) uses Eq. (5.12) to derive expressions for axisymmetric turbulence about a mean magnetic field. If we write $\mathbf{D}_3^\pm(\mathbf{L})$ in cylindrical coordinates the components become:

$$D_{3,\perp}^\pm \equiv \langle \delta Z_\perp^\mp |\delta \mathbf{Z}^\pm|^2 \rangle \quad (5.18)$$

$$D_{3,\parallel}^\pm \equiv \langle \delta Z_\parallel^\mp |\delta \mathbf{Z}^\pm|^2 \rangle \quad (5.19)$$

where the \perp and \parallel denote the components of the vector perpendicular and parallel to the mean magnetic field respectively. The axisymmetric form of Eq. (5.12) then becomes:

$$-4\epsilon^\pm = \left(\frac{1}{L_\perp}\right) \frac{\partial}{\partial L_\perp} (L_\perp D_{3,\perp}^\pm) + \frac{\partial}{\partial L_\parallel} D_{3,\parallel}^\pm. \quad (5.20)$$

where L_\perp is a lag in the direction perpendicular to the mean magnetic field and L_\parallel is a lag in the direction parallel to the mean magnetic field. The perpendicular and parallel components are sometimes referred to with the superscripts “2D” and “1D” in this thesis because the perpendicular component involves two orthogonal spatial dimensions and the parallel component involves only one spatial dimension. At this point, the two derivatives on the r.h.s. need only sum to produce a constant rate of cascade that is independent of lag \mathbf{L} . We can make a further assumption for simplicity that:

$$-4\epsilon_\perp^\pm \equiv \left(\frac{1}{L_\perp}\right) \frac{\partial}{\partial L_\perp} (L_\perp D_{3,\perp}^\pm) \quad (5.21)$$

$$-4\epsilon_\parallel^\pm \equiv \frac{\partial}{\partial L_\parallel} D_{3,\parallel}^\pm \quad (5.22)$$

Integrating the 2 dimensional Eq. (5.21) over a circle of radius L_\perp and the 1 dimensional Eq. (5.22) out to the lag L_\parallel , gives the expressions:

$$\begin{aligned} D_{3,\perp}^\pm(L_\perp) &\equiv \langle \delta Z_\perp^\mp(L_\perp) |\delta \mathbf{Z}^\pm(L_\perp)|^2 \rangle \\ &= -2\epsilon_\perp^\pm L_\perp \end{aligned} \quad (5.23)$$

and

$$\begin{aligned} D_{3,\parallel}^\pm(L_\parallel) &\equiv \langle \delta Z_\parallel^\mp(L_\parallel) |\delta \mathbf{Z}^\pm(L_\parallel)|^2 \rangle \\ &= -4\epsilon_\parallel^\pm L_\parallel \end{aligned} \quad (5.24)$$

We define the total 2D cascade rate in accordance with Eq. (5.13) and take the total 2D third-moment to be:

$$D_3^{2D}(L_\perp) \equiv \frac{D_{3,\perp}^+(L_\perp) + D_{3,\perp}^-(L_\perp)}{2} = -2\epsilon^{2D} L_\perp \quad (5.25)$$

where $\epsilon^{2D} = (\epsilon_\perp^+ + \epsilon_\perp^-)/2$ is the total perpendicular cascade rate. Likewise, the total 1D third-moment is taken to be:

$$D_3^{1D}(L_\parallel) \equiv \frac{D_{3,\parallel}^+(L_\parallel) + D_{3,\parallel}^-(L_\parallel)}{2} = -4\epsilon^{1D} L_\parallel \quad (5.26)$$

where $\epsilon^{1D} = (\epsilon_\parallel^+ + \epsilon_\parallel^-)/2$ is the total parallel cascade rate.

We can also define an expression for the total axisymmetric “hybrid” cascade, such that:

$$\epsilon_{\text{hybrid}}^\pm = \frac{D_{3,\perp}^\pm}{2L_\perp} + \frac{D_{3,\parallel}^\pm}{4L_\parallel} \quad (5.27)$$

$$= \epsilon_\perp^\pm + \epsilon_\parallel^\pm \quad (5.28)$$

From the axisymmetric form, we recover the isotropic cascade if $\epsilon_\parallel^\pm = (1/2)\epsilon_\perp^\pm$ and $L_\perp = L_\parallel$, or:

$$\epsilon_{ISO}^\pm = \frac{D_\perp^\pm}{2L_\perp} + \frac{D_\parallel^\pm}{4L_\parallel} = \frac{3}{4} \frac{D_{ISO}^\pm}{L}. \quad (5.29)$$

From Eq. (5.13), the total hybrid energy cascade is given by $\epsilon_{\text{hybrid}}^T = (\epsilon_{\text{hybrid}}^+ + \epsilon_{\text{hybrid}}^-)/2$ and, as with Eq. (5.16), we can employ this equation along with Eq. (5.23) and (5.24) to define the total third-moment D_3^T at scale L in the hybrid formalism:

$$D_3^T(L) \equiv \frac{D_{3,\perp}^+(L_\perp = L) + D_{3,\perp}^-(L_\perp = L)}{4} + \frac{D_{3,\parallel}^+(L_\parallel = L) + D_{3,\parallel}^-(L_\parallel = L)}{8} \quad (5.30)$$

Here we assume $L_\perp = L_\parallel = L$. From this equation, we expect $D_3^T = \epsilon_{\text{hybrid}}^T L$. As with the isotropic case, the superscript “ T ” will typically be suppressed. We have separately imposed the assumption that ϵ_\perp^\pm and ϵ_\parallel^\pm are each independent of lag. This may not be true, but it does represent a simplification and useful starting point for the purpose of presentation and discussion.

5.3.1 Anisotropic Application to the Solar Wind

To apply this concept, we rotate the data to mean field coordinates (Belcher and Davis, 1971; Bieber et al., 1996):

$$\hat{\mathbf{e}}_{\mathbf{x}} \equiv (\hat{\mathbf{e}}_{\mathbf{R}} \times \hat{\mathbf{e}}_{\mathbf{B}}) / |\hat{\mathbf{e}}_{\mathbf{R}} \times \hat{\mathbf{e}}_{\mathbf{B}}|, \quad (5.31)$$

$$\hat{\mathbf{e}}_{\mathbf{y}} \equiv \hat{\mathbf{e}}_{\mathbf{z}} \times \hat{\mathbf{e}}_{\mathbf{x}}, \quad (5.32)$$

$$\hat{\mathbf{e}}_{\mathbf{z}} \equiv \hat{\mathbf{e}}_{\mathbf{B}}. \quad (5.33)$$

where $\hat{\mathbf{e}}_{\mathbf{R}}$ is the radial direction and $\hat{\mathbf{e}}_{\mathbf{B}}$ is the direction of the mean magnetic field. With a single spacecraft in the solar wind the $\hat{\mathbf{e}}_{\mathbf{y}}$ direction is the only perpendicular direction for which we have a measured nonzero lag because $\hat{\mathbf{e}}_{\mathbf{x}}$ is perpendicular to the wind velocity and gives no measured lag. In principle, any lag across the mean field direction could be used to measure the perpendicular cascade, but in this coordinate system only the $\hat{\mathbf{e}}_{\mathbf{y}}$ direction provides a finite lag perpendicular to the mean magnetic field. We also note that in the solar wind $L_\perp = V_{SW}\tau \sin(\Theta_{BR})$ and $L_\parallel = V_{SW}\tau \cos(\Theta_{BR})$ where Θ_{BR} is the angle between the radial direction and the direction of the mean field. Recall that the typical value for Θ_{BR} at 1 AU in the ecliptic plane is 45° due to the Parker spiral. The resulting form for the perpendicular cascade is:

$$D_{3,\perp}^\pm(\tau) \equiv \langle \delta Z_y^\mp(\tau) |\delta \mathbf{Z}^\pm(\tau)|^2 \rangle = 2\epsilon_\perp^\pm V_{SW}\tau \sin(\Theta_{BR}) \quad (5.34)$$

while the parallel cascade is given by:

$$D_{3,\parallel}^\pm(\tau) \equiv \langle \delta Z_z^\mp(\tau) |\delta \mathbf{Z}^\pm(\tau)|^2 \rangle = 4\epsilon_\parallel^\pm V_{SW}\tau \cos(\Theta_{BR}). \quad (5.35)$$

Likewise, Eq. (5.25), (5.26), and (5.30) are appropriately modified for application to the solar wind. The \parallel and \perp forms of the hybrid MHD cascade expression are independent and can be obtained simultaneously from the data (MacBride et al., 2008). As with the isotropic case, we again associate \mathbf{Z}^\pm with $\mathbf{Z}^{out/in}$ according to the direction of fluctuation propagation for all the same reasons and with the same effects mentioned in Section 5.2.1.

The core expressions given by Eq. (5.8) (for incompressible hydrodynamics) and (5.12) (for incompressible MHD) are considered rigorous within the inertial range scales regardless of the form taken by the energy spectrum (Frisch, 1995; Biskamp, 2003). Variations derived from geometry considerations (isotropic, hybrid, etc.) are refinements that may or may not apply in some cases.

Chapter 6

Early Third-Moment Applications in the Solar Wind

As discussed in Chapters 3 and 4, there is strong evidence that turbulent processes may be at work in the solar wind. While the effectiveness of third-moment expressions in traditional hydrodynamic situations is well established, the application of the MHD analogues to the solar wind presents new challenges that largely stem from the restrictions of single spacecraft data. Sections 5.2.1 and 5.3.1 briefly describe some of the considerations necessary to apply the MHD third-moment expressions to single spacecraft solar wind measurements. The analyses of MacBride et al. (2005) and MacBride et al. (2008) represent two of the early studies, which demonstrate the viability of using third-order structure functions to compute the energy cascade rate in the solar wind.

6.1 MacBride et al. 2005

MacBride et al. (2005) perform a preliminary analysis using a generalized form of the isotropic MHD third-moment expression. They compute cascade rates for selected 27 day intervals of magnetic field and plasma data from the ACE spacecraft, as well as, attempt an analysis of a 7 yr period of data. Three important conclusions are drawn: 1) the isotropic MHD third-moment follows a linear scaling with lag in several selected intervals of data as is expected by turbulence theory, 2) the sign of ϵ , as computed from this expression, is positive, which is consistent with the expected cascade of energy from large to small scales, and 3) energy cascade rates computed from the isotropic third-moment roughly agree with cascade rates inferred from power spectra. Not only do these conclusions demonstrate the viability of applying third-moments to the solar wind, but the results also lend support to the assertion that turbulent processes are at work in the solar wind.

The isotropic MHD third-moment expression seen in Eq. (5.17) assumes that turbulent interactions occur in all three spatial dimensions. This expression can be generalized to turbulence in any number of dimensions, giving the relation (Politano and Pouquet, 1998b):

$$\begin{aligned} D_{3,ISO}^{\pm}(\tau) &\equiv \left\langle \delta Z_R^{\mp}(\tau) |\delta \mathbf{Z}^{\pm}(\tau)|^2 \right\rangle \\ &= +(4/d) \epsilon_{ISO}^{\pm} V_{SW} \tau \end{aligned} \tag{6.1}$$

where d represents the dimension of the turbulence. Recall from Section 4.3 that many argue solar wind turbulence should collapse to 2D ($d = 2$) in the direction perpendicular to the magnetic field.

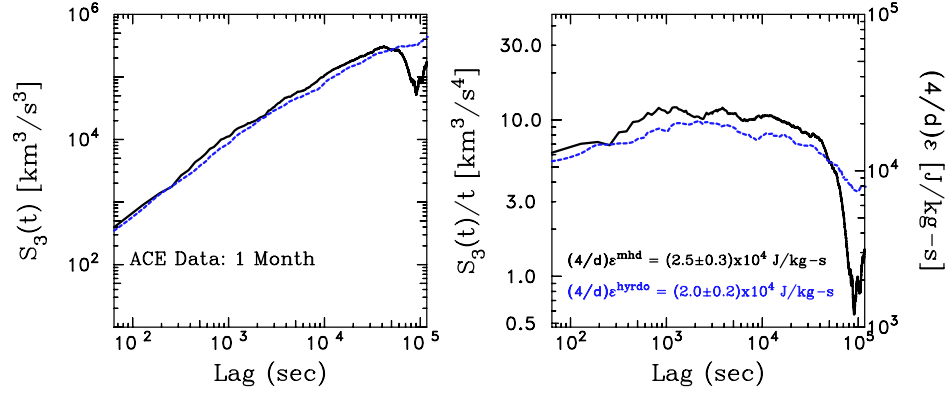


Figure 6.1: (left) Plot of hydrodynamic (dashed blue) and isotropic MHD (solid black) third-moments for the 27 day period of ACE data spanning from day 157 to 183 of year 2000. Note the linear scaling with lag as predicted by turbulence theory and positive slope indicating a cascade of energy from large to small scales. (right) Plot of third-moments divided by time lag τ . Figure reproduced from MacBride et al. (2005).

The MacBride et al. (2005) analysis first considers one Carrington rotation (~ 27 days) of ACE spacecraft magnetic field and plasma data spanning from day 157 to day 183 of year 2000. The isotropic MHD third-moment, isotropic HD third-moment, and 91 magnetic power spectra are computed using this data. Figure 6.1 plots the HD and MHD third-moments as a function of lag (or more specifically, the time separation τ). Note that, aside from the down turn seen in the MHD structure function near 5×10^4 s, both the HD and MHD forms show a linear scaling with lag. The structure functions also have a positive slope when plotted against τ indicative of a cascade of energy from large to small scales.

Figure 6.1 also plots the structure functions divided by lag. This should be a constant value in the inertial range and proportional to the energy cascade rate. The analysis finds that the average value of $(4/d)\epsilon$ from the MHD and HD expressions are 2.5×10^4 and 2.0×10^4 J/kg-s respectively. Assuming 2D turbulence these become 1.25×10^4 J/kg-s for isotropic MHD and 1.00×10^4 for isotropic HD. The fact that the MHD and HD expressions produce similar results suggests longitudinal solar wind speed fluctuations, at least in this specific interval, dominate the MHD expression. Magnetic power spectra are also produced for 91 subintervals within the same Carrington rotation. The average energy cascade rate inferred from the magnetic power spectra over this interval is 1.2×10^4 J/kg-s. This is reasonably close considering the power spectrum method relies on assumptions of the underlying turbulent dynamics, which are unclear in the solar wind.

MacBride et al. (2005) also experiments with detrending and stationarity testing in an effort to analyze longer intervals of data. The process of detrending involves subtracting large-scale trends from the data in order to isolate the turbulent fluctuations. This concept is employed again in the analysis described in Chapter 9. Stationarity testing involves analyzing only intervals of data in which the statistical properties are determined to be “stationary” or invariant in time. There are diverse methods for doing this. A rigorous “stationarity of the mean” analysis by Matthaeus and Goldstein (1982b) tests the statistical convergence of the mean field with respect to data volume. Experiments with this technique by MacBride et al. (2005) are less than satisfying. A convergence of the variance test,

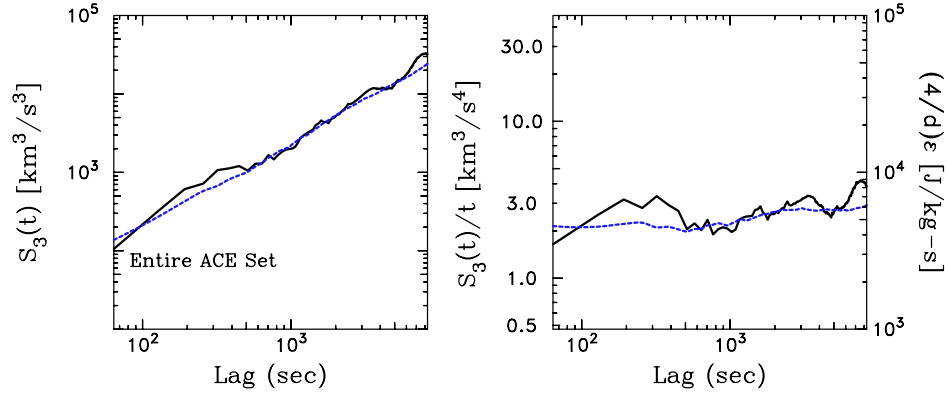


Figure 6.2: (left) Plot of hydrodynamic (dashed blue) and isotropic MHD (solid black) third-moments for 7 years of data from 1998 through 2004. (right) Plot of third-moments divided by time lag τ . Figure reproduced from MacBride et al. (2005).

which may be more applicable for the third-moment expressions, requires more data than is available. Simpler, less rigorous, tests aimed at removing transients involve the comparison of average quantities over multiple subsets of the data interval. All of these techniques provide a method for ensuring the homogeneity of selected data intervals. In our analyses, presented in Chapters 7–9, we settle for the deliberate removal of discontinuities using event lists.

Figure 6.2 shows a preliminary analysis of 7 years of ACE data from year 1998 through 2004. A stationarity test is performed on the mean of the data and detrending is employed in this analysis. While the analysis produces third-moments which are relatively linear with lag, the authors note that the techniques used in analyzing large volumes of data require improvement.

In Chapter 7, it is demonstrated that the ability to utilize large volumes of data is necessary in order to produce accurate and reproducible results due to the slow convergence of third-order structure function expressions. However, the application of third-moments on large volumes of data presents several complications which will be further addressed in the next section.

6.2 MacBride et al. 2008

The analysis of MacBride et al. (2008) builds on the analysis presented in the previous section and forms the basis for our three analyses presented in Chapters 7–9. This study both provides a more in depth analysis of third-order structure functions in the solar wind by improving on the application to large volumes of data and introducing the anisotropic hybrid formalism described in Section 5.3. The MacBride et al. (2008) analysis is an extensive study, touching on many aspects, ranging from the application of third-moments to large volumes of single spacecraft data to the structure of turbulence in fast and slow wind streams and the evolution over the course of the solar cycle. Here, we present the basic analysis technique and findings of MacBride et al. (2008) as they pertain to the analyses presented in this thesis.

The analysis techniques of MacBride et al. (2008) form the basis of the analyses to come, and thus we describe it in detail here. MacBride et al. (2008) use 7 yrs of ACE data ranging

from 1998 to 2005. The data is divided into consecutive subintervals of equal length, in the case of this analysis they use 48 hr intervals. For each of the subintervals, estimates of the various third-moments (i.e. hydrodynamic, isotropic, hybrid) are computed. The ensemble average involved in the third-moment expressions is taken to be the average over all of the subintervals.

Each subinterval has a different average velocity V_{SW} and, therefore, equivalent time lags τ are not comparable between different subintervals unless the average velocities happen to exactly match. To get around this, MacBride et al. (2008) employs an interpolation method to scale each third-moment estimate to a constant average velocity. For ACE plasma data, τ is always an integer multiple of 64 s. Therefore, for each subinterval of data, third-moment estimates at the actual spatial lags $V_{SW}\tau$ (whatever V_{SW} is for that interval), are interpolated onto a set of 113 discrete, fixed spatial lags. The discrete spatial lags are defined by assuming the ACE cadence of 64 s and a 400 km/s wind speed: $400 \text{ km/s} \times 64n \text{ s} = 25,600n \text{ km}$, where $1 < n < 113$. Using this interpolation method, MacBride et al. (2008) averages many third-moment estimates at the same spatial lag, although each estimate is from solar wind with different wind speeds.

Once ensemble averages are performed, cascade rates are computed using Eq. (5.10), (5.17), or (5.34) and (5.35) from Chapter 5. As we mention in Chapter 5, the MacBride et al. (2008) analysis accumulates third-moments in the out/in fashion instead of $+/-$. MacBride et al. (2008) compute uncertainties associated with the third-moment cascade rates simply based on the statistical spread of third-moments divided by lag. A more refined error analysis is presented in the next chapter.

Figure 6.3 shows the results of the analysis considering all of the data from 1998 to 2005. The MacBride et al. (2008) analysis does not attempt to remove the transient structures described in Chapter 3. Detrending and stationarity testing also are not employed in this analysis, although they were experimented with and rejected. Blue lines in the figure represent outward propagation quantities, red lines represent inward propagation quantities, solid black lines represent total out+in quantities, and the black dashed line represents the hydrodynamic version. The top row of panels show the second-moment (left) of velocity and magnetic fluctuations (red and blue lines) and the velocity fluctuations alone (dashed line). These quantities can be used to compute the turbulent power spectrum, the MHD versions of which are plotted in the top right panel. The total power in outward and inward propagating, magnetic and velocity fluctuations follows a power law form of $k^{-1.6 \pm 0.15}$, which is less than 0.5σ from the Kolomogorov prediction for the hydrodynamic spectral form (see Section 4.3). Using the Kolmogorov prediction, an energy cascade rate of $5.5 \times 10^4 \text{ J/kg-s}$ is obtained. MacBride et al. (2008) note the heating rate obtained from the power spectra is too large to match heating observations.

The bottom 4 rows of Figure 6.3 plot the third-moments (left) and third-moments divided by lag (right), which is proportional to the energy cascade rate. The second row of panels corresponds to the isotropic expression seen in Eq. (5.17). The third row corresponds to the perpendicular (2D) expression seen in Eq. (5.34) and the fourth row corresponds to the parallel (1D) expression seen in Eq. (5.35). The fifth row shows the total parallel+perpendicular third-moments derived from Eq. (5.28). Each of the total third-moment expressions (solid black lines) follow an approximately linear trend with lag as is expected by the theory. Energy cascade rates computed from each of the third-moments are reproduced in Table 6.1. Cascade rates computed from the third-moments are more reasonable than the power spectra estimate, which is expected since the third-moment expressions do not make assumptions

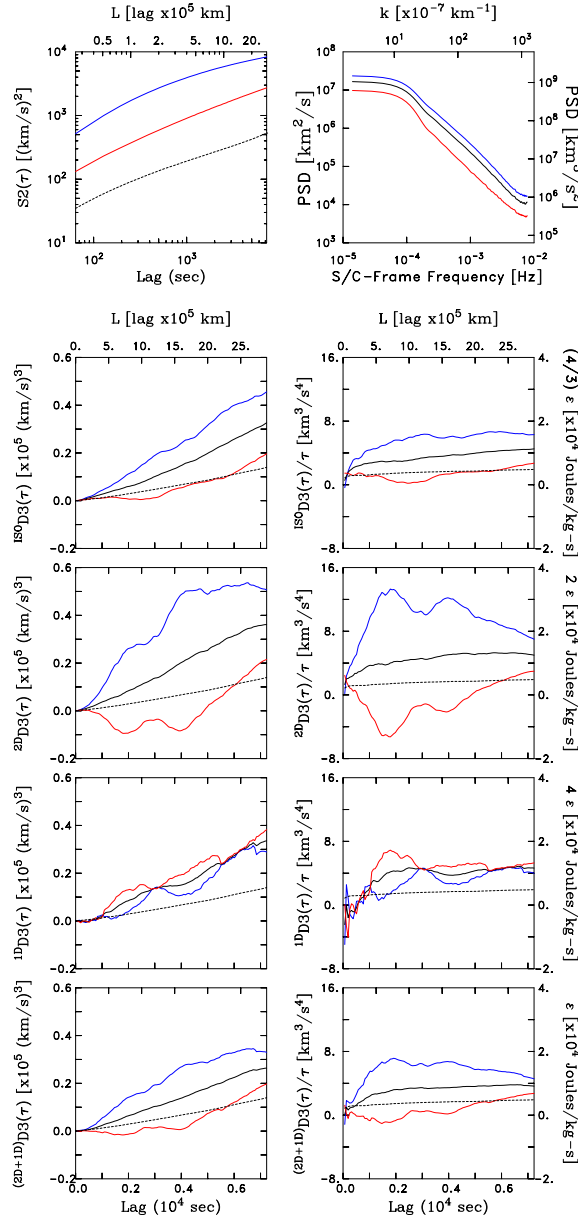


Figure 6.3: Third-moment analysis of ACE data from 1998 to 2005 using 2 day subintervals. (top left) Plot of second order structure functions for outward propagating MHD fluctuations (blue), inward propagating MHD fluctuations (red), and hydrodynamic fluctuations (dashed black). (top right) Power spectra computed from the second-order structure functions for the inward and outward propagating power (same color scheme) and the total magnetic and velocity fluctuation power (solid black). The bottom four rows show third-moment functions for the various turbulence geometries (left) and the third-moments divided by τ , which is proportional to ϵ (right). The color scheme is the same as the top panels. The second row shows the isotropic MHD expression. The third row shows the perpendicular component of the hybrid geometry expression. The fourth row shows the parallel component of the hybrid geometry expression. The fifth row shows the total hybrid geometry. Note the approximately linear scaling of the total out+in cascade rates as a function of lag and the approximately constant cascade rates over the scales analyzed. Figure reproduced from MacBride et al. (2008).

Table 6.1: Computed energy cascade rates for all D_3 in Figure 6.3. Table reproduced from MacBride et al. (2008).

Geometry	$\epsilon \pm \sigma_\epsilon$ (Stand. Dev.) [$\times 10^3$ Joules/kg-s]			
	MHD Outward	MHD Total	MHD Inward	Hydrodynamic
ISO	$10.50 \pm 0.22(2.39)$	$6.50 \pm 0.14(1.45)$	$2.50 \pm 0.12(1.26)$	$4.96 \pm 0.07(0.76)$
2D	$12.20 \pm 0.29(3.12)$	$5.62 \pm 0.10(1.08)$	$-0.96 \pm 0.27(2.86)$	$4.96 \pm 0.07(0.76)$
1D	$1.81 \pm 0.10(1.04)$	$2.29 \pm 0.09(0.98)$	$2.77 \pm 0.12(1.24)$	$4.96 \pm 0.07(0.76)$
2D+1D	$14.00 \pm 0.33(3.51)$	$7.91 \pm 0.19(2.01)$	$1.81 \pm 0.26(2.72)$	$4.96 \pm 0.07(0.76)$

on the underlying dynamics of the turbulence.

Aside from simply demonstrating the application of third-moments to large volumes of solar wind data, MacBride et al. (2008) also perform several studies examining the evolution and structure of the solar wind. In one study, the structure of the turbulence in fast and slow wind streams is examined. MacBride et al. (2008) take fast wind streams to be intervals where the average velocity is greater than 500 km/s and slow wind streams to be intervals where the average velocity is less than 400 km/s. This convention follows from the analysis of Dasso et al. (2005). Using the above outlined analysis techniques, fast and slow wind intervals are separately analyzed.

Figure 6.4 summarizes the results of these analyses. The left panel plots total cascade rates for slow wind intervals, fast wind intervals, and all data using the isotropic MHD (green), hybrid MHD (solid black), and hydrodynamic (dashed black) formalisms. The parallel and perpendicular components of the hybrid formalism are plotted in blue and red respectively. The results show greater cascade rates in fast wind intervals, which is consistent with the greater proton heating rates with increasing V_{SW} expected by Eq. (3.25) (Vasquez et al., 2007). The results also show that the energy cascade in slow winds is nearly isotropic, while the cascade in fast winds is primarily in the perpendicular direction. This indicates that the small-scale inertial range wave vectors will become increasingly oriented in the perpendicular direction (2D turbulence) as the turbulence evolves. This is in keeping with the predicted dominance of the perpendicular cascade by many authors, mentioned in Section 4.5 and provides evidence for the evolution of the turbulence at 1 AU from the field aligned wave vectors observed by Dasso et al. (2005) toward the expected 2D perpendicular geometry.

The right panel of Figure 6.4 attempts to further illuminate the anisotropy present in fast and slow winds. The cascade rates shown in the plot are computed from the parallel and perpendicular components of the hybrid formalism using intervals further subset based on the direction of the mean magnetic field. Intervals are divided such that only intervals where the mean magnetic field is approximately radial or approximately perpendicular to the radial direction are analyzed. MacBride et al. (2008) take a radial field to be when $0^\circ < \Theta_{BR} < 25^\circ$ or $155^\circ < \Theta_{BR} < 180^\circ$, which provides an observed lag only in the parallel direction. The perpendicular field is taken to be when $65^\circ < \Theta_{BR} < 115^\circ$, which provides an observed lag only oriented in the perpendicular direction. Results are consistent with those in the left panel

In another study, the evolution of the turbulent cascade over the course of the solar cycle

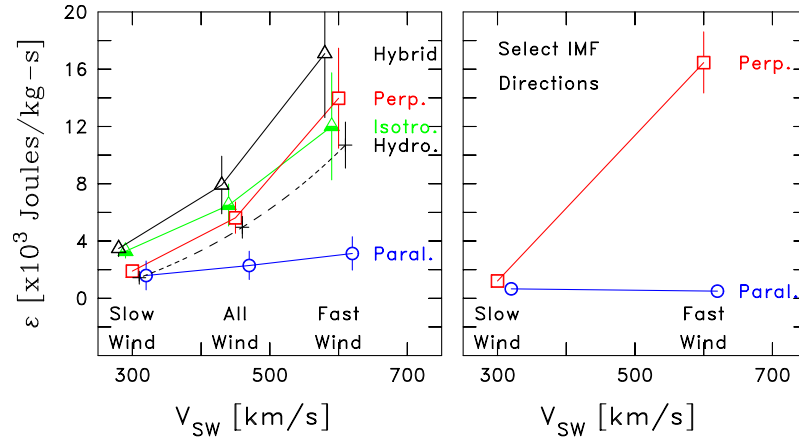


Figure 6.4: (left) Summary of total energy cascade rates for slow wind data ($V_{SW} < 400 \text{ km/s}$), fast wind data ($V_{SW} > 500 \text{ km/s}$), and all data. The black solid line gives cascade rates based on the hybrid MHD formalism, the green line uses the isotropic MHD formalism, and the dashed black line uses the hydrodynamic expression. The red line shows perpendicular component of the hybrid cascade and the blue line shows the parallel component of the hybrid cascade. (right) Plot of cascade rates for slow and fast wind streams, where the mean magnetic field is either directed radially (blue line) or perpendicular to the radial direction (red line). Note that, in slow winds, parallel and perpendicular cascade rates tend to be approximately equal, while in fast winds, the perpendicular cascade tends to dominate. Fast wind streams also appear to have larger energy cascade rates on average. Figure reproduced from MacBride et al. (2008).

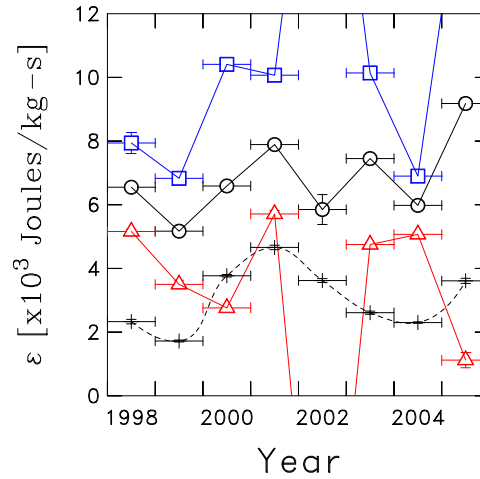


Figure 6.5: Plot of cascade rates separately computed for each year of ACE data from 1998 to 2005 using the isotropic third-moment. The color scheme is the same as Figure 6.3. Notice the approximately constant total cascade rate across all years indicating the turbulent energy cascade is unaffected by the solar cycle. However, considerable variability is present in the outward/inward components from year to year. Figure reproduced from MacBride et al. (2008).

is examined by separately analyzing each year of ACE data from 1998 through 2005 using the techniques outlined above. Figure 6.5 summarizes the computed cascade rates using the isotropic MHD and hydrodynamic expression. The color scheme is the same as Figure 6.3. The year 1998 occurs at the beginning of a rise into solar maximum, while 2005 occurs near the end of the fall into the next solar minimum. While the individual outward and inward (blue and red) cascade rates show considerable variability, the total cascade rate (solid black) remains relatively constant over the course of the solar cycle. This indicates that turbulent cascade rates can provide a consistent heating source for the solar wind. In 2002 and 2005, the inward and outward cascades are considerably imbalanced compared to other years, which remains unexplained. The authors note that the cascade of outward propagating energy is consistently the dominant component. Hydrodynamic values (dashed black), showing the contribution due to velocity fluctuations alone, are also plotted for reference.

Chapter 7

Advanced Heating Test

The analyses of MacBride et al. (2005) and MacBride et al. (2008) described in Chapter 6 provide important first steps in applying third-moment theory to solar wind turbulence. Both analyses show that third-moment expressions follow the linear scaling with lag indicative of a turbulent energy cascade in the solar wind and that ϵ computed from these expressions are roughly on the order of expected heating rates at 1 AU. Neither analysis demonstrates the degree to which computed ϵ compare to local heating rates in the solar wind.

In Stawarz et al. (2009), we build on the analysis of MacBride et al. (2008) to perform two main tasks: 1) we implement improved error analysis techniques to examine the convergence of third-moment estimates of ϵ within the solar wind and 2) quantitatively compare ϵ computed via third-moment expressions to proton heating rates inferred from the radial temperature gradient of the solar wind (see Section 3.7).

The following basic analysis technique is used in this study. We first access a large volume of merged magnetic field and thermal proton data from the ACE spacecraft. This is the same data used by MacBride et al. (2008), but extended to include more recent years. We use 10 years of ACE data from day 23 of 1998 through day 15 of 2008 encompassing both solar maximum and solar minimum behavior. Second, we divide the large volume of data into subsets that are comparable in duration to a correlation length for interplanetary turbulence at 1 AU. For the convergence analysis, we analyze both 12 hr subsets and the 48 hr subsets used by MacBride et al. (2008). Based on the results of the convergence analysis, we use only the 12 hr subsets in the subsequent heating rate analysis. Third, for each subset we compute estimates of the various structure functions described in Chapter 5, as well as averages of $V_{SW}T_P$ for use in the application of Eq. (3.25). As the length of the subsets are comparable to a correlation length, each subset provides a statistically independent sample of the underlying ensemble which is critical to a proper uncertainty analysis. All quantities that derive from a single subset are considered to be without intrinsic uncertainty as measurement uncertainties are small when compared with the statistical spread in the observations. Fourth, we average over many subsets and apply traditional uncertainty analyses. Last, in the case of structure functions, we perform an uncertainty-weighted average over lags within the inertial range to compute an average energy cascade rate.

7.1 Convergence of Third-Order Structure Functions

In order to demonstrate the rate of convergence of third-order structure functions, we perform the following analysis. We apply the formalism for the hybrid cascade shown in Section 5.3

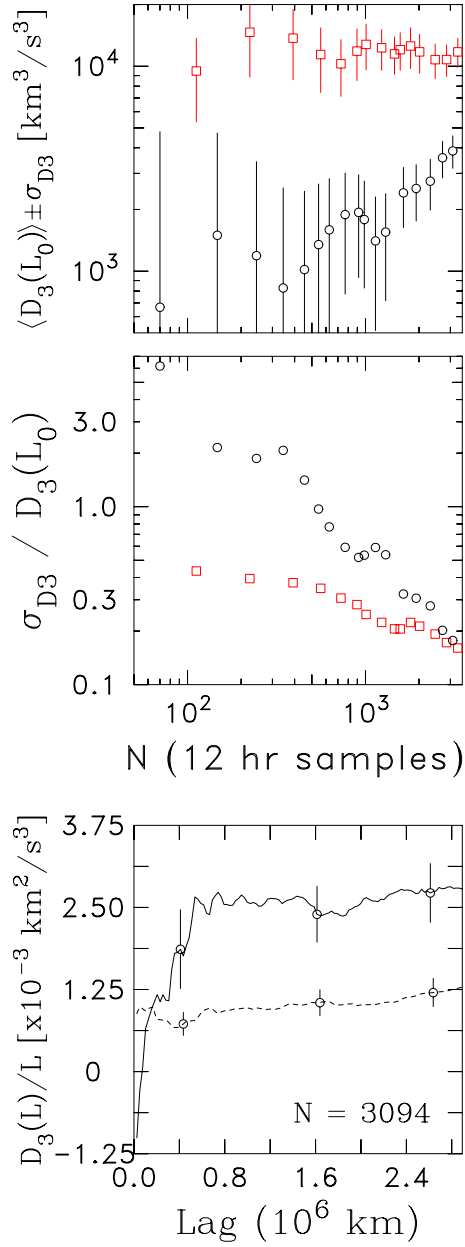


Figure 7.1: (top) Mean $\langle D_3(L_0) \rangle$ and uncertainty σ_{D_3} from hybrid MHD analysis at $L_0 = 1.6 \times 10^6 \text{ km}$ ($\tau = 4032 \text{ s}$). Red squares denote all data. Black circles denote removal of transients. (middle) Relative uncertainty in same. (bottom) Function $D_3(L)/L$ for hybrid MHD (solid) and hydrodynamic (dashed) calculations with example uncertainties for transient removal with best convergence ($N = 3094$). Figure reproduced from Stawarz et al. (2009).

to several years of ACE data starting with day 360 of 1999. We use 12 hr and 48 hr samples to compute estimates of the third-moments $D_{3,\perp}^{\pm}(\tau)$ and $D_{3,\parallel}^{\pm}(\tau)$ from Eq. (5.34) and (5.35).

Estimates from different samples are averaged together using the interpolation method described in Chapter 6. Uncertainties associated with these averages are computed in the usual manner (Bevington, 1969):

$$\sigma_X^2 \equiv (1/N) \left\{ \langle X^2 \rangle - \langle X \rangle^2 \right\} \quad (7.1)$$

where $\langle \dots \rangle$ denotes an unweighted average over 12 or 48 hr intervals, σ_X is the error-of-the-mean for any quantity X , and X is any quantity averaged over many intervals. The estimate of σ_X permit us to determine the statistical significance of the measured average of $V_{SW}T_P$ or any of the third-moment functions. The uncertainty analysis for the latter is computed as a function of lag L .

As an example, we show results for the total hybrid structure function D_3 defined in Eq. (5.30). Figure 7.1 (top) demonstrates that D_3 requires a considerable amount of data to achieve statistical convergence. Figure 7.1 plots the mean and estimated uncertainty $\langle D_3 \rangle$ and σ_{D_3} for the single value of lag $L = L_0 = 1.6 \times 10^6$ km for two separate analyses of the ACE data. Both analyses begin at the start of year 2000. In the first analysis (red) all data is used. In the second analysis (black), we remove transient data. This is done by accessing the ACE shock list maintained by the ACE Science Center and excluding all 12 hr analysis intervals that fall anywhere on or within the interval starting 12 hrs upstream of the shock and ending 36 hrs downstream of the shock. This removes considerable amounts of data during solar maximum, but guarantees removal of foreshock, shock, and driver gas. At each step in the analysis, an additional three solar rotations of data is incorporated. The plot shows the computed convergence in the sense of “diminishment of error” of the third-moment calculation for ϵL at $L_0 = 1.6 \times 10^6$ km (or, 0.01 AU corresponding to a time lag of $\tau = 4032$ s or ~ 67 min and a mean wind speed $V = 400$ km/s) using the hybrid geometry analysis plotted vs. the number of 12 hr samples used in the average. This is a lag within the expected inertial range. Because of transient removal, the black curve always uses fewer 12 hr samples. Clearly, inclusion of transients results in a significantly higher computed D_3 and associated cascade rate ϵ than when transients are removed. Since transients contain shocks, which are strong compressive signatures far outside the realm of this theory; and driver gas often contains magnetic clouds with strong rotations of the mean IMF, which yield significant signatures in D_3 , the exclusion of transients gives a better estimation of the heating rate of undisturbed solar wind. Also, the Vasquez et al. (2007) analysis, which leads to Eq. (3.25), does not include transients. To what extent the analysis including transients is useful or offers a meaningful assessment of heating rates under these conditions is unclear at the present time.

Figure 7.1 (middle) plots the relative uncertainty for the same value of L . It is curious that the analysis including transient data converges more rapidly than the analysis omitting transients, but nevertheless the latter gives a clear indication of how much data is required to obtain convergence in this analysis. The general rate of convergence is consistent with Podesta et al. (2009) which finds that for both 64 s resolution solar wind data and 40 ms resolution wind tunnel data, approximately one million data points are required to reduce the relative uncertainty to below 30%.

Figure 7.1 (bottom) plots $D_3(L)/L$ as a function of lag where D_3 is again summed over \parallel , \perp and out/in components so as to obtain the form of D_3 relevant to the total energy cascade.

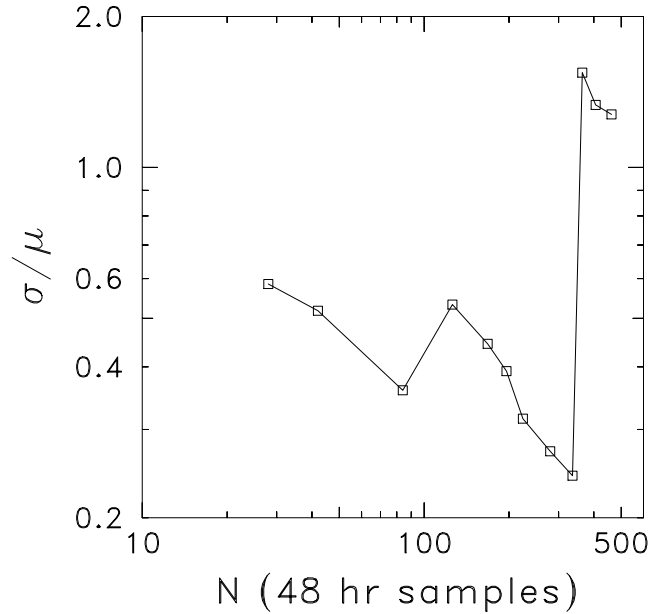


Figure 7.2: Reanalysis of Figure 7.1 (middle) including transient data using 48 hr subintervals. Figure reproduced from Stawarz et al. (2009).

Statistical uncertainties are plotted for several example lags. The function is approximately constant over most of the range of lag values.

Because of issues relating to mean field convergence (Matthaeus and Goldstein, 1982b), we have experimented with longer intermediate subintervals than the 12 hr subsets described above. We do not mean to claim that this together with a stationarity test will prove unsuccessful, but we offer the following demonstration as evidence of what can go wrong with analyses using long intermediate time scales. We recompute the summed hybrid structure function $D_3(L_0)$ as demonstrated in Figure 7.1 using 48 hr subintervals and examine the same $L_0 = 1.6 \times 10^6$ km lag. Figure 7.2 shows the result of this effort. The analysis is extremely vulnerable to transient observations that can reset the convergence of the computed third-moment. While the 12 hr analysis changes when transients are included or excluded, both analyses show convergence as additional data is added. This is not the case with the 48 hr analysis.

7.2 Energy Cascade vs. Heating Rates

Following the analysis above, we take 12 hrs to be our intermediate time scale over which individual estimates of the structure functions defined in Chapter 5 are computed. We compute the mean value of $V_{SW}T_P$ for each 12 hr subset and group the samples into seven bins based on this value. Uncertainties are again computed as above. Eq. (3.25) is evaluated from the mean and standard deviation of 12 hr values for $V_{SW}T_P$ within each bin to produce a mean value of $\langle \epsilon_{\text{heat}} \rangle$ and associated error-of-the-mean according to Eq. (7.1). Figure 7.3 plots $\langle \epsilon_{\text{heat}} \rangle$ as accumulated into the seven overlapping bins of $V_{SW}T_P$. Horizontal bars denote the standard deviation for values of $\langle V_{SW}T_P \rangle$ within each bin. Vertical bars denote errors-of-the-means for computed ϵ_{heat} .

We compute third-moment estimates of ϵ using the isotropic and hybrid MHD forms,

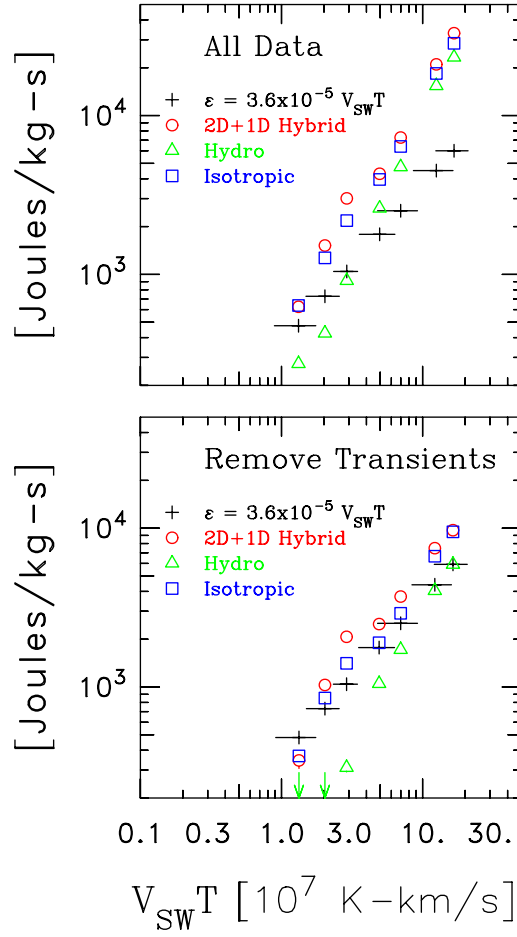


Figure 7.3: Comparison of total energy cascade for hydrodynamic and multi-dimensional MHD cascades vs. expected heating rates for protons as computed by Vasquez et al. (2007). (top) Uses all ACE data during the 10yr period. (bottom) Removes transient events to use remaining data subset of 10yr period. Hydrodynamic results for first two bins are off scale. Figure reproduced from Stawarz et al. (2009).

as well as, the hydrodynamic expression as described above with one addition: We average over all lags to compute an average value of ϵ within the inertial range. While ϵ is expected to be constant for all inertial range lags, some variability is observed and estimates derived for short lags via the hybrid analysis can be especially poor with large uncertainties. For this reason, we use an uncertainty-weighted average of $D_3(L)/L$ and the associated error-of-the-mean σ_ϵ to compute the mean rate of energy cascade and its associated uncertainty (Bevington, 1969):

$$\epsilon = G \left\{ \sum_L \left\{ [D_3(L)/L] / [\sigma_{D_3(L)}^2/L^2] \right\} \right\} \left\{ \sum_L [1/(\sigma_{D_3(L)}^2/L^2)] \right\}^{-1} \quad (7.2)$$

$$\sigma_\epsilon = \left\{ \sum_L [1/(\sigma_{D_3(L)}^2/L^2)] \right\}^{-1/2} \quad (7.3)$$

where $\sigma_{D_3(L)}^2$ is defined in Eq. (7.1). The constant G is dependent on the geometry and

dynamics so that for isotropic hydrodynamics $G_{HD} = 5/4$, for isotropic MHD $G_{ISO} = 3/4$, for the perpendicular cascade in the hybrid MHD expression $G_{\perp} = 1/2$, and for the parallel cascade in the hybrid MHD expression $G_{\parallel} = 1/4$. These constants can be extracted simply from the expressions in Chapter 5. We apply this formalism to the isotropic and hybrid MHD and hydrodynamic expressions and plot the results in Figure 7.3.

Figure 7.3 (top) shows a strong divergence between the Vasquez et al. (2007) and third-moment formalisms. While differences between computed cascade rates and the energy required to heat thermal protons is a factor of two for small values of $V_{SW}T_P$, it grows to $8\times$ for larger values. This is too much discrepancy to be acceptable, and we must consider the role of transients in the calculation.

Figure 7.3 (bottom) plots the recomputed values of ϵ derived from the Vasquez et al. (2007) analysis and the third-moment formalism as described above with shocks and associated driver gas removed. The results show a consistent excess of energy within the MHD cascade as compared to the proton heating rate ϵ_{heat} . The only exception to this is the lowest $V_{SW}T_P$ bin where both the isotropic and hybrid MHD expressions yield cascade rates lower than the Vasquez et al. (2007) prediction. Although the excess is small (factor of $\sim 50\%$), it is statistically significant at better than the $5\sigma_{\epsilon}$ level.

In both analyses shown in Figure 7.3, we see that the isotropic and hybrid MHD forms give similar total cascade rates (MacBride et al., 2008), but these values differ significantly and systematically from the hydrodynamic expression.

7.3 Heating Discussion

Figure 7.4 (top) shows the ratio of $\epsilon/\epsilon_{\text{heat}}$ where ϵ is computed from the various hydrodynamic and MHD structure function expressions. Three conclusions are immediately apparent: First, the computed hydrodynamic cascade systematically underestimates the MHD cascade at low values of $V_{SW}T_P$ and approaches the MHD predictions asymptotically for high values. Second, the MHD cascade is less than ϵ_{heat} at the lowest values of $V_{SW}T_P$. Third, the MHD cascade is systematically greater than ϵ_{heat} at all but the lowest values of $V_{SW}T_P$. Table 7.1 reproduces the values shown in Figure 7.4 (top).

We return now to the analysis of Vasquez et al. (2007). Two issues are addressed there which we must now consider in light of the above results. First, the gradients of T_P were measured in bins of V_{SW} that included both hot and cold plasma observations. The colder winds may be characterized by less heating than average. In fact, Freeman and Lopez (1985) show that $\sim 10\%$ of Helios data are slow, very cold winds that can be explained by an almost adiabatic expansion of the plasma. Therefore, where $V_{SW}T_P$ is small in Figure 7.4 (top), Eq. (3.25) could overestimate the true proton heating. This suggests that the heating rate as measured by the MHD cascade rate may be correct.

Second, the radial gradients of T_P and the resulting Eq. (3.25) of this paper are based only on the radial component of T_P as measured by ACE. Vasquez et al. (2007) shows that radial gradients of the projections of the solar wind thermal anisotropy onto the radial component (allowing for both changing anisotropy and rotation of the distribution with the IMF spiral) leads to significant differences between the radial gradient of the radial component of the temperature and the radial gradient of the average temperature. Taking this into consideration, Vasquez et al. (2007) determine that Eq. (3.25) which defines ϵ_{heat} underestimates the actual proton heating at 1 AU by a factor of 22%. We therefore consider estimates of ϵ_{heat} in Figures 7.3 and 7.4 (top) that are increased by 22%. This increase in

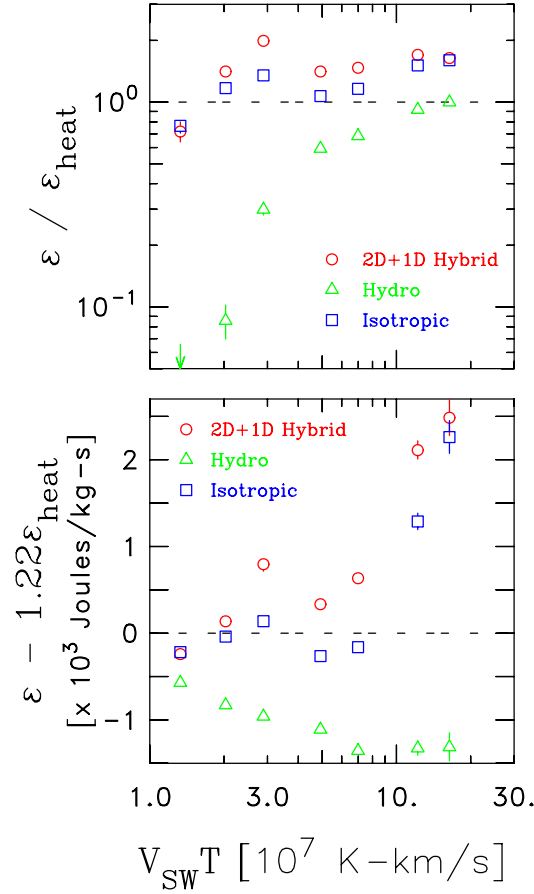


Figure 7.4: (top) Ratio of ϵ from the structure function method for hydrodynamics and MHD to ϵ_{heat} from the Vasquez et al. (2007) analysis of thermal protons. Analysis removes transients. Hydrodynamic result for first bin is off scale. (bottom) Difference of ϵ and ϵ_{heat} with transients removed using a worst-case factor of 1.22. Result predicts amount of energy cascade available for heating heavy ions and electrons. Figure reproduced from Stawarz et al. (2009).

Table 7.1: Computed $\epsilon/\epsilon_{\text{heat}}$ for ACE data with transient removal. Table reproduced from Stawarz et al. (2009).

$V_{SW}T_P$ [$\times 10^7$ (km/s)K]	$\epsilon/\epsilon_{\text{heat}}$		
	Hydrodynamics	Isotropic MHD	Hybrid MHD
1.3 ± 0.4	-0.0013 ± 0.015	0.77 ± 0.06	0.72 ± 0.08
2.0 ± 0.5	0.09 ± 0.02	1.17 ± 0.06	1.41 ± 0.08
2.9 ± 0.6	0.30 ± 0.02	1.35 ± 0.06	1.99 ± 0.08
4.9 ± 1.4	0.59 ± 0.01	1.07 ± 0.03	1.41 ± 0.03
7.0 ± 2.2	0.68 ± 0.01	1.16 ± 0.02	1.47 ± 0.02
12.2 ± 3.8	0.92 ± 0.02	1.51 ± 0.02	1.70 ± 0.03
16.4 ± 4.3	1.00 ± 0.03	1.60 ± 0.03	1.64 ± 0.04

Table 7.2: Computed $\epsilon - 1.22\epsilon_{\text{heat}}$ for ACE data with transient removal. Table reproduced from Stawarz et al. (2009).

$V_{SW}T_P$ [$\times 10^7$ (km/s)K]	$\epsilon - 1.22\epsilon_{\text{heat}}$ [Joules/kg-s]		
	Hydrodynamics	Isotropic MHD	Hybrid MHD
1.3 ± 0.4	$-570. \pm 9.$	$-218. \pm 29.$	$-241. \pm 38.$
2.0 ± 0.5	$-829. \pm 13.$	$-39. \pm 46.$	$137. \pm 48.$
2.9 ± 0.6	$-960. \pm 20.$	$138. \pm 63.$	$795. \pm 80.$
4.9 ± 1.4	$-1110. \pm 27.$	$-264. \pm 46.$	$334. \pm 57.$
7.0 ± 2.2	$-1355. \pm 35.$	$-161. \pm 46.$	$634. \pm 55.$
12.2 ± 3.8	$-1326. \pm 80.$	$1288. \pm 94.$	$2110. \pm 103.$
16.4 ± 4.3	$-1313 \pm 158.$	$2261. \pm 188.$	$2484. \pm 205.$

ϵ_{heat} is not sufficient to equate ϵ_{heat} with the rates obtained by the third-moment analyses. The measured cascade rates using D_3 for MHD still exceed the proton heating rates for all but the lowest values of $V_{SW}T_P$.

The best case argument for where the excess energy goes is made in the limit of high $V_{SW}T_P$. Winds of all speeds contribute here whenever they possess high $T_P \sim 2 - 3 \times 10^5$ K. Moreover, nearly all high-speed streams contribute to the upper bins of $V_{SW}T_P$ because they nearly always have both large V_{SW} and large T_P . The computed excess in the energy cascade in the highest two $V_{SW}T_P$ bins is 50 – 70%. Increasing ϵ_{heat} by 22% reduces the excess to 25 – 50%. While heavy ions may absorb some of this energy, there are no spectral signatures associated with heavy ion resonances. Also, Reisenfeld et al. (2001) argue that in situ heating of alphas comes from the deceleration of their differential streaming relative to protons. This is strongest in high-speed winds, which are hot winds, leaving open the possibility that some significant alpha heating via the cascade is active for intermediate values of $V_{SW}T_P$. We contend that most of the computed excess in the energy cascade goes to heating electrons. Leamon et al. (1999) argue that damping of waves at the Landau resonance is possible in many cases at scales comparable to the dissipation scale where the magnetic spectrum breaks (0.1 to 0.5 Hz). In their model, electron heating is accomplished by obliquely propagating proton cyclotron waves and approximately 40% of the cascading energy heats electrons (or 2/3 of the energy heating protons). Leamon et al. (1998) and Hamilton et al. (2008) argue that spectral characteristics in the dissipation range support the claim that 25 – 40% of the energy cascade goes into dissipation processes other than proton cyclotron resonance and electron heating either by cyclotron, transit time, Landau damping or current sheet formation. This places an upper bound on electron heating at 1/3 to 2/3 the proton heating rate which is consistent with our conclusions based on the excess cascade energy when compared to the observed local heating rate of protons. Gary et al. (2008) and Saito et al. (2008) argue that a cascade of whistler mode energy can be established at scales much smaller than the proton inertial length. This cascade is not strictly energy-conserving since the modes are Landau resonant with thermal electrons, but it does represent transport of magnetic energy to smaller scales (and perpendicular wave vectors) in association with electron heating. It is possible that the remainder of the energy cascade that is not used to heat thermal protons is thereby used to heat electrons.

In order to quantitatively address the heating of heavy ions and electrons, we compute

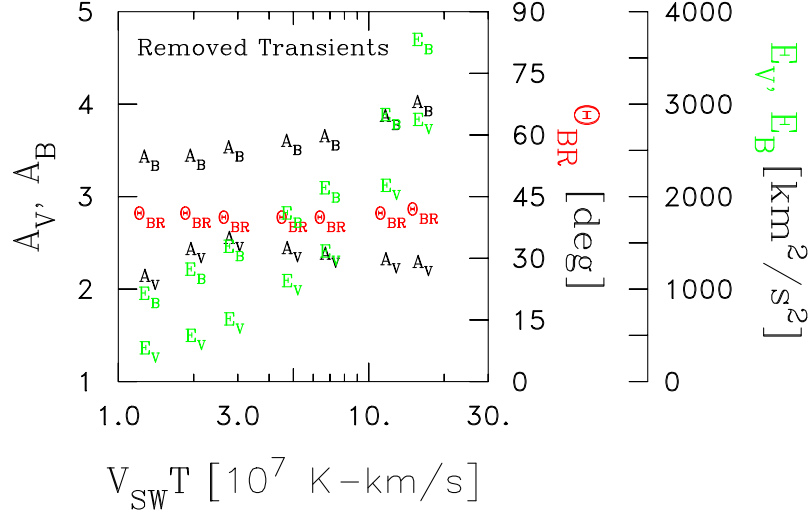


Figure 7.5: Anisotropy of velocity A_V and magnetic A_B fluctuations, angle between mean magnetic field and radial direction Θ_{BR} , velocity fluctuation energy E_V and magnetic fluctuation energy E_B . All values are computed as means of r.m.s. values for 12 hr intervals. Uncertainties are generally smaller than symbols used in plotting. Figure reproduced from Stawarz et al. (2009).

the excess energy in the cascade relative to the rate of proton heating derived from the radial gradient of proton temperatures. Figure 7.4(bottom) adopts the factor of 1.22 on ϵ_{heat} and computes the remaining energy that can be extracted from the cascade. As we have already seen, the hydrodynamic expression produces too little energy in the cascade to explain the heating of thermal protons. The lowest bin also contains too little energy cascade for the MHD expressions, but as discussed above this is probably because the expected proton heating is an overestimate for this bin. At intermediate values of $V_{SW}T_P$, we find, on average, there is an excess in the MHD energy cascade (both isotropic and hybrid) of ~ 500 Joules/kg-s that is available for heating of heavy ions and electrons. For the largest values of $V_{SW}T_P$, the energy excess is ~ 2000 Joules/kg-s. Table 7.2 lists the values plotted in Figure 7.4(bottom).

In an effort to understand why the hydrodynamic expression possesses the asymptotic behavior seen in Figure 7.4, we compute several r.m.s. averages of the data: The kinetic and magnetic energy (E_V and E_B , respectively) and the velocity and magnetic anisotropy relative to the radial (flow) direction (A_V and A_B , respectively) as defined by the fluctuation energy in the previously defined T and N components summed and divided by the energy in the R component. The reader will recall that the hydrodynamic expression uses the R component only. We also average the angle between the mean magnetic field and the radial direction Θ_{BR} . Figure 7.5 shows the results of these averages binned by $V_{SW}T_P$. The bulk anisotropy of the velocity fluctuations is $2.1 < A_V < 2.6$ where $A_V = 2$ denotes isotropy, so the observed behavior for ϵ^{HD} is unaffected by a hypothetical anisotropy in the velocity fluctuations. The bulk anisotropy of the magnetic fluctuations is larger, in apparent support of the hybrid geometry approximation and adding complication to the isotropic analysis. Both the kinetic energy E_V and the magnetic energy E_B rise consistently with the difference being approximately constant. The ratio E_V/E_B decreases slightly with increasing $V_{SW}T_P$ in mild support of a convergence of $\epsilon^{\text{MHD}}/\epsilon^{\text{HD}}$, but not to the degree seen in Figure 7.4(top).

This does not support the result shown in Figure 7.4 (bottom) where the difference between computed values of ϵ^{MHD} and ϵ^{HD} increases with $V_{\text{SW}}T_P$. Likewise, the average value of Θ_{BR} is virtually constant at $\sim 41^\circ$ with a standard deviation of $\sim 15^\circ$ for each bin. This indicates that the product $V_{\text{SW}}T_P$ is dominated by the factor of ~ 10 variation of T_P and not the factor of 2 variation of V_{SW} . Each $V_{\text{SW}}T_P$ bin contains both fast and slow winds. There is no support for the claim that rotation of the IMF alters the measured correlations in a manner that might alter the measured ϵ . We can only conclude that there are significant changes in the correlations including phase that occur as $V_{\text{SW}}T_P$ increases, as this is the central idea in the third-moment formalism. Moreover, it points to an important reason why estimates of ϵ based on the power spectra alone seem to fail at 1 AU.

7.3.1 A Small Correction

Over the course of performing the analysis described in Chapter 9, a small error in the selection of 12 hr intervals in the above analysis was uncovered. The error pertains to the selection of intervals with adequate data coverage to effectively perform the third-moment analysis and merely results in the rejection of additional intervals which would otherwise be considered good candidates. Figure 9.7 revises the analysis in the bottom panel of Figure 7.3 as it pertains to the large-scale shear analysis of Chapter 9. The isotropic formalism is shown in blue and proton heating rates are shown in black. The red points pertain to the shear analysis and are not pertinent to this discussion. The isotropic cascade rates shift by an amount greater than 1 error-of-the-mean. In particular, the second and third points from the left, which are above the proton heating rate in Figure 7.3, now lay below ϵ_{heat} . Note, some of this variability is the result of additional selection criteria necessary for the shear analysis and this plot is only referred to for demonstration purposes. We have re-performed the exact analysis present in this chapter, and the results are similar to those in this figure.

Even with this slight modification, the conclusions of this chapter are unaffected. Recall that proton heating rates computed from Eq. (3.25) are expected to overestimate the true heating rate a lower $V_{\text{SW}}T_P$ and the higher $V_{\text{SW}}T_P$ cascade rates in this analysis remain relatively unaffected. While not shown, the conclusions of the hybrid analysis are likewise unchanged.

Chapter 8

High Cross-Helicity

We further build on the analyses of MacBride et al. (2005, 2008) and Stawarz et al. (2009) described in the previous two chapters, whose application and extension of the ideas of Politano and Pouquet (1998a,b) has led to the following results: 1) Demonstration that a scale-independent cascade rate exists within the inertial range of solar wind fluctuations at 1 AU; 2) Energy cascade rates in good agreement with the inferred heating rates of the solar wind; and 3) Energy cascades perpendicular to the mean magnetic field direction in high-speed winds in agreement with simulations that require the asymptotic state of the turbulence to approach a 2D (perpendicular wave vector) geometry.

The Stawarz et al. (2009) study, from the previous chapter, sorts data based on one parameter that should relate to the energy cascade rate: the proton heating rate. Another parameter on which ϵ depends is the cross-helicity, which turbulence theory predicts will “throttle” the rate of energy cascade. In this study (Stawarz et al., 2010), we analyze the dependence of ϵ on cross-helicity in the solar wind and uncover an unusual process in intervals of “high” cross-helicity. This analysis technique is also explored in a less in depth fashion in Smith et al. (2009).

We analyze the same 10 yrs of ACE spacecraft magnetic field and plasma data from the analysis of the previous chapter. This data spans from 1998 through 2007 and we again divide this into 12 hr intervals. The same basic procedure from Chapters 6 and 7 is used for computing third-moment expressions (MacBride et al., 2008; Stawarz et al., 2009).

8.1 Cross-Helicity

The average energy per unit mass in incompressible kinetic and magnetic fluctuations within a given 12 hr interval is:

$$E \equiv \frac{1}{2} \left(\frac{1}{N} \sum_i [(\delta v)^2 + (\delta B)^2] \right) \quad (8.1)$$

$$= \frac{1}{4} \left(\frac{1}{N} \sum_i [(\delta Z^+)^2 + (\delta Z^-)^2] \right) \quad (8.2)$$

where \sum_i represents the sum over N points, one for each 64s within the 12 hr interval. Here, and for the purposes of this chapter, we redefine the magnetic field in Alfvén units $\mathbf{B}^A \equiv \mathbf{B}/\sqrt{\mu_0 \rho}$ and for convenience drop the superscript A . From Eq. 8.1 and 8.2, we identify $\langle (\delta \mathbf{Z}^+)^2 \rangle / 4$ as the energy in fluctuations propagating anti-parallel to the mean magnetic field,

and $\langle(\delta\mathbf{Z}^-)^2\rangle/4$ as the energy in parallel-propagating fluctuations. The difference between the two energies is called the cross-helicity H_C . Within a given interval H_C is the cross-correlation between magnetic and velocity fluctuations. The average cross-helicity within a given interval can be written as:

$$H_C \equiv \frac{1}{N} \sum_i [\delta\mathbf{v} \cdot \delta\mathbf{B}] \quad (8.3)$$

$$= \frac{1}{4} \left(\frac{1}{N} \sum_i [(\delta Z^+)^2 - (\delta Z^-)^2] \right). \quad (8.4)$$

The amount of cross-helicity that can be supported by the turbulence is limited by the energy. Therefore, we can normalize H_C according to energy:

$$\sigma_C \equiv H_C/E \quad (8.5)$$

so that the following relationship holds:

$$-1 \leq \sigma_C \leq +1. \quad (8.6)$$

The normalized cross-helicity σ_C describes the amount of imbalance between the fluctuations propagating in different directions: when $\sigma_C = \pm 1$, fluctuations are completely in one direction, and when $\sigma_C = 0$, they are “balanced” with equal energy content in the two propagation directions. We show in this chapter that the energy cascade rate deduced from the third-moment of the fluctuations, depends on σ_C , as well as, on the total energy in fluctuations. When $|\sigma_C| = 1$ the turbulence has maximum cross-correlation between the two fields and the non-linear terms that constitute the turbulent evolution are zero. It is not unusual for the solar wind to have large $|\sigma_C|$, but the correlation is never perfect and at worst the turbulent cascade is expected to be sluggish as a result. Each 12 hr interval of ACE data is then characterized by a pair of values E and σ_C .

Just as the total rate of energy cascade is written as $\epsilon^T = (\epsilon^+ + \epsilon^-)/2$ (see Eq. (5.13)), the cross-helicity cascade rate is written as:

$$\epsilon^C = (\epsilon^+ - \epsilon^-)/2 \quad (8.7)$$

Furthermore, a normalized cross-helicity rate of cascade is given by $\epsilon^{\sigma_C} = (\epsilon^+ - \epsilon^-)/(\epsilon^+ + \epsilon^-)$.

In the analyses presented in this chapter, we again use $\mathbf{Z}^{out/in}$ instead of \mathbf{Z}^\pm in accordance with the direction of fluctuation propagation. As such, we continue to refer to D_3^{out} , D_3^{in} , ϵ^{out} , and ϵ^{in} as seen in previous chapters. The cascade of cross-helicity is no different. Since the sign of H_C changes with the mean field direction, we risk simple cancellation if we add measurements from toward and away sectors. Therefore, we redefine the cross-helicity as the difference between outward and inward propagating components and the cascade of cross-helicity is given by $\epsilon^C = \frac{1}{2}(\epsilon^{out} - \epsilon^{in})$. The normalized cross-helicity rate of cascade is $\epsilon^{\sigma_C} = (\epsilon^{out} - \epsilon^{in})/(\epsilon^{out} + \epsilon^{in})$. All of this is designed to avoid simple cancellation due to field reversals that would result in $H_C = 0$ even though $|H_C| > 0$ in most instances.

8.2 Isotropic Analysis

Figure 8.1 shows the distribution of fluctuation energy computed by Eq. 8.1 for 12 hr samples using the stated 10 yrs of data. The purpose of this analysis is to determine how ϵ^\pm depends

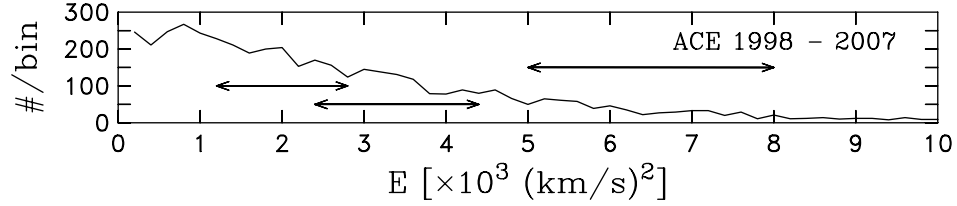


Figure 8.1: Distribution of magnetic and kinetic fluctuation energy for 12 hr samples grouped in $200 \text{ km}^2/\text{s}^2$ bins as defined by Eq. 8.1. There are 4625 samples in the distribution after eliminating shocks and transients. Figure reproduced from Stawarz et al. (2010).

upon E and σ_C in the solar wind. Kolmogorov scaling implies $\epsilon^T \sim E^{3/2}$ (Kolmogorov, 1941a), but the application of this concept to MHD turbulence leads to a dependence upon σ_C that is unknown. We select three energy intervals represented by arrows in the figure and four intervals of cross-helicity. Table 8.1 lists these energy and helicity ranges along with the number of 12 hr samples obtained for each. In this analysis, we use the isotropic MHD formalism described in Section 5.2. The resulting estimates for $D_{3,ISO}^{in/out}$ are shown in Figure 8.2. Note that each curve is to a fair approximation a straight line indicating that the energy cascade rate $\sim D_{3,ISO}^{in/out}/(V_{SW}\tau)$ is constant at all scales. Table 8.1 lists the computed energy cascade rates for each component.

What we see consistently in Figure 8.2 is that the energy cascade rate of the majority outward-propagating component (blue) decreases with increasing σ_C until it becomes negative while the minority inward-propagating component (red) decreases, but remains positive. We see this same behavior in all three energy subsets, but greater values of σ_C must be reached for the more energetic intervals before the reversal is obtained.

Figure 8.3 (top) plots the energy cascade rate for the outward propagating and inward propagating components as well as total energy and cross-helicity cascade rates. Note that as inferred above, the energetically dominant outward-propagating component possesses the greatest energy cascade rate at low values of $|\sigma_C|$, but that the cascade rate decreases and becomes negative at large values of $|\sigma_C|$. This results in a negative rate of energy cascade for the total energy when $|\sigma_C|$ is sufficiently large. As suggested above, ϵ^{in} remains positive. Note: when data is selected without regard for $|\sigma_C|$ the total energy cascade rate for each of the three energy subsets is 824 ± 27 , 2273 ± 36 , and $6099 \pm 102 \text{ J/kg-s}$, respectively, with both outward and inward propagating components showing positive energy cascade.

Table 8.2 lists several quantities derived from Figure 8.2 and Table 8.1. The first is the ratio of the energy cascade rate for outward propagation to energy cascade rate for inward propagation $\epsilon^{out}/\epsilon^{in}$. The second quantity is the cascade rate for the cross-helicity and the third quantity is the normalized cascade rate for the cross-helicity defined above. Figure 8.3 (middle) shows the ratio $\epsilon^{out}/\epsilon^{in}$ as a function of $|\sigma_C|$. At low values of $|\sigma_C|$, the ratio $\epsilon^{out}/\epsilon^{in}$ increases with energy. It appears that for low to intermediate values of $|\sigma_C|$ the ratio $\epsilon^{out}/\epsilon^{in}$ increases with increasing $|\sigma_C|$, but as ϵ^{out} turns negative the ratio turns negative as well. The lowest energy bin fails to show this behavior because the negative cascade regime begins at relatively low values of $|\sigma_C|$. At large $|\sigma_C|$ the value of $|\epsilon^{out}|$ significantly exceeds ϵ^{in} and is the dominant term in the cascade, leading to $|\epsilon^{out}/\epsilon^{in}| > 1$. Figure 8.3 (bottom) plots ϵ^{σ_C} . Omitting one point in the first panel that occurs when $\epsilon^T \simeq 0$ (the denominator in Eq. 8.5) there is a general trend to larger (positive, > 1) cascade rates for the normalized

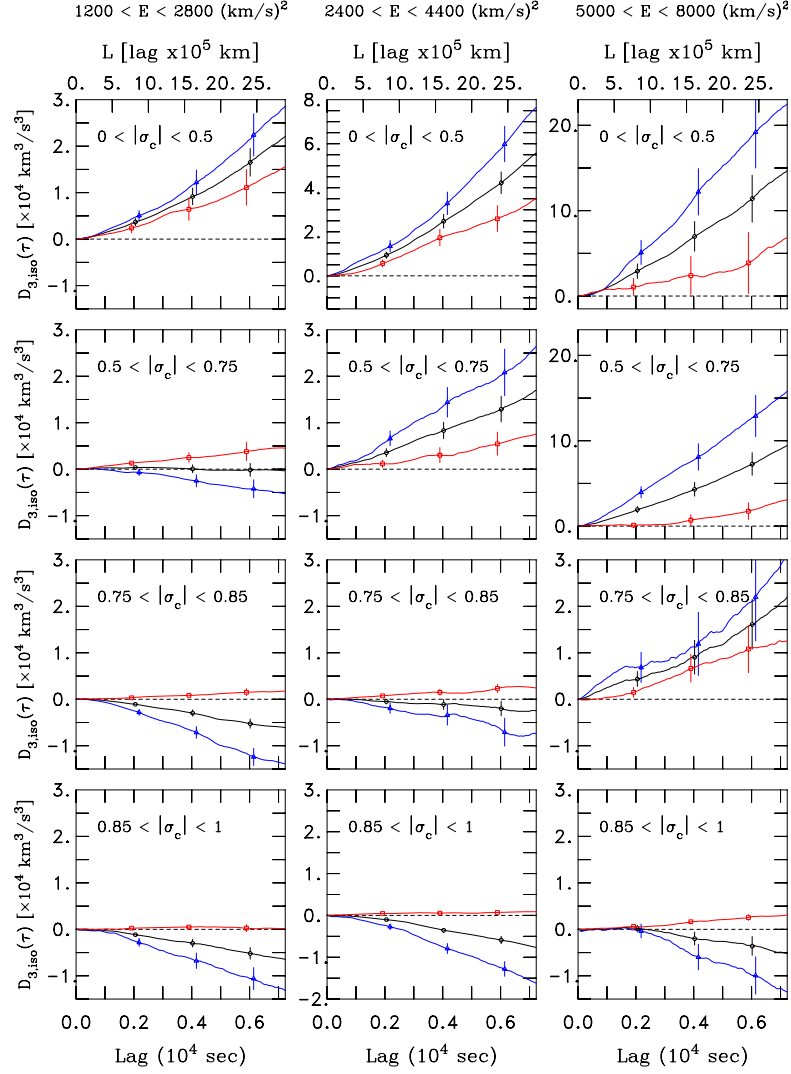


Figure 8.2: Computed values for $D_{3,ISO}$ according to Eq. 5.17 using 12 hr samples and 10 years of data. Vertical columns represent the three energy ranges shown in Figure 8.1. Horizontal rows are four helicity ranges. Blue (red) marked with triangles (squares) denote outward (inward) propagation. Black middle curve marked by circles is $D_{3,ISO}^T$. Sample error bars are shown. See Table 8.1 for details. Figure reproduced from Stawarz et al. (2010).

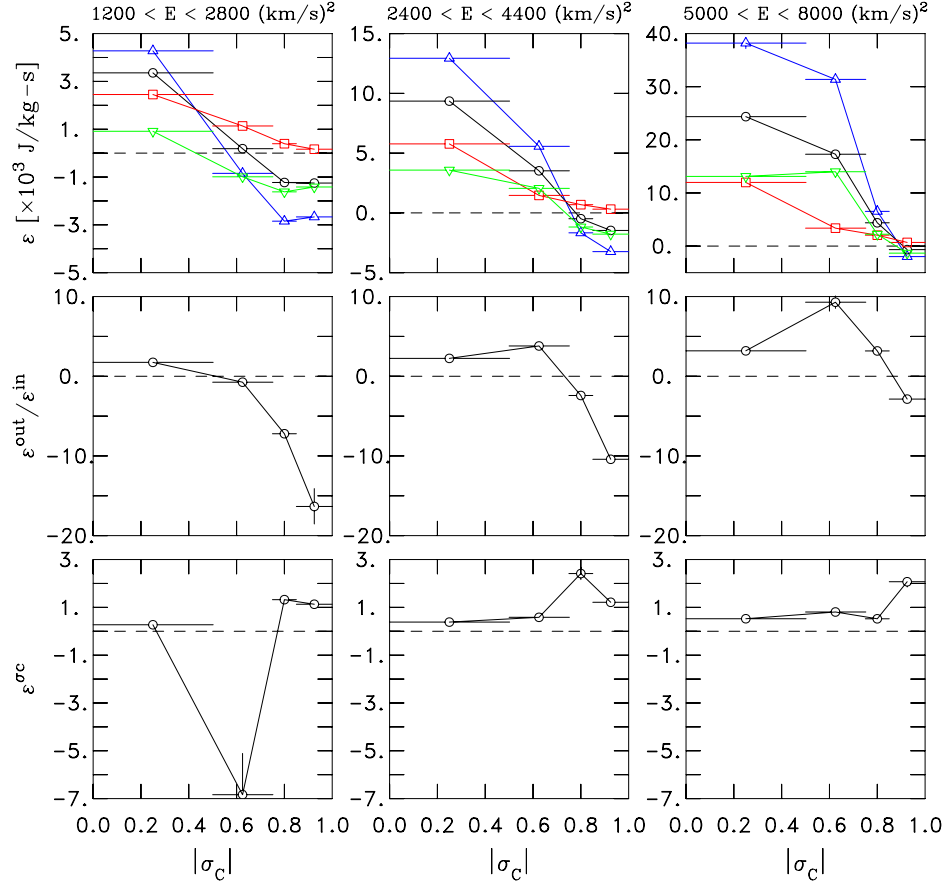


Figure 8.3: (top row) Signed cascade rate computed by averaging over all lags in isotropic geometry analysis. Blue triangles represent outward propagating energy cascade, red squares are inward propagating energy cascade, black circles give total energy cascade, and green inverted triangles represent the cross-helicity cascade. (middle row) Ratio of rate of cascade for outward propagating fluctuations over rate of cascade for inward propagating fluctuations. (bottom row) Ratio of helicity cascade rate to total energy cascade rate ϵ^{σ^C} . See Tables 8.1 and 8.2. Figure reproduced from Stawarz et al. (2010).

Table 8.1: Cascade statistics from isotropic geometry Figure 8.2. Table reproduced from Stawarz et al. (2010).

Energy Range [(km/s) ²]	$ \sigma_C $ Range	# Samples	ϵ_{iso}^{out}	ϵ_{iso}^{in}	ϵ_{iso}^T
[$\times 10^3$ Joules/kg-s]					
1200 – 2800	$0.00 < \sigma_C < 0.50$	455	4.28 ± 0.10	2.45 ± 0.09	3.36 ± 0.07
1200 – 2800	$0.50 < \sigma_C < 0.75$	581	-0.85 ± 0.06	1.14 ± 0.05	0.19 ± 0.04
1200 – 2800	$0.75 < \sigma_C < 0.85$	340	-2.85 ± 0.05	0.39 ± 0.02	-1.23 ± 0.03
1200 – 2800	$0.85 < \sigma_C < 1.00$	135	-2.67 ± 0.07	0.16 ± 0.02	-1.25 ± 0.04
2400 – 4400	$0.00 < \sigma_C < 0.50$	239	12.94 ± 0.20	5.77 ± 0.15	9.35 ± 0.13
2400 – 4400	$0.50 < \sigma_C < 0.75$	306	5.57 ± 0.13	1.47 ± 0.07	3.52 ± 0.08
2400 – 4400	$0.75 < \sigma_C < 0.85$	310	-1.67 ± 0.09	0.69 ± 0.03	-0.49 ± 0.05
2400 – 4400	$0.85 < \sigma_C < 1.00$	373	-3.24 ± 0.05	0.31 ± 0.01	-1.47 ± 0.03
5000 – 8000	$0.00 < \sigma_C < 0.50$	52	38.21 ± 1.02	11.98 ± 0.83	24.37 ± 0.66
5000 – 8000	$0.50 < \sigma_C < 0.75$	94	31.38 ± 0.56	3.38 ± 0.27	17.29 ± 0.31
5000 – 8000	$0.75 < \sigma_C < 0.85$	127	6.54 ± 0.27	2.06 ± 0.12	4.39 ± 0.15
5000 – 8000	$0.85 < \sigma_C < 1.00$	285	-1.97 ± 0.12	0.69 ± 0.02	-0.66 ± 0.06

Table 8.2: Cascade statistics derived from isotropic geometry Figure 8.2. Table reproduced from Stawarz et al. (2010).

Energy Range [(km/s) ²]	$ \sigma_C $ Range	$\epsilon_{iso}^{out}/\epsilon_{iso}^{in}$	ϵ^C	ϵ^{σ_C}
[$\times 10^3$ Joules/kg-s]				
1200 – 2800	$0.00 < \sigma_C < 0.50$	1.75 ± 0.08	0.91 ± 0.07	0.27 ± 0.02
1200 – 2800	$0.50 < \sigma_C < 0.75$	-0.74 ± 0.06	-0.99 ± 0.04	-6.84 ± 1.71
1200 – 2800	$0.75 < \sigma_C < 0.85$	-7.21 ± 0.40	-1.62 ± 0.03	1.32 ± 0.04
1200 – 2800	$0.85 < \sigma_C < 1.00$	-16.34 ± 2.20	-1.42 ± 0.04	1.13 ± 0.04
2400 – 4400	$0.00 < \sigma_C < 0.50$	2.24 ± 0.07	3.58 ± 0.13	0.38 ± 0.01
2400 – 4400	$0.50 < \sigma_C < 0.75$	3.80 ± 0.21	2.05 ± 0.08	0.58 ± 0.02
2400 – 4400	$0.75 < \sigma_C < 0.85$	-2.42 ± 0.16	-1.18 ± 0.05	2.41 ± 0.25
2400 – 4400	$0.85 < \sigma_C < 1.00$	-10.42 ± 0.51	-1.77 ± 0.03	1.21 ± 0.03
5000 – 8000	$0.00 < \sigma_C < 0.50$	3.19 ± 0.24	13.11 ± 0.66	0.52 ± 0.03
5000 – 8000	$0.50 < \sigma_C < 0.75$	9.29 ± 0.77	14.00 ± 0.31	0.81 ± 0.02
5000 – 8000	$0.75 < \sigma_C < 0.85$	3.18 ± 0.23	2.24 ± 0.15	0.52 ± 0.04
5000 – 8000	$0.85 < \sigma_C < 1.00$	-2.87 ± 0.20	-1.33 ± 0.06	2.07 ± 0.22

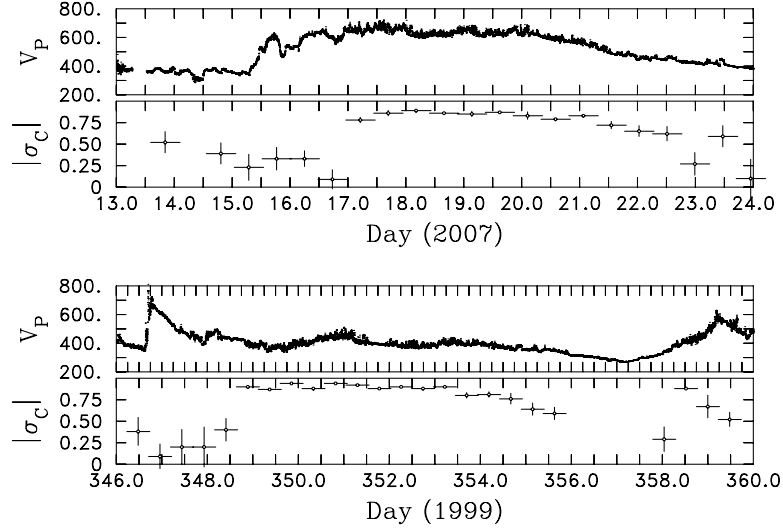


Figure 8.4: Examples of wind speed and σ_C for 2 two-week periods. The high $|\sigma_C|$ occurs in solar wind regions isolated from shear and can occur in relatively slow wind and during solar maximum. Figure reproduced from Stawarz et al. (2010).

cross-helicity when $|\sigma_C|$ is large. It never exceeds several times the rate of total energy cascade, but is $\ll 1$ when $|\sigma_C|$ is small.

Figure 8.4 shows two time series with typical examples of high $|\sigma_C|$ states. The first example is a fast wind from solar minimum that follows a CIR with significant separation and precedes a rarefaction region by a similar spacing. This is the classic high $|\sigma_C|$ state reported by Belcher and Davis (1971). We contend, as does Roberts et al. (1987), that this is a region of low shear where little driving of new turbulent energy is present. In contrast, the CIR and rarefaction region are likely areas where the turbulence is “stirred”. The high $|\sigma_C|$ intervals shown here come from all three energy ranges studied in Figure 8.2. The second example is from near solar maximum and focuses on an interval where the solar wind never achieves what is normally considered a fast wind speed. There is a shock early in the interval followed by a current sheet crossing and a stream interface late in the interval, but between these transients (from day 349 to 353) there is an extended region of isolated flow without apparent sources of shear in which the value of $|\sigma_C|$ is consistently high. Not all intervals with high $|\sigma_C|$ are fast streams, but they do tend to be isolated flows removed from regions of strong shear.

8.3 Hybrid Analysis

Figure 8.5 shows the results of our analysis using the hybrid formalism of Section 5.3. The color convention from Figure 8.2 continues with dashed lines representing the 1D (parallel) component and solid lines representing the 2D (perpendicular) component. (Note that a factor of 2 difference exists between the conversion of D_3 to ϵ that favors the 2D cascade: If $D_{3,\perp} = D_{3,\parallel}$ then $\epsilon_{\perp} = 2\epsilon_{\parallel}$ and the cascade is effectively isotropic.) While we again observe elements of D_3 turning negative as $|\sigma_C|$ increases, it is again the outward-propagating component (blue) that is most negative while the inward-propagating component (red) re-

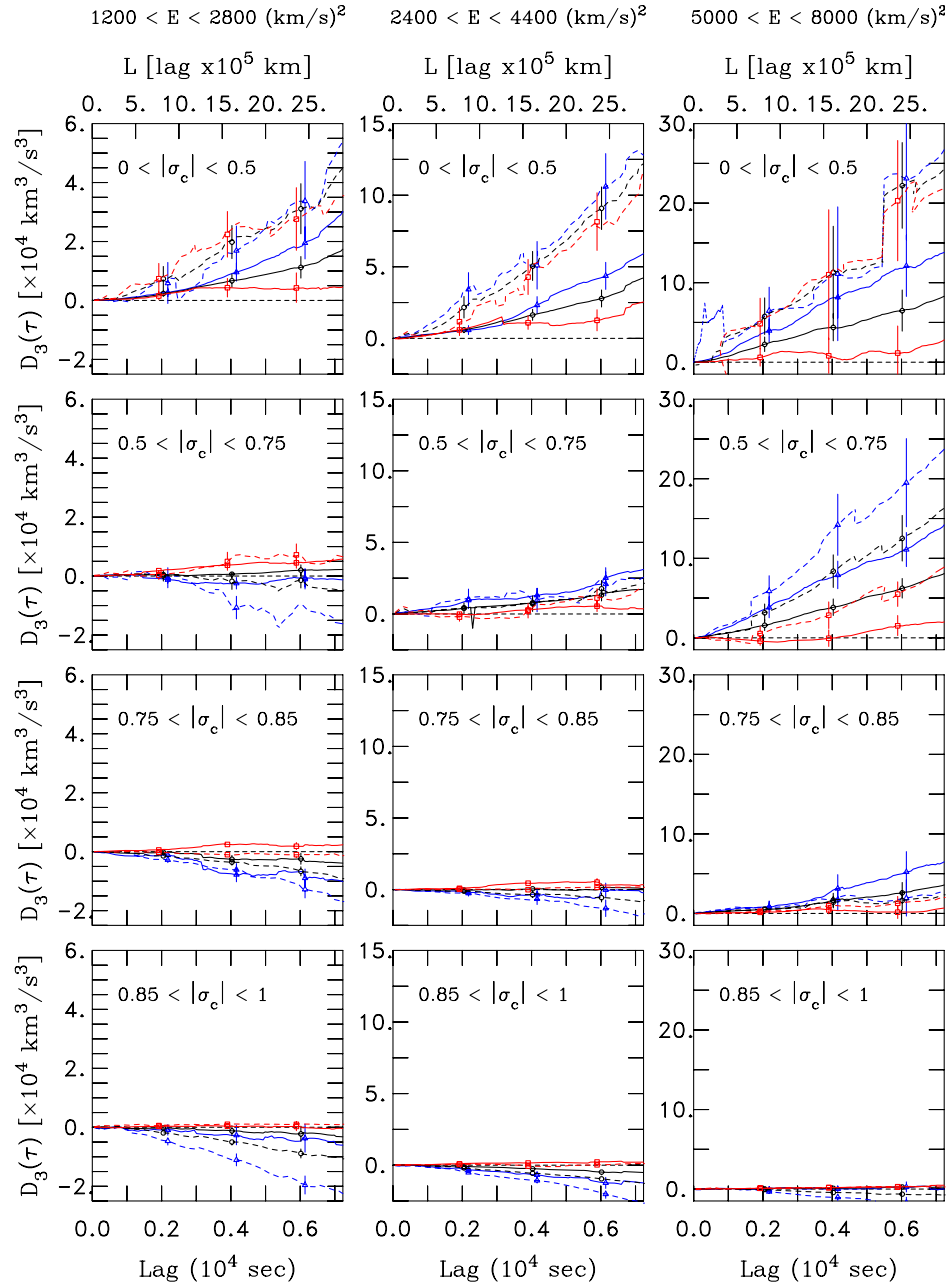


Figure 8.5: Same as in Figure 8.2 except solid curves are 2D analysis and dashed curves are 1D analysis. Sample error bars are again shown. Note that low sample numbers can lead to large uncertainties and functions that deviate from linearity when isotropic expression is further divided into 1D/2D hybrid expressions. Figure reproduced from Stawarz et al. (2010).

Table 8.3: Out and in cascade statistics from Figure 8.5 for 2D and 1D components. Table reproduced from Stawarz et al. (2010).

Energy Range [(km/s) ²]	$ \sigma_C $ Range	ϵ_{2D}^{out} [$\times 10^3$ Joules/kg-s]	ϵ_{2D}^{in} [$\times 10^3$ Joules/kg-s]	ϵ_{1D}^{out} [$\times 10^3$ Joules/kg-s]	ϵ_{1D}^{in} [$\times 10^3$ Joules/kg-s]
1200 – 2800	$0.00 < \sigma_C < 0.50$	2.23 ± 0.08	1.01 ± 0.08	2.38 ± 0.14	3.01 ± 0.12
1200 – 2800	$0.50 < \sigma_C < 0.75$	-0.45 ± 0.06	1.05 ± 0.04	-1.09 ± 0.05	0.55 ± 0.04
1200 – 2800	$0.75 < \sigma_C < 0.85$	-1.76 ± 0.08	0.53 ± 0.03	-0.97 ± 0.03	-0.10 ± 0.01
1200 – 2800	$0.85 < \sigma_C < 1.00$	-0.83 ± 0.10	0.08 ± 0.03	-1.66 ± 0.03	0.14 ± 0.01
2400 – 4400	$0.00 < \sigma_C < 0.50$	5.95 ± 0.17	2.97 ± 0.15	8.77 ± 0.24	6.78 ± 0.22
2400 – 4400	$0.50 < \sigma_C < 0.75$	4.49 ± 0.14	0.53 ± 0.07	2.11 ± 0.12	0.59 ± 0.08
2400 – 4400	$0.75 < \sigma_C < 0.85$	-0.88 ± 0.12	0.86 ± 0.04	-1.07 ± 0.06	0.11 ± 0.02
2400 – 4400	$0.85 < \sigma_C < 1.00$	-1.97 ± 0.07	0.53 ± 0.02	-1.69 ± 0.03	0.04 ± 0.01
5000 – 8000	$0.00 < \sigma_C < 0.50$	20.89 ± 0.70	3.27 ± 0.55	19.31 ± 0.93	18.68 ± 0.99
5000 – 8000	$0.50 < \sigma_C < 0.75$	21.16 ± 0.49	1.02 ± 0.27	16.21 ± 0.52	4.57 ± 0.22
5000 – 8000	$0.75 < \sigma_C < 0.85$	7.06 ± 0.36	0.99 ± 0.13	2.47 ± 0.21	0.81 ± 0.07
5000 – 8000	$0.85 < \sigma_C < 1.00$	0.25 ± 0.13	0.59 ± 0.03	-1.31 ± 0.06	0.30 ± 0.01

mains positive. $D_{3,\parallel}$ (dashed curves) turns more negative than $D_{3,\perp}$ (solid curves). Again, higher energy states require higher values of σ_C before negative cascade rates are observed. Table 8.3 lists the values of ϵ derived from Figure 8.5.

We now compute more refined quantities. In addition to considering the 1D and 2D moments and their associated cascade rates separately, we can combine third-moments in a hybrid manner to get ϵ_{hybrid}^{out} and ϵ_{hybrid}^{in} . Table 8.4 shows these hybrid cascade rates according to in/out propagation derived from averaging of the third-moments divided by lag. Table 8.5 sums in/out propagation to list cascade rates according to 2D and 1D components. (Note, the total energy cascade rates in Table 8.5 differ from values in Table 8.4 by 1σ due to separate averaging of combined third-moment functions.) Table 8.6 computes differences in individual energy cascade rates to obtain cross-helicity cascade rates according to 2D and 1D components.

Figure 8.6 plots these results. Figure 8.6 (top row) shows the computed energy cascade rates associated with the functions D_3 plotted in Figure 8.5. In general, the energy cascade for the 2D and 1D components exhibit comparable behavior and are similar to the in/out results shown in Figure 8.3. The 2D cascade of helicity tends to exceed the 1D cascade at low $|\sigma_C|$ and reverse at high values, but to leading order the cascade of ϵ^C appears nearly isotropic in the hybrid analysis. The total cascade rate for outward propagating fluctuations, inward propagating fluctuations, and total energy (Figure 8.6 2nd row) behaves in much the same manner as is seen in the isotropic calculation. As seen in the Stawarz et al. (2009) analysis (Chapter 7), the hybrid calculation yields slightly greater values for total energy cascade, but the difference is on the order of 10%. For low values of $|\sigma_C|$ the cascade rate for total energy increases with the energy level. A trend for small ϵ^C cascade rate evident at low $|\sigma_C|$ in the isotropic analysis is more evident here, not because ϵ^C is reduced, but because the energy cascade rate of the inward propagating component at high energy content is elevated. The values of ϵ^C agree well between the isotropic and hybrid

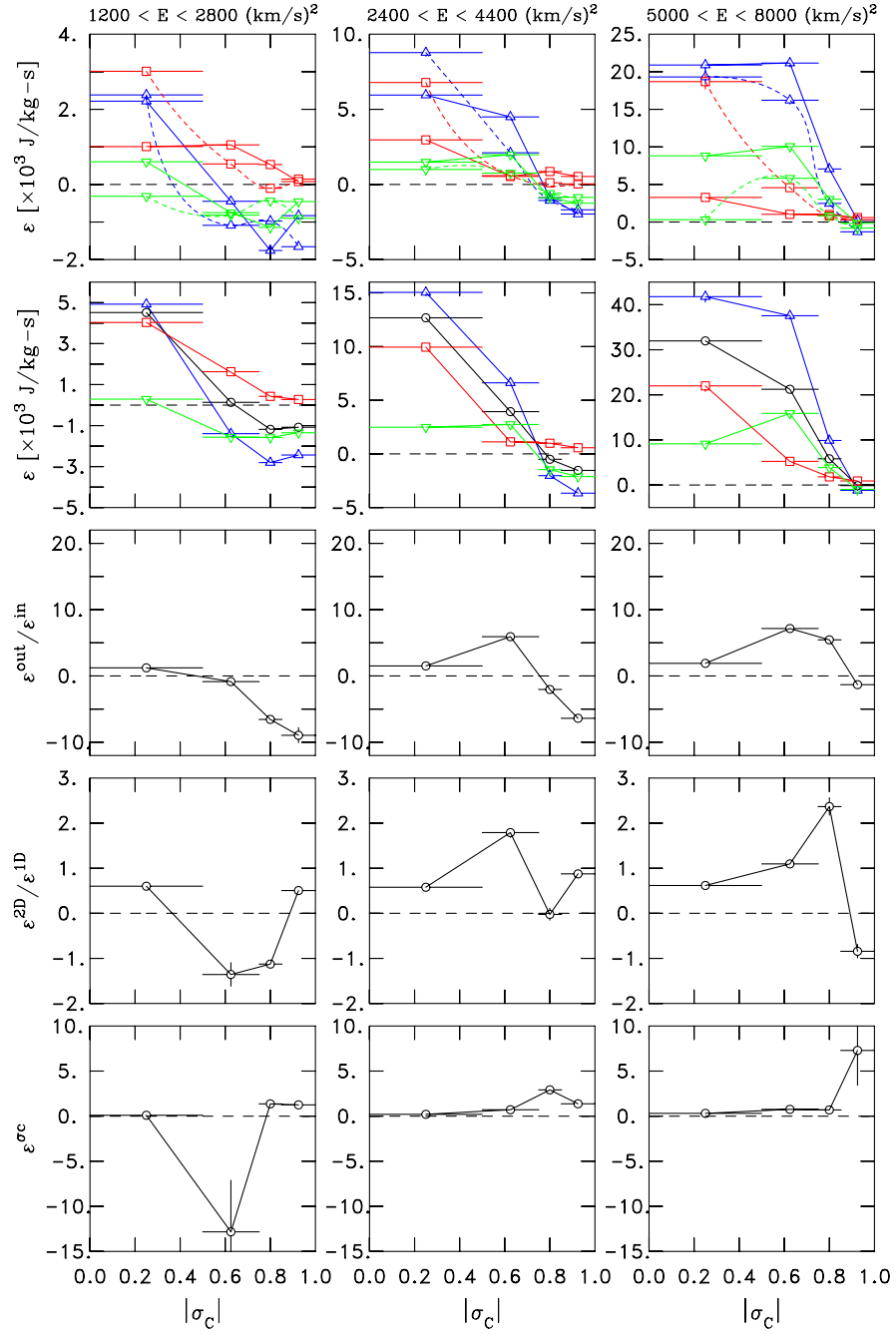


Figure 8.6: (top row) Signed energy and helicity cascade rates computed by averaging over all lags in hybrid model. Blue triangles are outward propagation energy cascade, red squares are inward propagation energy cascade, green inverted triangles are helicity cascade, solid lines are 2D component, and dashed lines are 1D component. (second row) Sum of 2D + 1D components to yield net energy cascade rates for outward propagating and inward propagating components along with total energy. Green is total helicity cascade rate. (third row) Sum of 2D + 1D components to yield the ratio $\epsilon^{out}/\epsilon^{in}$. (fourth row) Sum of outward propagating and inward propagating components to compute ratio of energy cascade for 2D geometry over energy cascade for 1D geometry. (bottom row) Ratio of helicity cascade rate to total energy cascade rate $\epsilon^{\sigma c}$. Figure reproduced from Stawarz et al. (2010).

Table 8.4: Net out and in cascade statistics from hybrid geometry. Table reproduced from Stawarz et al. (2010).

Energy Range [(km/s) ²]	$ \sigma_C $ Range	ϵ_{hybrid}^{out}	ϵ_{hybrid}^{in}	ϵ_{hybrid}^T	$\epsilon_{hybrid}^{out}/\epsilon_{hybrid}^{in}$
		[$\times 10^3$ Joules/kg-s]			
1200 – 2800	$0.00 < \sigma_C < 0.50$	4.93 ± 0.17	4.03 ± 0.16	4.52 ± 0.12	1.22 ± 0.06
1200 – 2800	$0.50 < \sigma_C < 0.75$	-1.39 ± 0.09	1.63 ± 0.06	0.13 ± 0.05	-0.86 ± 0.06
1200 – 2800	$0.75 < \sigma_C < 0.85$	-2.80 ± 0.08	0.43 ± 0.03	-1.18 ± 0.04	-6.56 ± 0.48
1200 – 2800	$0.85 < \sigma_C < 1.00$	-2.44 ± 0.10	0.27 ± 0.03	-1.08 ± 0.05	-8.95 ± 1.11
2400 – 4400	$0.00 < \sigma_C < 0.50$	15.04 ± 0.30	9.94 ± 0.28	12.68 ± 0.21	1.51 ± 0.05
2400 – 4400	$0.50 < \sigma_C < 0.75$	6.62 ± 0.19	1.12 ± 0.11	3.94 ± 0.11	5.92 ± 0.61
2400 – 4400	$0.75 < \sigma_C < 0.85$	-2.03 ± 0.13	0.99 ± 0.05	-0.50 ± 0.07	-2.04 ± 0.16
2400 – 4400	$0.85 < \sigma_C < 1.00$	-3.66 ± 0.08	0.57 ± 0.02	-1.54 ± 0.04	-6.39 ± 0.28
5000 – 8000	$0.00 < \sigma_C < 0.50$	41.77 ± 1.22	21.99 ± 1.23	31.97 ± 0.87	1.90 ± 0.12
5000 – 8000	$0.50 < \sigma_C < 0.75$	37.55 ± 0.73	5.25 ± 0.35	21.23 ± 0.41	7.15 ± 0.50
5000 – 8000	$0.75 < \sigma_C < 0.85$	9.88 ± 0.43	1.81 ± 0.15	5.81 ± 0.23	5.45 ± 0.51
5000 – 8000	$0.85 < \sigma_C < 1.00$	-1.19 ± 0.15	0.90 ± 0.03	-0.14 ± 0.08	-1.32 ± 0.17

Table 8.5: Energy cascade statistics from Figure 8.5 for 2D and 1D components. Table reproduced from Stawarz et al. (2010).

Energy Range [(km/s) ²]	$ \sigma_C $ Range	ϵ_{2D}^T	ϵ_{1D}^T	$\epsilon_{2D}^T/\epsilon_{1D}^T$
		[$\times 10^3$ Joules/kg-s]		
1200 – 2800	$0.00 < \sigma_C < 0.50$	1.63 ± 0.06	2.71 ± 0.09	0.60 ± 0.03
1200 – 2800	$0.50 < \sigma_C < 0.75$	0.31 ± 0.04	-0.23 ± 0.03	-1.36 ± 0.26
1200 – 2800	$0.75 < \sigma_C < 0.85$	-0.61 ± 0.04	-0.54 ± 0.02	1.13 ± 0.08
1200 – 2800	$0.85 < \sigma_C < 1.00$	-0.38 ± 0.05	-0.75 ± 0.02	0.50 ± 0.07
2400 – 4400	$0.00 < \sigma_C < 0.50$	4.55 ± 0.11	7.87 ± 0.17	0.58 ± 0.02
2400 – 4400	$0.50 < \sigma_C < 0.75$	2.52 ± 0.08	1.41 ± 0.07	1.79 ± 0.11
2400 – 4400	$0.75 < \sigma_C < 0.85$	0.01 ± 0.06	-0.49 ± 0.03	-0.02 ± 0.13
2400 – 4400	$0.85 < \sigma_C < 1.00$	-0.72 ± 0.04	-0.83 ± 0.02	0.87 ± 0.05
5000 – 8000	$0.00 < \sigma_C < 0.50$	11.79 ± 0.46	19.11 ± 0.69	0.62 ± 0.03
5000 – 8000	$0.50 < \sigma_C < 0.75$	11.08 ± 0.28	10.11 ± 0.29	1.10 ± 0.04
5000 – 8000	$0.75 < \sigma_C < 0.85$	4.02 ± 0.19	1.70 ± 0.11	2.37 ± 0.19
5000 – 8000	$0.85 < \sigma_C < 1.00$	0.42 ± 0.07	-0.50 ± 0.03	-0.84 ± 0.15

Table 8.6: Cascade statistics derived from hybrid geometry and Figure 8.5 for cross helicity. Table reproduced from Stawarz et al. (2010).

Energy Range [(km/s) ²]	$ \sigma_C $ Range	ϵ_{2D}^C	ϵ_{1D}^C [$\times 10^3$ Joules/kg-s]	ϵ_{hybrid}^C	$\epsilon_{hybrid}^{\sigma_C}$
1200 – 2800	$0.00 < \sigma_C < 0.50$	0.60 ± 0.06	-0.31 ± 0.09	0.29 ± 0.11	0.10 ± 0.03
1200 – 2800	$0.50 < \sigma_C < 0.75$	-0.75 ± 0.04	-0.82 ± 0.03	-1.57 ± 0.05	-12.83 ± 5.68
1200 – 2800	$0.75 < \sigma_C < 0.85$	-1.14 ± 0.04	-0.44 ± 0.02	-1.58 ± 0.04	1.40 ± 0.06
1200 – 2800	$0.85 < \sigma_C < 1.00$	-0.45 ± 0.05	-0.90 ± 0.02	-1.35 ± 0.05	1.25 ± 0.08
2400 – 4400	$0.00 < \sigma_C < 0.50$	1.49 ± 0.11	1.00 ± 0.16	2.48 ± 0.20	0.20 ± 0.02
2400 – 4400	$0.50 < \sigma_C < 0.75$	1.98 ± 0.08	0.76 ± 0.07	2.74 ± 0.11	0.71 ± 0.03
2400 – 4400	$0.75 < \sigma_C < 0.85$	-0.87 ± 0.06	-0.59 ± 0.03	-1.46 ± 0.07	2.92 ± 0.41
2400 – 4400	$0.85 < \sigma_C < 1.00$	-1.25 ± 0.04	-0.86 ± 0.02	-2.11 ± 0.04	1.37 ± 0.04
5000 – 8000	$0.00 < \sigma_C < 0.50$	8.81 ± 0.45	0.31 ± 0.68	9.12 ± 0.81	0.31 ± 0.03
5000 – 8000	$0.50 < \sigma_C < 0.75$	10.07 ± 0.28	5.82 ± 0.28	15.89 ± 0.40	0.75 ± 0.02
5000 – 8000	$0.75 < \sigma_C < 0.85$	3.04 ± 0.19	0.83 ± 0.11	3.87 ± 0.22	0.69 ± 0.05
5000 – 8000	$0.85 < \sigma_C < 1.00$	-0.17 ± 0.07	-0.80 ± 0.03	-0.98 ± 0.07	7.29 ± 3.85

analyses. As with the isotropic analysis, the value of ϵ^C again falls in line with the energy cascade rates for higher $|\sigma_C|$. We again see the reversal in the cascade rate of the outward propagating fluctuations at intermediate values of $|\sigma_C|$ that leads to a net negative cascade rate for total energy when $|\sigma_C|$ is sufficiently large. The ratio $\epsilon^{out}/\epsilon^{in}$ (Figure 8.6 3rd row) demonstrates this clearly and again behaves in much the same manner as in the isotropic calculation: $|\epsilon^{out}/\epsilon^{in}| > 1$ consistently indicating that $|\epsilon^{out}| > |\epsilon^{in}|$ except when $\epsilon^{out} \simeq 0$ and changing sign. By summing the outward propagating and inward propagating components, we can compare the strength of the 2D and 1D cascades (Figure 8.6 4th row). We find $|\epsilon_{2D}^T/\epsilon_{1D}^T| < 2.5$ and most often $\simeq 1$. This suggests an anisotropic cascade of nearly equal proportion (nearly isotropic). Since fluctuation levels in fast winds generally have higher energy than in slow winds, this would seem to be at odds with MacBride et al. (2008) who find a strongly anisotropic cascade in fast winds. However, Figure 8.4 shows that not all examples of high $|\sigma_C|$ come from fast winds. We return to this point below. The hybrid calculation of ϵ^{σ_C} (Figure 8.6 bottom row) behaves again in much the same manner as is seen in the isotropic calculation except, we note a scale change to accommodate the greater range of values. As with the isotropic analysis, when data is selected without regard for $|\sigma_C|$, all cascade rates are positive for each of the three energy ranges and for each component of the turbulence.

It is commonly held that fast winds demonstrate greater fluctuation energy than slow winds and this is true to a degree. MacBride et al. (2008) demonstrate that fast winds exhibit a strongly anisotropic cascade at these same spatial scales, with the energy moving preferentially toward perpendicular wave vectors. This is interpreted to mean that the turbulence is evolving away from the field-aligned wave vectors that dominate fast wind observations (Dasso et al., 2005) and toward the anticipated 2D state predicted by theory (Shebalin et al., 1983; Higdon, 1984; Goldreich and Sridhar, 1995; Ghosh et al., 1998a,b; Matthaeus et al., 1998). We do not measure this same strongly anisotropic cascade for the

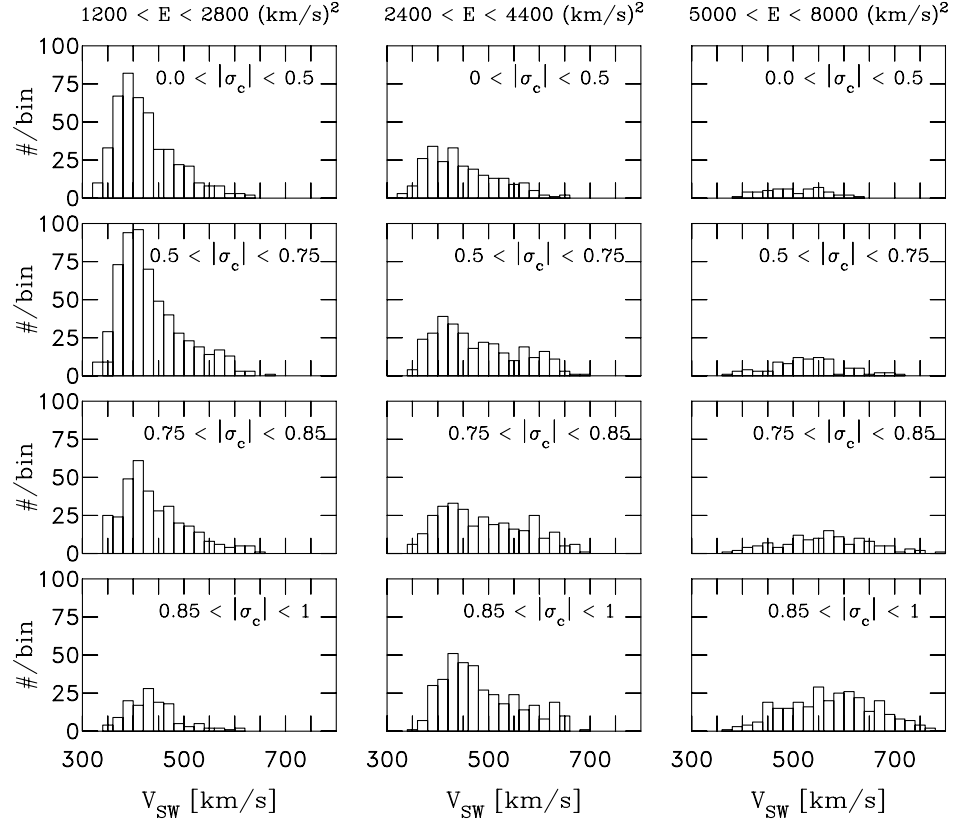


Figure 8.7: Distribution of wind speeds for 12 hr samples grouped in 20 km/s bins for each of the 12 panels in Figures 8.2 and 8.5. Figure reproduced from Stawarz et al. (2010).

higher energy subsets. Figure 8.7 explains why - the anticipated shift toward fast winds as the energy increases proves to be subtle with a sustained admixture of fast and slow wind conditions. Dasso et al. (2005) demonstrate that the slow winds at 1 AU are already largely 2D while MacBride et al. (2008) show they possess a more isotropic cascade. The fast wind component increases, but a sufficient number of slow wind observations remain to invalidate the comparison between our high energy, large $|\sigma_c|$ observations and the fast wind results of MacBride et al. (2008). So, selecting for high energy fluctuations with large values of $|\sigma_c|$ does not necessarily focus exclusively on fast wind flows.

8.4 Selecting for Heating Rate

In the isotropic and hybrid analyses of Sections 8.2 and 8.3, we select intervals with similar energy content and vary σ_c . Another method is to select intervals that are expected to have similar cascade rates. One way to get similar cascade rates, barring consideration of the new back-transfer result shown here, is to select intervals expected by solar wind studies to possess similar heating rates. As we do in the previous chapter, the proton heating rate at 1 AU for a given interval can be determined using Eq. 3.25.

In Chapter 7, we demonstrate that when observations are selected according to values of $V_{SW}T_P$, the computed average energy cascade rate is in close agreement with the expected rate of proton heating with 10-40% of the cascade remaining to heat electrons. As a further

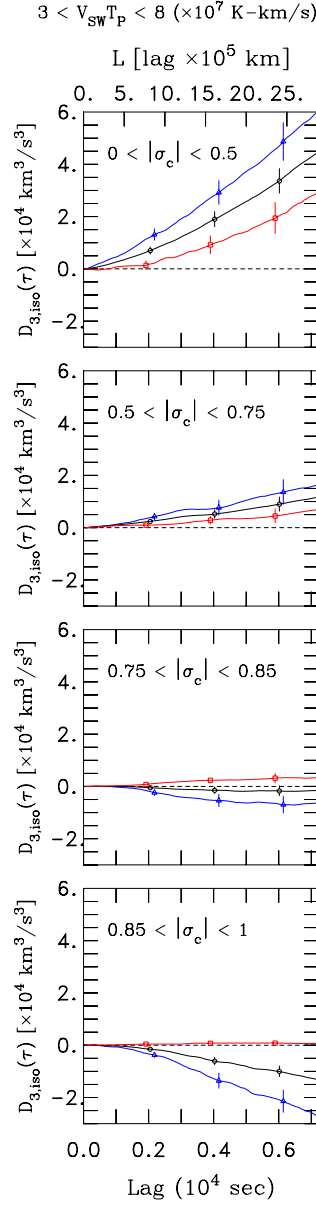


Figure 8.8: Computed values for $D_{3,ISO}$ using 12 hr samples and 10 years of data for samples with $3 < V_{SW} T_P < 8 [\times 10^7] \text{ K-km/s}$. Horizontal rows are divided into four helicity ranges. Blue (red) denotes outward (inward) propagation. Black is total energy. Figure reproduced from Stawarz et al. (2010).

Table 8.7: Cascade statistics from isotropic geometry Figure 8.8. Table reproduced from Stawarz et al. (2010).

$ \sigma_C $ Range	# Samples	ϵ_{iso}^{out}	ϵ_{iso}^{in} [$\times 10^3$ Joules/kg-s]	ϵ_{iso}^T	ϵ_{iso}^C
$0.00 < \sigma_C < 0.50$	419	11.01 ± 0.17	3.11 ± 0.15	7.04 ± 0.12	3.95 ± 0.11
$0.50 < \sigma_C < 0.75$	490	3.22 ± 0.11	1.24 ± 0.07	2.22 ± 0.07	0.99 ± 0.07
$0.75 < \sigma_C < 0.85$	368	-1.76 ± 0.09	0.85 ± 0.04	-0.43 ± 0.05	-1.31 ± 0.05
$0.85 < \sigma_C < 1.00$	500	-3.95 ± 0.10	0.30 ± 0.02	-1.83 ± 0.05	-2.13 ± 0.05
$0.00 < \sigma_C < 1.00$	1777	2.10 ± 0.06	1.36 ± 0.04	1.73 ± 0.04	0.37 ± 0.04

example of the back-transfer physics, we use only those 12 hr intervals that fall into range 4 of the 7 $V_{SW}T_P$ ranges in the previous chapter: $3.0 < V_{SW}T_P < 8.0 [\times 10^7] \text{K-km/s}$. The average heating rate for this subset is $\epsilon_{\text{heat}} = 1.8 \times 10^3 \text{ J/kg-s}$ while the computed cascade rates are $1.9 \times 10^3 \text{ J/kg-s}$ for the isotropic analysis and $2.5 \times 10^3 \text{ J/kg-s}$ for the hybrid analysis. Figure 8.8 shows the results of our re-analysis of this same subset using the isotropic formalism. As above, when $|\sigma_C|$ is large the cascade rate of the dominant outward-propagating component reverses sign and with sufficiently large $|\sigma_C|$, the total energy cascade rate reverses. Table 8.7 lists the inferred cascade rates derived from Figure 8.8. Average temperatures are $\sim 10^5 \text{ K}$ for each subset due to data selection. The distribution of wind speeds for the 4 σ_C ranges have means that vary from 450 to 485 km/s and standard deviations less than 70 km/s. The mixture of fast and slow wind intervals is about constant with changing $|\sigma_C|$.

The bottom row of Table 8.7 shows the computed cascade rates and average temperature when the $V_{SW}T_P$ range is not subset for $|\sigma_C|$. No net back-transfer of energy is observed in any component or the total and the temperature is essentially unchanged. This further demonstrates that the back-transfer condition is common, but that the rates are small compared with the forward-transfer rates at lower $|\sigma_C|$. The fact that average temperatures appear not to depend on the existence of back-transfer conditions raises important questions that we address in Section 8.6.

8.5 Solar Minimum

We continue our demonstration with an examination of solar minimum years 2005 through mid-year of 2008. We perform this analysis as above while dividing into subsets for wind speed and fluctuation energy. As before, we remove shocks and their drivers, although there are very few shocks during these years and most are quite weak. For simplicity, we again limit our presentation to the isotropic formalism.

Figure 8.9 shows our analysis of the slow wind. The top panel shows the distribution of fluctuation energy for the 12 hr samples. We limit our analysis to the energy range $1000 < E < 3000 (\text{km/s})^2$. There are too few observations of $|\sigma_C| > 0.85$ to obtain an accurate estimate of D_3 for this instance. There is again a strong forward cascade for low cross-helicity with a reversal of the cascade for high $|\sigma_C|$ values. See Table 8.8 for cascade rates.

Figure 8.10 shows our analysis of the fast wind events. The top panel again shows the distribution of fluctuation energy for the 12 hr samples. We limit our analysis to the energy

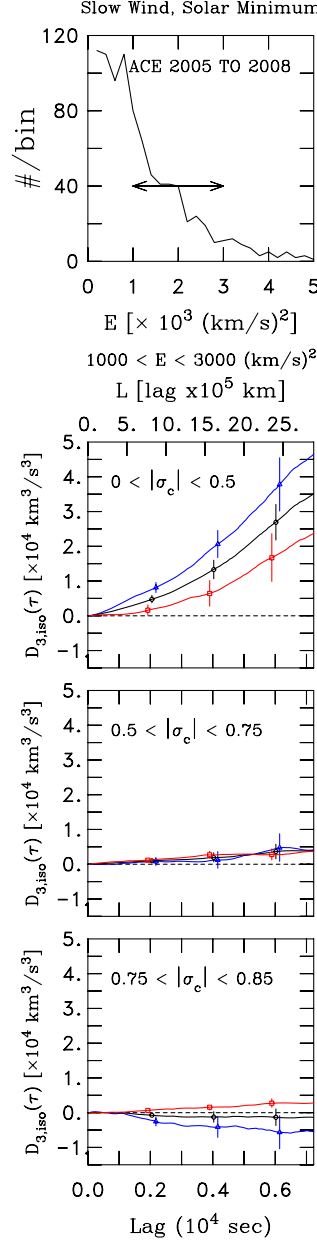


Figure 8.9: Analysis of slow wind $V_{SW} < 450 \text{ km/s}$ for solar minimum observations. (top) Distribution of fluctuation energy for 12 hr samples in $200 (\text{km/s})^2$ bins. Arrow marks $1000 < E < 3000 (\text{km/s})^2$ range chosen for analysis. (remainder) Computed values for $D_{3,ISO}$ using 12 hr samples and 3.5 years of data. There are insufficient samples to obtain good estimates for $0.85 < |\sigma_C| < 1.0$. Blue (red) denotes outward (inward) propagation. Black is total energy. Figure reproduced from Stawarz et al. (2010).

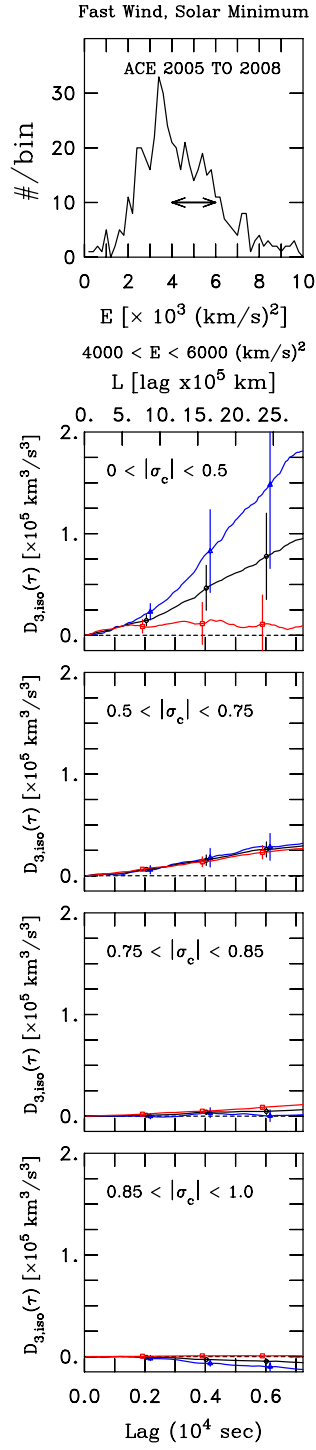


Figure 8.10: Same as Figure 8.9 except fast wind $V_{SW} > 550 \text{ km/s}$. Figure reproduced from Stawarz et al. (2010).

Table 8.8: Cascade statistics from isotropic geometry solar minimum slow wind Figure 8.9. Table reproduced from Stawarz et al. (2010).

$ \sigma_C $ Range	# Samples	ϵ_{iso}^{out}	ϵ_{iso}^{in}	ϵ_{iso}^T	ϵ_{iso}^C
			[$\times 10^3$ Joules/kg-s]		
$0.00 < \sigma_C < 0.50$	187	7.40 ± 0.15	2.22 ± 0.14	4.77 ± 0.10	2.59 ± 0.10
$0.50 < \sigma_C < 0.75$	142	0.59 ± 0.10	1.14 ± 0.05	0.89 ± 0.06	-0.28 ± 0.06
$0.75 < \sigma_C < 0.85$	51	-1.49 ± 0.12	0.61 ± 0.03	-0.45 ± 0.06	-1.05 ± 0.06

Table 8.9: Cascade statistics from isotropic geometry solar minimum fast wind Figure 8.9. Table reproduced from Stawarz et al. (2010).

$ \sigma_C $ Range	# Samples	ϵ_{iso}^{out}	ϵ_{iso}^{in}	ϵ_{iso}^T	ϵ_{iso}^C
			[$\times 10^3$ Joules/kg-s]		
$0.00 < \sigma_C < 0.50$	11	21.60 ± 1.10	7.97 ± 0.76	15.77 ± 0.70	6.82 ± 0.70
$0.50 < \sigma_C < 0.75$	30	6.23 ± 0.36	6.37 ± 0.20	6.35 ± 0.21	-0.07 ± 0.21
$0.75 < \sigma_C < 0.85$	74	0.27 ± 0.19	2.30 ± 0.06	1.33 ± 0.10	-1.02 ± 0.10
$0.85 < \sigma_C < 1.00$	60	-2.39 ± 0.13	0.30 ± 0.03	-1.05 ± 0.06	-1.35 ± 0.06

range $4000 < E < 8000$ (km/s)². The number of samples for $|\sigma_C| < 0.5$ is not large, so uncertainties for the D_3 estimates are large. Nevertheless, the figure clearly shows a strong forward cascade for low $|\sigma_C|$ with a reversal at high $|\sigma_C|$ consistent with all of the events we show in this chapter. See Table 8.9 for cascade rates.

In both the fast and slow wind solar minimum analyses, the results fall in line with previous conclusions. The forward cascade of H_C in low $|\sigma_C|$ states is about half the forward cascade of total energy. In high $|\sigma_C|$ states, the back-transfer of H_C is greater than the energy cascade rate. In both fast and slow wind conditions the energy cascade rate is generally $> 10^3$ Joules/kg-s and exceeds 10^4 Joules/kg-s in the fast wind at low $|\sigma_C|$. This means the solar wind continues to experience heating at 1 AU during solar minimum at a rate that is fully comparable to solar maximum conditions. Since energy injection via shear flow appears to be less than at solar maximum and is generally considered to be more isolated and associated primarily with CIRs, we must conclude that much of the energy cascade at 1 AU is fueled by remnant fluctuations that can be traced back to the acceleration region of the Sun. Furthermore, the back-transfer cascade of energy appears unchanged from solar maximum conditions.

8.6 Cross-Helicity Discussion

The observed forward-transfer of energy to small scales that dominates most of the observations reported in this thesis (MacBride et al., 2005, 2008; Stawarz et al., 2009), has been shown to provide the correct rate of heating to match observations at 1 AU (see Chapter 7). The reservoir of energy at the energy-containing scales is significant and can fuel this process over many AU (Verma et al., 1995; Matthaeus et al., 1996b; Smith et al., 2001) before

pickup ions are needed as a new source of energy in the outer heliosphere (Smith et al., 2001; Isenberg et al., 2003; Smith et al., 2006; Breech et al., 2008). To demonstrate this fact, we take the energy content and cascade rates listed in Table 8.1. For the low energy bin $1200 - 2800 \text{ (km/s)}^2$ the average energy content is $\sim 2000 \text{ (km/s)}^2 = 2. \times 10^9 \text{ Joules/kg}$. Selecting for low helicity $0 < |\sigma_C| < 0.5$ the energy cascade rate $3.4 \times 10^3 \text{ Joules/kg-s}$ implies a cascade lifetime of $(2/3.4) \times 10^6 = 6. \times 10^5 \text{ s} \sim 200 \text{ hrs}$ which probably means that the 12 hr interval is small for estimating the energy content of the energy-containing scales. Still, it suggests a long-lived cascade. Other intervals of low $|\sigma_C|$ show similar time scales associated with the depletion of the energy reservoir.

An observed back-transfer of energy to large scales also places constraints on the observations. Clearly, energy cannot be removed from the thermal pool, so the energy must come from the inertial range itself and this sets a limit on how long this process can continue. There are no studies reporting spectra with strongly depleted inertial ranges, so the back-transfer process must be relatively short lived compared with the time scale for depleting the inertial range. Likewise, the energy content of the large energy-containing scales surpasses that of the inertial range when sufficiently large scales are considered, so the ability to move energy to large scales in order to reinforce observations there is severely limited when the inertial range is the energy reservoir for this process. To compute the limiting time scale for the back-transfer dynamics, we estimate the energy content of the inertial range using the power spectrum shown in Figure 6.3 (MacBride et al., 2008): $P(10^3 \text{ Hz}) \sim 10^5 \text{ (km}^2/\text{s)}$. With a spectral index $-5/3$, we can integrate the inertial range from 10^{-4} Hz , roughly the correlation scale, to 10^{-1} Hz , roughly the dissipation scale, and get an energy content of 10^9 Joules/kg . If we select the energy cascade associated with the high helicity state $0.85 < |\sigma_C| < 1$ from the previous energy range, which is one of the strongest back-transfer rates reported in this study, the time needed for the back-transfer to deplete this energy is $10^6 \text{ s} \sim 300 \text{ hr}$. So depletion of the inertial range by the back-transfer of energy is a slow process that is unlikely to yield observable signatures in the spectrum if shear-driven turbulence dominates within a few AU.

Protracted back-transfer dynamics would suggest that high $|\sigma_C|$ intervals would be cold due to the absence of in situ heating. At 1 AU, they are not particularly cold. Extension of the Vasquez et al. (2007) analysis shows that if normal heating operates over the first few tenths of an AU, inside the Helios orbit, prior to the establishment of the back-transfer cascade subsequently seen at 1 AU, the difference in temperature between a forward-cascade and a back-transfer interval is less than a factor of 2. It seems reasonable to assume that some time must pass before the back-transfer dynamics are sufficiently organized, so we contend that no significant temperature differences should be in evidence at 1 AU.

It is slightly more difficult to determine whether or not the observed dynamic fits into any pre-existing theoretical formalism. The back-transfer of energy we see when σ_C is large strongly suggests an inverse cascade process. Three-dimensional MHD absolute equilibria (Stribling and Matthaeus, 1990) and long-time relaxation to minimal energy states show conditions for which σ_C is back-transferred. However, net energy is forward transferred. Simulations by Ting et al. (1986) and Stribling and Matthaeus (1991) suggest that the cross-helicity cascade does not lead to a final state dictated by inverse cascade dynamics. Likewise, dynamic alignment seems to provide a suitable description for our observations and has been suggested as a possible explanation for high $|\sigma_C|$ observations (Dobrowolny et al., 1980), but the theory of dynamic alignment has been phrased in terms of competing forward-cascade processes. The reported rapid alignment seen during the early phase of

turbulence simulations (Matthaeus et al., 2008) may offer a suitable explanation for these results and the time scale for this process agrees well with observations at 1 AU, but more study is required.

Chapter 9

Large-Scale Velocity Shear

Wan et al. (2009) derives an expression for the MHD energy cascade rate in the presence of a large-scale velocity shear. The third-moment expressions derived in Chapter 5 and utilized in the analyses described in Chapters 6–8 implicitly assume the statistical properties of the fluid are unchanging (homogeneous) throughout space. The presence of a large-scale change in velocity violates this assumption and, as it turns out, introduces additional terms that alter the energy cascade rate. It is also true that the solar wind is full of large-scale rises and falls in solar wind speed (see Section 3.2). It would, therefore, seem a proper analysis of solar wind turbulence requires the inclusion of velocity shear. Were the previous analyses in error? If so, why do we find such good agreement between the energy cascade rate computed without shear and the observed proton heating rates?

In this analyses, we extend the Wan et al. (2009) shear formalism for application to the solar wind and attempt to answer these questions. We find that, because the solar wind contains approximately equal amounts of rising and falling solar wind speed, the third-moment expressions without shear are valid when analyzing large amounts of data with no regard for the direction of velocity shear. However, if one wishes to analyze regions of a single shear direction (such as rarefactions or CIRs), the shear formalism is necessary.

In this chapter, we first describe the extension of third-moment expressions to include shear both in hydrodynamics and MHD and discuss the considerations necessary to extend the MHD expressions for use with single spacecraft solar wind data. We then present the findings of two analyses. The first sorts intervals of data based on the sign and magnitude of the velocity shear within an interval and the second re-performs the heating analysis from Section 7.2 using the velocity shear formalism.

9.1 Theoretical Approach to Large-Scale Velocity Shear

We want to examine the role of large-scale velocity shear in generating and modifying the MHD turbulence in the solar wind near 1 AU. At large scales, kinetic energy significantly exceeds magnetic energy, and thus the energy-containing scale of interplanetary turbulence is dominated by the contribution of velocity shear. This velocity shear is a source of the turbulent energy cascade. In addition, the velocity shear affects the flux of energy through the inertial range and imposes a peculiar anisotropy on the fluctuations in addition to what arises from the presence of the magnetic field.

The role of velocity shear in turbulence is more profitably examined first with respect to hydrodynamics in Section 9.1.1 and then applied to MHD in Section 9.1.2. From the

hydrodynamic case, we see that the anisotropy in the second-moment contributes with the shear to the evaluation of the energy dissipation rate.

9.1.1 Velocity Shear in Hydrodynamic Third-Moments

Remember that the Navier-Stokes equations for incompressible hydrodynamics and constant density can be re-expressed under assumptions of homogeneous fluctuations to yield a relation between the mean rate of energy dissipation per unit mass ϵ and correlation functions of velocity \mathbf{v} . This is the “Kármán-Howarth” equation that we mention in Section 5.1, but do not explicitly derive. If the turbulent system is deemed to be in a statistically steady state the mean dissipation rate is equivalent to the energy cascade rate through the inertial range. Kolmogorov (1941b) uses this expression to derive the hydrodynamic “4/5” Law for the energy cascade rate, seen in Eq. (5.10). This approach is used to describe turbulent fluctuations with a large number of degrees of freedom, such that the fluctuations become well behaved in a statistical sense. In these situations, velocity shears associated with turbulent eddies are presumed to exist over a large range of directions and to vary in speed up and down with equal repetition so that the average shear is zero. More explicitly, \mathbf{v} is a random variable whose average is centered at zero and has the same statistical properties everywhere so as to satisfy homogeneity. The energy cascade is forward from larger to smaller scales, and this corresponds to a positive value of ϵ .

In Section 5.1, we explicitly derive the generalized KHM equation seen in Eq. (5.8). The vector form of the KHM equation can be simplified to one dimension by integrating over the volume of the sphere of radius L , and applying Gauss’ theorem to the divergence operator to obtain a surface integral. The KHM equation in spherical average form is:

$$\frac{1}{4\pi} \int \langle \delta \mathbf{v} | \delta \mathbf{v} |^2 \rangle \cdot \hat{\mathbf{L}} d\Omega = -\frac{4}{3} \epsilon L \quad (9.1)$$

where $d\Omega \equiv \sin \theta d\theta d\phi$ is the element of solid angle, and θ and ϕ are spherical polar coordinates, and $\hat{\mathbf{L}}$ is the unit radial vector normal to the sphere (see Nie and Tanveer, 1999). The integral in Eq. (9.1) is carried out over all angles, and normalized by 4π and so calculates the scale to scale flux of energy through the sphere. The integral form of the KHM equation is more analogous to the formalism of shear studies than the usual divergence representation. Eq. (9.1) is still valid regardless of the anisotropy of the $\delta \mathbf{v}$. Assuming isotropy allows one to take $\langle \delta \mathbf{v} | \delta \mathbf{v} |^2 \rangle \cdot \hat{\mathbf{L}}$ out of the integral and obtain the Yaglom-like “4/3” Law seen in Eq. (5.9). Note that the integral of the third-order structure function is negative, linear in lag (L is always non-negative in spherical coordinates) and proportional to ϵ . The sense in which \mathbf{v} is a homogeneous field is critical to the derivation of the KHM equation. Remember that in our derivation of the KHM relation, we impose homogeneity conditions to obtain Eq. (5.6). Here, \mathbf{v} refers to a fluctuating velocity with a mean value that is zero everywhere.

Casciola et al. (2003) obtain a different third-moment equation for examining the role of velocity shear on turbulence in the absence of boundary effects. They set

$$\mathbf{v} = \mathbf{u} + (\mathbf{x} \cdot \nabla) \mathbf{U}. \quad (9.2)$$

Eq. (9.2) separates total velocity into a fluctuation component \mathbf{u} and varying mean part \mathbf{U} . Here the mean velocity is incompressible and restricted to a plane parallel shear flow that varies linearly with position. This case is referred to as a homogeneous shear flow (e.g., Hinze, 1975; Townsend, 1976; Davidson, 2004). As such, increments of \mathbf{U} for any lag are the same

no matter the position of the origin. Casciola et al. (2003) call \mathbf{v} in Eq. (9.2) a homogeneous field, but we do not since the average of \mathbf{v} varies with position. As such, the velocity used in the KHM equation given by Eq. (9.1) is not interchangeable with the one given by Eq. (9.2). The N-S equation can then be rewritten in a manner similar to the derivation of the KHM equation (see Section 5.1). The resulting equation has structure functions that are separated into parts showing the role of the background shear. Numerous experiments explore quasi-homogeneous shear flows. These include physical experiments (e.g., Champagne et al., 1970; Harris et al., 1977; Shen and Warhaft, 2000, 2002) and numerical simulations (e.g., Rogers and Moin, 1987; Lee et al., 1990; Kida and Tanaka, 1994; Pumir and Shraiman, 1995; Pumir, 1996; Schumacher and Eckhardt, 2000; Schumacher, 2004; Gualtieri et al., 2002; Casciola et al., 2003, 2007).

For a homogeneous velocity shear, and without loss of generality, we select a coordinate system so that the background flow magnitude varies linearly with position in a single direction across the flow. Taking the background velocity \mathbf{U} to be $\alpha y \hat{\mathbf{x}}$, the gradient is $\alpha \hat{\mathbf{y}}$ where α is the constant magnitude of speed change with position. The mean kinetic energy is then fixed, as its production and dissipation are balanced by its convection in the mean gradient direction (e.g., Champagne et al., 1970). Fluctuations on the background shear have velocities \mathbf{u} in all three directions and vary with position in all three directions. Casciola et al. (2003) derive an equation for this situation in terms of velocity increments and average over of a sphere of radius L . The resulting equation is referred to here as the Casciola-Gualtieri-Benzi-Piva (CGBP) equation. As with the expressions in Chapter 5, the viscous dissipation terms are neglected, meaning we are considering scale greater than the dissipative scales (i.e. the inertial and energy-containing ranges). The CGBP equation is given by:

$$S_3^{HD} + S_U^{HD} + S_P^{HD} = -\frac{4}{3}\epsilon L, \quad (9.3)$$

where

$$S_3^{HD} = \frac{1}{4\pi} \int \langle \delta \mathbf{u} |\delta \mathbf{u}|^2 \rangle \cdot \hat{\mathbf{L}} d\Omega, \quad (9.4)$$

$$S_U^{HD} = \frac{\alpha L}{4\pi} \int \sin^2 \theta \sin \phi \cos \phi \langle |\delta \mathbf{u}|^2 \rangle d\Omega, \quad (9.5)$$

and

$$S_P^{HD} = \frac{2\alpha}{4\pi L^2} \int \int \langle \delta u_x \delta u_y \rangle L^2 dL d\Omega. \quad (9.6)$$

Here superscript HD refers to the hydrodynamic case, $\delta \mathbf{u} \equiv \mathbf{u}(\mathbf{x} + \mathbf{L}) - \mathbf{u}(\mathbf{x})$ is the increment of \mathbf{u} along the lag and $|\delta \mathbf{u}|^2 \equiv \delta \mathbf{u} \cdot \delta \mathbf{u}$. Integrals are definite. In Eq. (9.4) and (9.5), the integrals are evaluated over all angles, and in Eq. (9.6), they are evaluated over the spherical volume with radius L . S_3^{HD} is the third-moment due to fluctuations alone and has the same form as the left hand side of Eq. (9.1). The terms S_U^{HD} and S_P^{HD} are proportional to the shear, and their values are reliant on the particulars of the fluctuation anisotropy in the (trace and off-diagonal xy element of the tensor) second-moment in the presence of shear. The term S_U^{HD} calculates the flux of energy through the sphere due to shear, while S_P^{HD} is the shear production of energy in the volume.

From Eq. (9.3), the sum of the individual terms on the left hand side is linear with L . Casciola et al. (2003) uses three dimensional (3D) incompressible hydrodynamic numerical simulations to examine a linearly varying plane shear flow with turbulent fluctuations (see also Gualtieri et al., 2002). From the simulation results, they find that the fluctuations

satisfy Eq. (9.3) well in the inertial and energy-containing ranges. The individual terms themselves are not, however, linear with L . The sum of transfer terms S_3^{HD} and S_U^{HD} is most significant in the inertial range, corresponding to the cascade of energy from larger to smaller scales. In the energy-containing scales both of these transfer terms become small at large L . The term S_P^{HD} can be insignificant at the smallest scales of the inertial range but becomes significant in the energy-containing range, and the dominant term at large L . It is referred to as the shear production term because it accounts for the energization of the cascade. The sum $S_3^{HD} + S_U^{HD}$ is comparable to S_P^{HD} at the scale $L_s = (\epsilon/|\alpha|^3)^{1/2}$ (Toschi et al., 1999).

The importance of the terms is affected by the magnitude of α . In the limit $\alpha = 0$, Eq. (9.3) reduces to the KHM equation given by Eq. (9.1). In the opposite limit of large $|\alpha|$, $|S_3^{HD}|$ can be small compared to either $|S_U^{HD}|$ or $|S_P^{HD}|$ or to both. We can consider $|\alpha|L \gg [\delta u(L)]_{rms}$, where $[\delta u(L)]_{rms}$ is the root-mean-squared value of $\delta \mathbf{u}$ averaged over all angles at fixed L . In this limit, if only one term proportional to α remains in Eq. (9.3), then the corresponding fluctuation correlation is independent of L . This situation is likely in the energy-containing range where $|S_U^{HD}| \ll |S_P^{HD}|$ when $L \gg L_s$. It might also occur within a large inertial range if $|S_U^{HD}| \gg |S_P^{HD}|$ and $[\delta u(L)]_{rms}/|\alpha| \ll L \ll L_s$.

The term S_3^{HD} can contribute significantly to the cascade even when the fluctuations are isotropic or nearly so. For smaller L , fluctuations tend to become more isotropic (e.g., Hinze, 1975) due in part to the effects of pressure strains that cancel relative to energy scale transfer, but not for energizing fluctuation velocity components of the same scale. As a result, S_3^{HD} is likely to be dominant at the small scale end of the inertial range, and isotropy can be used to estimate this term.

The shear term S_U^{HD} is sensitive to the fluctuation anisotropy and so is more difficult to estimate. In Eq. (9.5), the angular sensitivity comes from the projection of \mathbf{U} and $\delta \mathbf{U}$ onto the normal to the sphere $\hat{\mathbf{L}}$. The factor $\sin \theta \cos \phi$ is from the projection along the flow direction $\hat{\mathbf{x}}$ onto $\hat{\mathbf{L}}$, and the part $\sin \theta \sin \phi$ is from the projection along the flow gradient direction $\hat{\mathbf{y}}$ onto $\hat{\mathbf{L}}$. With this projection, an isotropic fluctuation energy dependence, or one where the fluctuation energy is isotropic in the xy plane, causes S_U^{HD} to vanish. This velocity shear in three dimensions is, however, associated with the nonlinear vortex stretching of eddies. It is known to yield a strain along two principal axes in the xy plane located half way between $\hat{\mathbf{x}}$ and $\hat{\mathbf{y}}$ (see Tennekes and Lumley, 1972; Kundu, 1990). Along one axis, the vorticity and energy of eddies are maximally amplified at the expense of these same quantities along the other axis. The principal axis on which eddies are amplified or not reverses with the sign of α . This contributes to fluctuation anisotropy and gives S_U^{HD} a negative value.

The strain associated with vortex stretching also causes the correlation between δu_x and δu_y to become nonzero. This is a condition indicative of anisotropic fluctuations. For $\alpha > 0$, this correlation is negative, and for $\alpha < 0$ this correlation is positive. As a result, S_P^{HD} will have a negative value. Lumley (1967) uses dimensional analysis to determine the value of the $\langle u_x u_y \rangle$ omni-directional spectrum in the inertial range of a homogeneous shear flow turbulence. He shows that the Kolmogorov energy cascade is associated with a $k^{-7/3}$ wave number spectrum for $\langle u_x u_y \rangle$. This indicates that the corresponding second-order structure function $\langle \delta u_x \delta u_y \rangle$ should vary as $L^{4/3}$.

To evaluate cases for a homogeneous velocity shear, we need to use the CGBP equation and not the KHM equation. To illustrate this, we replace $\delta \mathbf{v}$ in Eq. (9.1) with $\delta \mathbf{u} + \delta \mathbf{U}$ as

occurs when the velocity shear is not detrended. We then obtain:

$$S_3^{HD} + S_U^{HD} + S_{extra}^{HD} = -\frac{4}{3}\epsilon L, \quad (9.7)$$

where S_{extra}^{HD} is given by

$$S_{extra}^{HD} = \frac{1}{4\pi} \int \langle \delta \mathbf{u} |\delta \mathbf{U}|^2 + 2(\delta \mathbf{u} \cdot \delta \mathbf{U}) \times (\delta \mathbf{u} + \delta \mathbf{U}) \rangle \cdot \hat{\mathbf{L}} d\Omega, \quad (9.8)$$

and the cubic term involving δU vanishes upon integration. These extra terms do not equate with S_P^{HD} in Eq. (9.3), and thus the value of ϵ obtained from Eq. (9.7) differs from that in Eq. (9.3).

When solar wind velocity shear intervals of particular magnitude and sign are combined, the background velocity is not spatially invariant. This situation requires using the generalization of the CGBP equation to MHD. Moreover, we need a method for representing the shear-induced anisotropy to evaluate a term analogous to S_U^{HD} , which relies heavily on the process of vortex stretching discussed above.

9.1.2 Velocity Shear in MHD Third-Moments

As with Eq. 9.1, the 3D MHD version of the KHM equation (see Eq. (5.12)) in spherical average form is given by (Politano and Pouquet, 1998a,b):

$$\frac{1}{4\pi} \int \langle \delta \mathbf{Z}^\mp |\delta \mathbf{Z}^\pm|^2 \rangle \cdot \hat{\mathbf{L}} d\Omega = -\frac{4}{3}\epsilon^\pm L, \quad (9.9)$$

Again, this formulation of the equations better corresponds to the formalism of MHD shear analysis. The integral represents the flux of the energy from scale to scale through the sphere. Eq. (9.9) is general and valid for both isotropic and anisotropic turbulence, and for flow with zero average shear. Recall, the total energy cascade rate ϵ^T is given by $\epsilon^T = (\epsilon^+ + \epsilon^-)/2$ and should be equivalent to the mean dissipation rate of energy. In this chapter, we refer to Eq. (9.9) and any of the equations (see Chapter 5) derived from it as the PP equations.

Wan et al. (2009, 2010a,b) examine the resulting relations for MHD, when the velocity is separated into fluctuations and background linear shear flow, in both two and three dimensions. Wan et al. (2010b) particularly, focus on the 2D case where the velocity and magnetic field fluctuations are confined to a plane, and where there is no background magnetic field. In this 2D case, the fluid vorticity is non-linearly strained via electrodynamic vortex amplification associated with a differential Lorentz force (e.g., Spangler, 1999). They undertook incompressible 2D MHD numerical simulations with periodic boundaries of driven turbulence amidst a velocity shear. The prescribed time constant background velocity varies up and down spanwise, and sharply between two regions of nearly linear shear. In the linear shear region, the contributions from fluctuations and shear terms are evaluated and found to be in good agreement with theory. They show that the power spectrum of the fluctuations exhibits anisotropic behaviors at lower wave numbers. This is induced by the velocity shear which, judging from their Figure 10, is oriented approximately with principal axes that are streamwise and spanwise. Power is greater in the spanwise direction. Moreover, they consider the total velocity without any detrending for shear, and the 2D PP equations are found to give a good estimate of the cascade rate when the entire spatial domain is considered, so that the net shear vanishes.

In the solar wind, the effects of the velocity shear influence fluctuations with vectors and variations in all three spatial directions. Moreover, there is a background interplanetary magnetic field \mathbf{B}_0 that must also be considered, and here we assume that \mathbf{B}_0 is a constant. We set:

$$\mathbf{Z}^\pm = \mathbf{z}^\pm + \alpha y \hat{\mathbf{x}} \pm \mathbf{B}_0 / (\mu_0 \rho)^{1/2}, \quad (9.10)$$

where $\mathbf{z}^\pm = \mathbf{u} \pm \mathbf{b} / (\mu_0 \rho)^{1/2}$ is the fluctuating part, \mathbf{b} is the fluctuating magnetic field, and the mean velocity is as in Section 9.1.1. Wan et al. (2009) derive the shear expressions from the 3D MHD equations that we refer to here as the Wan-Servidio-Oughton-Matthaeus (WSOM) equations. The WSOM equations are obtained using the fluctuating and mean parts and integrating over a spherical volume. We recast the equations in a form analogous to Eq. (9.3) as:

$$S_3^{MHD,\pm} + S_U^{MHD,\pm} + S_P^{MHD,\pm} = -\frac{4}{3} \epsilon^\pm L, \quad (9.11)$$

where

$$S_3^{MHD,\pm} = \frac{1}{4\pi} \int \langle \delta \mathbf{z}^\mp | \delta \mathbf{z}^\pm |^2 \rangle \cdot \hat{\mathbf{L}} d\Omega, \quad (9.12)$$

$$S_U^{MHD,\pm} = \frac{\alpha L}{4\pi} \int \sin^2 \theta \sin \phi \cos \phi \times \langle |\delta \mathbf{z}^\pm|^2 \rangle d\Omega, \quad (9.13)$$

and

$$S_P^{MHD,\pm} = \frac{2\alpha}{4\pi L^2} \int \int \langle \delta z_x^\pm \delta z_y^\mp \rangle L^2 dr d\Omega. \quad (9.14)$$

Again, we neglect dissipative terms since the application is for the inertial. The derivation of these terms is entirely analogous to the derivation of the KHM equation presented in Section 5.1. The only differences are that the MHD equations written in terms of the Elsässer variables (see Eq. (3.8)) are used instead of the N-S equation and the Elsässer variables are rewritten in the form seen in Eq. (9.10). Remember that the MHD equations in terms of the Elsässer variables are of the same form as the N-S equation. The nature of the terms and limits with respect to α are in accord with the above discussion for hydrodynamics. Eq. (9.12) is the familiar MHD KHM equation, but only for the fluctuations with the large-scale background shear removed. Eq. (9.13) and (9.14) are again the shear transfer and shear production terms seen in the in the previous section for the hydrodynamic version. Summing over the \pm terms in Eq. (9.11)-(9.14) and then dividing by 2 gives the corresponding total energy cascade rate. The WSOM equations are valid for any form of anisotropic turbulence which arises in association with the velocity shear.

When $\sigma_c = 0$, all corresponding \pm terms in Eq. (9.12)-(9.14) are equal to each other ($S_3^{MHD,+} = S_3^{MHD,-}$, etc.) and contribute to the forward energy cascade so that each term is non-positive. Recall, when $\sigma_c = \pm 1$, non-linearity in the incompressible MHD equations vanishes and so should all terms. For intermediate σ_c , there is no known constraint on the sign of the terms. The expectation is that for σ_c not near ± 1 , the cascade will be forward and all terms in Eq. (9.12)-(9.14) will be non-positive.

9.1.3 Application of Velocity Shear Formalism to the Solar Wind

Eq. (9.11) provides what is needed to examine simulation results from incompressible 3D MHD quasi-homogeneous shear flow. Yet, the solar wind is a flow where the ratio of the plasma to magnetic pressure is typically below unity, and thus is far from an incompressible medium. Here, \mathbf{B}_0 and its attendant anisotropy with respect to direction become vitally important. Turbulent velocity and magnetic field fluctuations in the presence of \mathbf{B}_0 nonlinearly

interact most strongly across \mathbf{B}_0 (e.g., Shebalin et al., 1983; Matthaeus et al., 1996b). With highly oblique wave vectors, the fluctuations are found to approach a nearly incompressible (e.g., Zank and Matthaeus, 1993) or weakly compressive (e.g., Bhattacharjee et al., 1998) state. For this case, the incompressible MHD equations contain the dominant non-linear effects needed to describe the turbulent fluctuations. Observations show that interplanetary fluctuations are relatively non-compressive in the inertial range. Moreover, lags across \mathbf{B}_0 are readily available at 1 AU. Recall from Section 6.2 that MacBride et al. (2008) shows from Eq. (5.34) and (5.35), which derive from Eq. (9.9), that the cross-field cascade in the solar wind is indeed stronger than along \mathbf{B}_0 . The amount of anisotropy is modest enough that the isotropic approximation is still useful in cascade rate determination (see also Stawarz et al., 2009). We, therefore, ignore anisotropy arising from \mathbf{B}_0 (the hybrid formalism) in this chapter, in order to focus on velocity shear.

In order to proceed further with solar wind data analyses, we consider approximations for the individual terms in Eq. (9.11) since single spacecraft analyses lack direct measurement of fluctuation anisotropy with respect to the velocity shear. Again, because we combine intervals with a particular varying background velocity in this chapter, we must use the WSOM equations to obtain ϵ and not the PP equations, for the same reasons discussed earlier concerning the hydrodynamics case. In Section 9.2, we show that the PP equations, in particular the isotropic form seen in Eq. (5.17), yield incorrect results for such cases.

In Eq. (9.11), the terms $S_U^{MHD,\pm}$ require anisotropy, and thus we treat first the estimation of these terms. The $S_U^{MHD,\pm}$ terms from Eq. (9.13) involve an integral over the fluctuation energy that vanishes for isotropic fluctuations in the xy plane. With the assumed form of the velocity shear and with fluctuations varying in all three spatial dimensions, the most straightforward expectation for fluctuation energy anisotropy induced by the shear is the alignment of this anisotropy with the mean strain principal axes $(\hat{\mathbf{y}} \pm \hat{\mathbf{x}})/2^{1/2}$. This is due to the aforementioned mechanism of vortex stretching. We can evaluate the integral in Eq. (9.13) by assuming that the fluctuation energy $|\delta\mathbf{z}^\pm(L, \phi, \theta)|^2$ varies with θ and ϕ in the simplest possible manner: θ and ϕ vary according to an ellipsoidal model with coefficients independent of L , so that the anisotropy is constant with L . This neglects the expected attenuation of anisotropy for smaller L in the inertial range. In the solar wind, however, the inertial range is moderately short, and moreover the estimates for ϵ are based on averages taken over the observed linear range of L . Thereby, this approach can be viewed as the estimate for the average anisotropy over the extent of this range. In this approach, the values of $S_U^{MHD,\pm}$ are varied and summed with the other terms for which more direct estimates are available. This yields a total dissipation rate that is at least consistent with the observed proton heating rate.

We replace $|\delta\mathbf{z}^\pm(L, \phi, \theta)|^2$ with $f(\phi, \theta)|\delta\mathbf{z}^\pm(L)|^2$ where:

$$f(\phi, \theta) = \frac{3}{1/a^2 + 1/b^2 + 1/c^2} \times \left[\frac{\sin^2 \theta (1/2 + \cos \phi \sin \phi)}{a^2} + \frac{\sin^2 \theta (1/2 - \cos \phi \sin \phi)}{b^2} + \frac{\cos^2 \theta}{c^2} \right] \quad (9.15)$$

is the ellipsoid of anisotropy with principal axes radii a and b in the xy plane and the out of plane axis with radius c . (Note that a larger radius along its axis corresponds to smaller amplitude along that axis for fixed radius L .) The value of f is normalized so that 4π results when f is integrated over all solid angle. The mean values $\langle |\delta\mathbf{z}^\pm(L)|^2 \rangle$ over all angles can be related to the values along the streamwise lag $\langle |\delta\mathbf{z}^\pm(L, 0, 90^\circ)|^2 \rangle$. The values along

the streamwise lag are hereafter denoted by $\langle |\delta \mathbf{z}^\pm(L)|_s^2 \rangle$, that in application are replaced by measured values from solar wind data. Dividing through with the value of f in the x direction, we obtain:

$$\langle |\delta \mathbf{z}^\pm(L)|^2 \rangle = A_s \langle |\delta \mathbf{z}^\pm(L)|_s^2 \rangle \quad (9.16)$$

where the factor $A_s \equiv 1/f(0, 90^\circ)$ is given by:

$$A_s = \left[\frac{3}{1/a^2 + 1/b^2 + 1/c^2} \right]^{-1} \times \left[\frac{1}{2} \left(\frac{1}{a^2} + \frac{1}{b^2} \right) \right]^{-1} \quad (9.17)$$

or more compactly by

$$A_s = \frac{2}{3} \frac{c^2(a^2 + b^2) + a^2b^2}{c^2(a^2 + b^2)}. \quad (9.18)$$

With these assumptions, the resulting form for Eq. (9.13) is:

$$S_U^{MHD,\pm} = -\frac{2|\alpha|L}{15} \frac{|b^2 - a^2|}{a^2 + b^2} \langle |\delta \mathbf{z}^\pm(L)|_s^2 \rangle \quad (9.19)$$

which is independent of c by virtue of the cancellation of factors in Eq. (9.15) and (9.17). We assume that the forward energy cascade is enhanced by both $S_U^{MHD,+}$ and $S_U^{MHD,-}$ when they are nonzero because the data used in Section 9.2 combines intervals without regard for σ_c . The average $|\sigma_c|$ is not so large as to significantly alter the inertial range cascade (Smith et al., 2009; Stawarz et al., 2010). With this assumption, we take absolute values in Eq. (9.19), so that $S_U^{MHD,\pm}$ is always non-positive. This means that we can also take $b^2 \geq a^2$ without loss of generality and not be concerned with the sign of α when evaluating Eq. (9.19). Note that isotropy in the xy plane $a^2 = b^2$ gives $S_U^{MHD,\pm} = 0$. Moreover, the choice of principal axes in the xy plane in Eq. (9.15) maximizes $|S_U^{MHD,\pm}|$ for fixed xy anisotropy b^2/a^2 , whereas if the axes are along $\hat{\mathbf{x}}$ and $\hat{\mathbf{y}}$, $S_U^{MHD,\pm}$ are zero. Alternatively, for fixed values of $S_U^{MHD,\pm}$, b^2/a^2 is minimized because a different orientation for the principal axes in the xy plane requires larger b^2/a^2 to obtain the same values of $S_U^{MHD,\pm}$.

The model Eq. (9.19) is essential in the analyses below. The values of a and b are to be taken as free parameters to vary anisotropy in the xy plane and examine the resulting values of ϵ^\pm to compare with independently proton heating rates from Eq (3.25). We neglect the effect of σ_c in the present analysis and use the same parameters a , b , and c for the Elsässer amplitudes $|\mathbf{z}^+|$ and $|\mathbf{z}^-|$. Taking a case from Section 9.2, one sets $a = 1$, and $b = 2$, then $S_U^{MHD,\pm} = -0.08|\alpha|L\langle |\delta \mathbf{z}^\pm|^2 \rangle$ with a proportionality constant of 0.08. The actual range of the proportionality constant is quite limited. The largest magnitude is $2/15$ and occurs when $b^2/a^2 \rightarrow \infty$. As a result, the magnitudes of $S_U^{MHD,\pm}$ are sensitive to small departures from isotropy but insensitive to large departures.

Remaining terms on the left hand side of Eq. (9.11) give nonzero values even for isotropic fluctuations, but the underlying fluctuations will be anisotropic for finite α . To lowest order, we expect the anisotropy of these terms to align with the mean strain principal axes. We approximate the anisotropy as one equivalent to the fluctuation energy and separate integrands as quantities whose angular dependence is given by Eq. (9.15) and an amplitude dependence only on L . The integration over all angles of $f(\phi, \theta)$ only results in the cancellation of the 4π factor in Eq. (9.12) and (9.14). The mean value of the ratio between the actual amplitude dependence and the dependence measured in the streamwise direction is

proportional to A_s . This introduces a dependence upon the free parameter c , as well as, a and b . From Eq. (9.12), the terms dependent only on fluctuations are estimated by:

$$S_3^{MHD,\pm} = A_s^{3/2} \langle [\delta z_x^\mp |\delta \mathbf{z}^\pm|^2]_s \rangle \quad (9.20)$$

which retain the signs of the third-order structure functions along the streamwise lag. The shear production terms $S_P^{MHD,\pm}$ involve an evaluation over the volume. With this approach, we use the streamwise values of $\langle \delta z_x^\pm \delta z_y^\mp \rangle$ so that:

$$S_P^{MHD,\pm} = \frac{2\alpha A_s}{L^2} \int_0^L \langle [\delta z_x^\pm \delta z_y^\mp]_s \rangle L^2 dL \quad (9.21)$$

With increasing L , the values of $S_P^{MHD,\pm}$ accumulate and generally increase in magnitude. Notice that absolute values are not introduced into Eq. (9.21) because the signs and magnitudes of the integrands are obtained with measurements. Their relation with the sign of α gives a consistency check on the assumption that velocity shear driving of turbulence is preeminent.

The dependence of A_s on c can vary the magnitude of the estimates for $S_3^{MHD,\pm}$ and $S_P^{MHD,\pm}$. For the typical case in Section 9.2, $a = c = 1$ and $b = 2$, we find from Eq. (9.18) that $A_s = 1.2$ which differs little from complete isotropy where $a = b = c = 1$ and $A_s = 1$. In the limit that $c^2/a^2 \rightarrow \infty$, which corresponds to fluctuation wave vectors confined increasingly to the xy plane, $A_s = 2/3$. In the opposite limit that $c^2/a^2 \rightarrow 0$ and b^2/a^2 is finite, $A_s \rightarrow \infty$, so that large anisotropy in the z -direction can greatly affect the values of $S_3^{MHD,\pm}$ and $S_P^{MHD,\pm}$.

The final expressions used in the present analyses change some of the notation and are consistent with previous chapters of this thesis. Again, the signs of \mathbf{Z}^\pm and \mathbf{z}^\pm are redefined with respect to the background magnetic field so as to correspond to propagating Alfvén waves traveling inward (denoted by superscript ‘in’) or outward (denoted by ‘out’) from the Sun. The background velocity is mainly in the heliocentric radial direction $\hat{\mathbf{R}}$ away from the Sun. In Cartesian coordinates, this corresponds to the $\hat{\mathbf{x}}$ direction used above. We take $\hat{\mathbf{y}}$ to be in the direction of the Earth’s revolution about the Sun which is the $\hat{\mathbf{T}}$ direction of the RTN coordinate system. Again, we take $L = -V_{SW}\tau$ for the same reasons discussed in Chapter 5. We hereafter also drop the subscript denoting streamwise measurements, and the superscript MHD since that is the only case we consider in the remainder of this chapter. Eq. (9.11) with all approximations included is rewritten as:

$$D_3^{out/in} + D_U^{out/in} + D_P^{out/in} = \frac{4}{3} \epsilon_{SH}^{out/in} V_{SW} \tau \quad (9.22)$$

where the functions of $V_{SW}\tau$ are:

$$D_3^{out/in} = A_s^{3/2} \langle \delta z_R^{in/out} |\delta \mathbf{z}^{out/in}|^2 \rangle \quad (9.23)$$

$$D_U^{out/in} = \frac{2|\alpha| V_{SW} \tau}{15} \frac{|b^2 - a^2|}{a^2 + b^2} \langle |\delta \mathbf{z}^{out/in}|^2 \rangle \quad (9.24)$$

$$D_P^{out/in} = -\frac{2\alpha A_s V_{SW}}{\tau^2} \int_0^\tau \langle \delta z_R^{out/in} \delta z_T^{in/out} \rangle \tau^2 d\tau. \quad (9.25)$$

We also define the sum of structure functions in Eq. (9.22) by:

$$D_{3,SH}^{out/in} \equiv D_3^{out/in} + D_U^{out/in} + D_P^{out/in}, \quad (9.26)$$

and total structure functions by:

$$D_3^T \equiv (D_3^{out} + D_3^{in})/2 \quad (9.27)$$

$$D_U^T \equiv (D_U^{out} + D_U^{in})/2 \quad (9.28)$$

$$D_P^T \equiv (D_P^{out} + D_P^{in})/2, \quad (9.29)$$

$$D_{3,SH}^T \equiv (D_{3,SH}^{out} + D_{3,SH}^{in})/2. \quad (9.30)$$

The total dissipation rate is given by:

$$\epsilon_{SH}^T = (\epsilon_{SH}^{out} + \epsilon_{SH}^{in})/2. \quad (9.31)$$

The subscript ‘SH’ denotes that the expressions correspond to the WSOM theory for the case of homogeneous shear, and use detrended velocities to evaluate fluctuations and their moments. Recall the concept of detrending from Chapter 6. As with the expressions in Chapter 5, the sign of the structure functions as a function of τ for a cascade from large to small scales is positive. For the purposes of this chapter, we retain the superscript “T” when referring to total quantities.

For comparison purposes, we also consider the isotropic expression which does not consider shear given by Eq. (5.17). In this chapter, we denote this expression with the subscript ‘NOSH’ for ‘no shear’.

9.2 Shear Analyses

In this study, we again use the same 10 years of ACE magnetic field and plasma data used in the analyses from Chapters 7 and 8. This data spans from 1998 until the end of 2007. A wide range of solar wind conditions are encompassed in this data including solar minimum and solar maximum conditions, as well as, intervals of increasing and decreasing solar wind speed associated with velocity shears.

The analyses of MacBride et al. (2005, 2008) and Stawarz et al. (2009) demonstrate that the MHD third-moment expressions described in Chapter 5 can provide scale independent energy cascade rates within the inertial range at 1 AU. The calculated rates match up well with inferred proton heating rates in the solar wind. In this study, we use the WSOM equations and the modified third-moment shear expressions $D_{3,SH}^{out/in}(V_{SW}\tau)$ described in Section 9.1 to analyze solar wind observations with regard to velocity shear.

We consider two subinterval lengths 6 and 12 hrs. Additionally, as with the previously described analyses, we remove intervals containing CMEs and other transients based on a list of known events. We compute values of both ϵ_{SH}^T and ϵ_{NOSH}^T based on the 6 and 12 hr intervals. The method for computing ϵ_{NOSH}^T is the same as that used by MacBride et al. (2008) and Stawarz et al. (2009, 2010) (see Chapters 6–8), while the method used to compute ϵ_{SH}^T is a slightly modified version of the same procedure.

Moments computed from 12 hr intervals are found to give results consistent with those from 6 hr intervals. Thereby, we present only the results for 12 hr intervals, which is the same interval size we use in the analyses of Chapters 7 and 8.

The shear analyses assume a uniform shear, and hence we need to obtain the linear trend in each data interval. We perform a linear fit of the radial velocity data in each 12 hr interval and subtract the linear trend from the raw radial velocity dataset. This gives a linear trend characterizing the shear, and a detrended set of data characterizing velocity fluctuations.

Recall the RTN coordinate system described at the end of Section 2.4. In the solar wind, we take the directions $\hat{\mathbf{R}}$ (radially outward from the Sun) and $\hat{\mathbf{T}}$ (in the direction of the Sun's rotation) to correspond to the \mathbf{x} and \mathbf{y} directions in the theory. In other words, we assume the gradient to be in the $(\hat{\mathbf{R}}, \hat{\mathbf{T}})$ plane. This neglects any latitudinal component to the shear and is the natural starting point for a single-spacecraft analysis. We return to this assumption in Section 9.3. The background solar wind velocity is mainly in the $\hat{\mathbf{R}}$ direction, but varies with time at the spacecraft and has a gradient in the $\hat{\mathbf{T}}$ direction due to the rotation with the Sun of sources of different solar wind speeds. The wind speed is constant on the local Parker spiral, so that $\alpha = \partial V_{SW}/\partial T$ is given by:

$$\alpha = -\frac{\Delta V_{SW}}{\Omega R t_{interv}} = -5.9 \times 10^{-8} \Delta V_{SW} [\text{s}^{-1}] \quad (9.32)$$

where ΔV_{SW} is the change in speed based on the linear trend for the whole 12 hr interval and is in units of km/s, $R = 1 \text{ AU}$ is the heliocentric distance, $\Omega = (2\pi/27) \text{ days}^{-1}$ is the synodic angular frequency of solar rotation taken to be the value near the solar equator, and $t_{interv} = 0.5 \text{ days}$ is used. Note that $\Omega R t_{interv}$ corresponds to a distance traversed along a circular arc for time t_{interv} owing to solar rotation.

Fluctuation velocity and magnetic field data, and the proton density, which is averaged for the 12 hr interval, are used to compute $\delta z_R^{in/out} |\delta \mathbf{z}^{out/in}|^2$, $|\delta \mathbf{z}^{out/in}|^2$, and $\delta z_R^{out/in} \delta z_T^{in/out}$ as a function of time lag for each 12 hr interval. These quantities are then interpolated to a grid of spatial lag based on the average V_{SW} for the interval as described in Section 6.2. The above third-moments, along with α and the chosen free parameters a , b and c , are then used to calculate $D_3^{out/in}$, $D_U^{out/in}$, $D_P^{out/in}$ and $D_{3,SH}^{out/in}$ as a function of lag given by Equations (9.23)-(9.26), as well as the total quantities D_3^T , D_U^T , D_P^T and $D_{3,SH}^T$ given by Equations (9.27)-(9.30).

When computing the isotropic MHD expressions, which do not include shear, we compute $\delta Z_R^{in/out} |\delta \mathbf{Z}^{out/in}|^2$ as a function of lag for each 12 hr interval, which gives the function $D_{3,NOSH}^{out/in}$. Values are also interpolated onto a common spatial grid based on the average V_{SW} for the 12 hr interval in order to compute ensemble averages. In addition, the expected proton heating rate ϵ_{heat} given by Eq. (3.25) is computed for each 12 hr interval for comparison with computed cascade rates.

Averaging the 12 hr interval quantities, we perform two analyses. First, in Section 9.2.1, we subset intervals into bins of velocity shear and examine the predictions of the WSOM equations and those of shear-driven turbulence. Second, in Section 9.2.2, we bin according to $V_{SW} T_P$ and reanalyze the heating results seen in Figure 7.3 using the WSOM equations.

9.2.1 Sorting Results by Local Velocity Shear

In order to apply Eq. (9.22)-(9.31), intervals are sorted into bins according to ΔV_{SW} in a specified range. The ΔV_{SW} bins that we use range from -100 to $+100 \text{ km/s}$ with equal widths of 25 km/s . Note that negative values of ΔV_{SW} correspond to regions where faster wind is followed by slower wind so that these are regions of rarefaction. Positive values of ΔV_{SW} correspond to regions where a slower wind is being overtaken by a faster wind, and thus these are regions of compression.

The present analysis bins compression and rarefaction intervals for equivalent levels of shear without regard for the duration of the event. With equivalent levels of shear, the theory has cascade rates that are the same in the rarefaction and compression intervals. Important

differences in these intervals when analyzed, however, are shown below. This might arise due to assumptions in our analysis such as the neglect of latitudinal gradients. Our theory, in general, is symmetric regardless of whether the shear is positive or negative. Results are shown without additional comment on these assumptions. Section 9.3 then discusses how the assumptions can impact the results.

Averages over the 12 hr intervals having ΔV_{SW} within the appropriate bins are performed to find the average value of $D_{3,SH}^T$ as a function of lag. The uncertainty weighted average of $3D_{3,SH}^T/(4L)$ is calculated for each spatial lag L which is less than the corresponding time lag τ of 8000 s based on a reference speed of 400 km/s. We average over the range of lags in which $D_{3,SH}^T$ varies almost linearly. Recall that the linear scaling of $D_{3,SH}^T$ is required by the theory. This constraint is shown further below to be important when $\Delta V_{SW} > 0$. This calculation gives the average ϵ_{SH}^T for each bin. A similar approach is used to obtain ϵ_{NOSH}^T .

We use the method described in Chapter 7 to compute uncertainties. Take X to be some quantity, e.g., $D_3^{out/in}$ at a particular spatial lag, which is to be averaged over the 12 hr intervals analyzed. Each value of X computed from an individual 12 hr interval is taken to be a statistically independent estimate with no intrinsic uncertainty because 12 hrs is greater than the correlation length and the propagation of measurement error is likely the same for all samples. As such, estimates from the 12 hr intervals follow a Gaussian distribution, and Gaussian statistics can be used to compute the mean, standard deviation, and error-of-the-mean for the ensemble averaged quantities. From there, the uncertainty is propagated through further calculations using standard methods.

The average value of ϵ_{heat} is also obtained from all 12 hr intervals per ΔV_{SW} bin. The expression for ϵ_{heat} in Eq. (3.25) is determined by an analysis based on the spherically symmetric proton equation of state. Hence, the heating rate is the average over the spherical polar angles and so does not correspond to rates in separate rarefaction and compression regions. Based on the work of Burlaga and Ogilvie (1973), who find that the net heating in compressions over rarefactions is $\sim 15\%$ on average, we expect that the $\Delta V_{SW} > 0$ bins have somewhat more heating than predicted by ϵ_{heat} , while $\Delta V_{SW} < 0$ bins have less. The amount of relative deviation is, however, likely to be less than approximately 5%. Thus, ϵ_{heat} is deemed to be a sufficiently good guide to the required dissipation rate from the turbulence in the present analyses. Uncertainty for the average value of ϵ_{heat} is determined as above.

Figure 9.1 plots the value of ϵ_{SH}^T , ϵ_{NOSH}^T , and ϵ_{heat} as a function of ΔV_{SW} (see also Table 9.1). Here the value of ϵ_{SH}^T is obtained by assuming an anisotropy of 2 : 1, corresponding to the values $a = c = 1$ and $b = 2$ in Equations (9.18) and (9.24). Errors-of-the-mean are plotted but are typically smaller than the symbols used, and horizontal bars indicate the range of ΔV_{SW} analyzed for each data point. Except for ϵ_{NOSH}^T , the plotted rates increase with $|\Delta V_{SW}|$, as is expected of a turbulent energy cascade driven by velocity shear. The values of ϵ_{SH}^T and ϵ_{heat} approximately follow each other, and ϵ_{SH}^T is always above zero, consistent with a forward cascade dissipating and heating the plasma. The cascade rate ignoring shear ϵ_{NOSH}^T appears to be dominated by the sign of the shear and has no correspondence with ϵ_{heat} . The absolute value of ϵ_{NOSH}^T is smaller for the bin with $\Delta V_{SW} < 0$ than the one for the same but positive signed ΔV_{SW} bin.

The values of ϵ_{SH}^T for the bins closest to zero, i.e. -25 to 0 km/s and 0 to $+25$ km/s, in Figure 9.1 are anomalously small compared to ϵ_{heat} and not a good match. The poor match probably occurs because cases of weak shear are less likely to be characterized well by a linear trend of velocity shear. In these cases, the intervals tend to be located between intervals of positive and negative shear and may be at local maximum or minimum V_{SW} . Thus, we

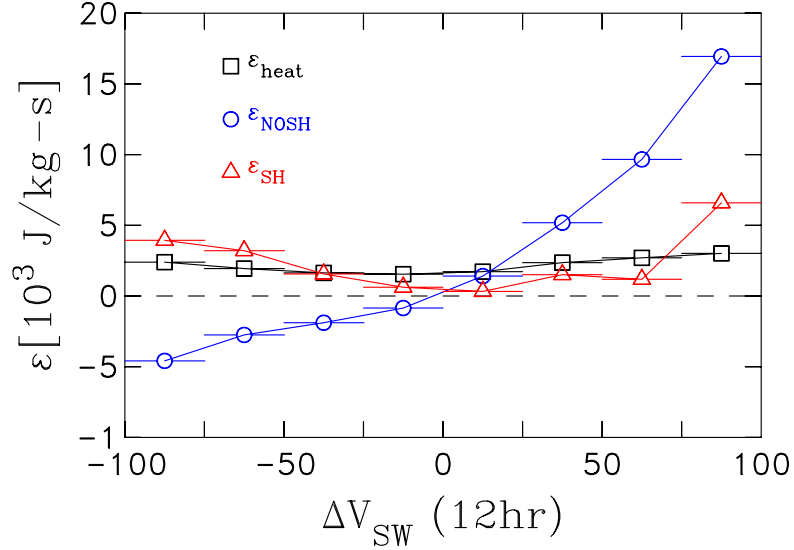


Figure 9.1: Cascade rates versus ΔV_{SW} for 12 hr intervals and comparison with the average proton heating rate. The no-shear analysis is dominated by the signal from the background shear. The shear analysis yields acceptable results for $\Delta V_{SW} < -25$ km/s. Error bars are smaller than symbols. Table 9.1 gives plotted data values, errors, and sample numbers. Figure reproduced from Stawarz et al. (2011).

focus on the outer lying bins, where the shear is more significant and better characterized.

The farther outlying bins on the left and negative side of $\Delta V_{SW} = -25$ km/s have ϵ_{SH}^T that matches or exceeds ϵ_{heat} . These can provide sufficient energization for the plasma including electron and alpha heating, as well as proton heating. Taking electron heating to be about 50% of proton heating provides a good upper bound to the expected total plasma heating (Vasquez et al., 2007; Stawarz et al., 2009), and the values obtained for ϵ_{SH}^T can satisfy these bounds. On the other hand, farther outlying bins on the right and positive side of $\Delta V_{SW} = +25$ km/s have a more irregular trend up and down with respect to ϵ_{heat} and are less in agreement with ϵ_{heat} than is the case on the opposite side. This is not a trend to be

Table 9.1: Rates for Figure 9.1. Table reproduced from Stawarz et al. (2011).

ΔV_{SW} Range [km/s]	# Samples	ϵ_{SH}^T	ϵ_{NOSH}^T	ϵ_{heat}^T
[$\times 10^3$ Joules/kg-s]				
$-100 < \Delta V_{SW} < -75$	159	3.94 ± 0.11	-4.59 ± 0.09	2.39 ± 0.14
$-75 < \Delta V_{SW} < -50$	404	3.20 ± 0.05	-2.75 ± 0.04	1.94 ± 0.07
$-50 < \Delta V_{SW} < -25$	915	1.56 ± 0.03	-1.89 ± 0.03	1.63 ± 0.05
$-25 < \Delta V_{SW} < 0$	1334	0.62 ± 0.06	-0.85 ± 0.02	1.54 ± 0.04
$0 < \Delta V_{SW} < +25$	782	0.32 ± 0.11	1.41 ± 0.04	1.72 ± 0.05
$+25 < \Delta V_{SW} < +50$	410	1.51 ± 0.29	5.18 ± 0.09	2.36 ± 0.09
$+50 < \Delta V_{SW} < +75$	204	1.18 ± 0.34	9.66 ± 0.12	2.70 ± 0.13
$+75 < \Delta V_{SW} < +100$	136	6.59 ± 0.38	16.94 ± 0.26	3.02 ± 0.17

expected for an ensemble of true homogeneous shear-driven turbulence, where the sign of α or ΔV_{SW} does not affect the cascade rate. Section 9.3 discusses how compressional regions in the solar wind can deviate from the theory and contribute to the observed trends.

The analysis based on the PP equations giving ϵ_{NOSH}^T , clearly does not provide the cascade rates for cases with persistent shear. This is explained in Section 9.1, and these results are in agreement with conclusions reached there. The signal from the velocity shear itself contaminates the measurements to such an extent that the sign of the calculated ϵ_{NOSH}^T is the same as that of ΔV_{SW} .

We now consider the relative contribution of fluctuation-only and shear-dependent terms to the cascade rates. The theory requires $D_{3,SH}^T$ to vary linearly. The individual terms that sum to $D_{3,SH}^T$ can vary differently from a linear scaling. Figure 9.2 plots the values of D_3^T , D_U^T , D_P^T , and the sum of these three terms $D_{3,SH}^T$ as a function of lag for the ΔV_{SW} bin from -75 to -50 km/s. The value of $D_{3,NOSH}^T$ as a function of lag within this bin is also plotted for completeness, but we do not discuss this quantity further. Figure 9.3 plots the same but for the ΔV_{SW} bin from $+50$ to $+75$ km/s. The trends in each figure are typical of the bins with the same sign of ΔV_{SW} .

In Figure 9.2, all quantities vary approximately linearly with lag over the plotted range. By far, the largest contribution to $D_{3,SH}^T$ comes from the detrended third-moment term D_3^T . The values of D_U^T and D_P^T are smaller with D_U^T larger than D_P^T . Though small, D_P^T has a value that is more than one standard deviation from zero. The relative error for D_P^T is less than 1%, and the error bars for D_P^T in Figure 9.2 are smaller than the plotted symbol size. Its magnitude and sign can be compared to the predictions of shear-driven turbulence. Here, D_P^T has a positive sign as expected of the generation of energy from the shear. Its relatively small value is consistent with the plotted range of lags being within the inertial range. Since D_P^T according to Eq. 9.25 and 9.30 depends on $\langle \delta z_R^{out/in}(\tau) \delta z_T^{in/out}(\tau) \rangle$, which we measure to be nonzero at all lag times τ , fluctuations are anisotropic, and this too is consistent with shear-driven turbulence.

In Figure 9.3, where $\Delta V_{SW} > 0$, we find complicated behavior which is outside the expectations for homogeneous shear-driven turbulence. In Section 9.3, we discuss how compressive effects can contribute to this behavior. The term $D_{3,SH}^T$ varies linearly with lag starting from near zero out to about 2000 s, which is in accord with theory, but then decreases and follows a non-monotonic course. The linear range is only a quarter of the plotted range and smaller than the expected inertial range. The computed value of ϵ_{SH}^T is taken only from this range. The term D_3^T changes from positive values to negative ones beyond 2000 s. Both $D_{3,SH}^T$ and D_3^T have values with much larger uncertainty than corresponding points in Figure 9.2. The term D_U^T varies nearly monotonically over the whole range which corresponds to increasing fluctuation energy with increasing lag. It even exceeds D_3^T beyond lags of 1000 s. The term D_P^T remains close to zero in the plotted range. The irregular behavior of $D_{3,SH}^T$ with lag is found for all bins with $\Delta V_{SW} > 0$ and its relatively large uncertainty undoubtedly contributes to the scatter in ϵ_{SH}^T about ϵ_{heat} .

In the theory, we expect symmetrical results for rarefaction and compression intervals. In Figure 9.2, we find that the plotted quantities for rarefactions are well-behaved with consistent behavior throughout the entire range and measurement uncertainties are relatively small. By contrast, Figure 9.3 for compressions, shows that the plotted quantities do not follow a consistent trend and do not conform to expectations of linear scaling. Therefore, we fail to find the expected symmetry and conclude based on the observed nonlinear scaling and larger uncertainties that the analysis provides a poorer assessment of compression regions.

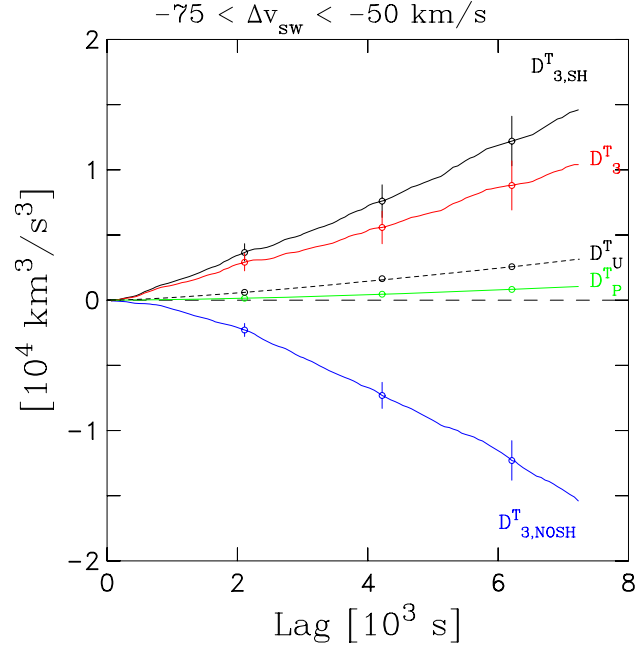


Figure 9.2: Structure function terms versus lag for the second leftmost speed bin in Figure 9.1. The plot shows the contribution from fluctuation and shear terms to the total sum where the sum for the shear analysis is $D_{3,SH}^T$ (solid black line), fluctuation term is D_3^T (solid red line), shear transfer term is D_U^T (short dashed black line), shear production term is D_P^T (solid green line), and the no-shear analysis is $D_{3,NOSH}^T$ (solid blue line). Error bars are included with data points. Figure reproduced from Stawarz et al. (2011).

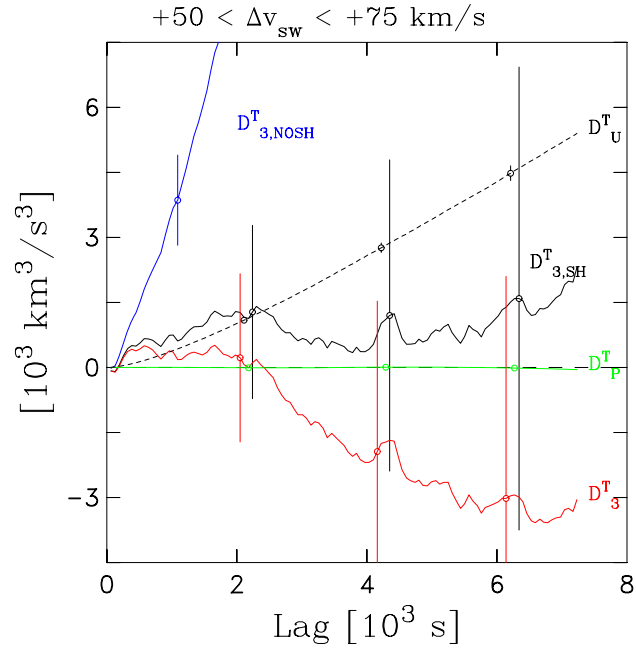


Figure 9.3: Structure function terms versus lag for the second rightmost speed bin in Figure 9.1. Plot quantities are rendered as in Figure 9.2. Figure reproduced from Stawarz et al. (2011).

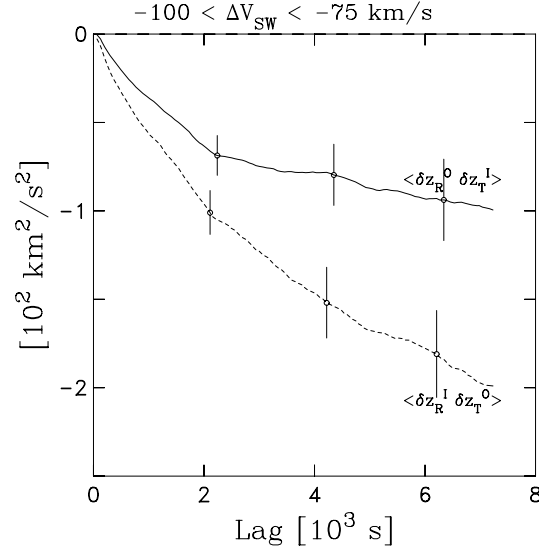


Figure 9.4: Second-order structure functions versus lag for the leftmost bin in Figure 9.1. The values are intrinsic to shear production. Negative values are consistent with shear-driven turbulence. Table 9.2 gives fit parameters. In this plot, the superscripts “I” and “O” correspond to the superscripts “in” and “out” for inward and outward propagating fluctuations. Figure reproduced from Stawarz et al. (2011).

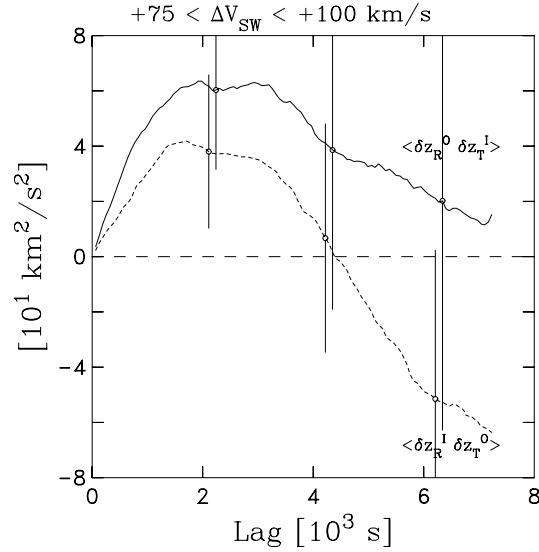


Figure 9.5: Second-order structure functions versus lag for the rightmost bin in Figure 9.1. Positive values are consistent with shear-driven turbulence. Table 9.2 gives fit parameters. In this plot, the superscripts “I” and “O” correspond to the superscripts “in” and “out” for inward and outward propagating fluctuations. Figure reproduced from Stawarz et al. (2011).

Table 9.2: Fits for Figures 9.4 and 9.5. Table reproduced from Stawarz et al. (2011).

ΔV_{SW} Range [km/s]	Quantity	Fit	Lag Range [s]
$-100 < \Delta V_{SW} < -75$	$\langle \delta z_R^{in} \delta z_T^{out} \rangle$	$(-0.339^{+0.004}_{-0.004})\tau^{0.73 \pm 0.01}$	$0 < \tau < 7232$
$-100 < \Delta V_{SW} < -75$	$\langle \delta z_R^{out} \delta z_T^{in} \rangle$	$(-0.479^{+0.009}_{-0.009})\tau^{0.62 \pm 0.02}$	$0 < \tau < 7232$
$+75 < \Delta V_{SW} < +100$	$\langle \delta z_R^{in} \delta z_T^{out} \rangle$	$(0.072^{+0.007}_{-0.006})\tau^{0.86 \pm 0.10}$	$0 < \tau < 2048$
$+75 < \Delta V_{SW} < +100$	$\langle \delta z_R^{out} \delta z_T^{in} \rangle$	$(0.158^{+0.008}_{-0.008})\tau^{0.82 \pm 0.06}$	$0 < \tau < 2048$

Because the terms $D_P^{out/in}$ provide the most direct measurement of the effects of the shear-driven turbulence, we examine separately the underlying fluctuation structure functions. These are the second-order structure functions given by $\langle \delta z_R^{out/in} \delta z_T^{in/out} \rangle$. In the theory, the sign of $\langle \delta z_R^{out/in} \delta z_T^{in/out} \rangle$ matches that needed to produce energy for the cascade. In addition, the absolute value of $\langle \delta z_R^{out/in} \delta z_T^{in/out} \rangle$ increases with increasing scale since production is strongest at the large, energy-containing scales. Figure 9.4 plots $\langle \delta z_R^{out} \delta z_T^{in} \rangle$ and $\langle \delta z_R^{in} \delta z_T^{out} \rangle$ as a function of lag for the ΔV_{SW} bin from -100 to -75 km/s. Figure 9.5 plots the same but for the ΔV_{SW} bin from $+75$ to $+100$ km/s.

In Figure 9.4, both $\langle \delta z_R^{out} \delta z_T^{in} \rangle$ and $\langle \delta z_R^{in} \delta z_T^{out} \rangle$ monotonically decrease and have negative values that are consistent with production by shear-driven turbulence. Other bins with $\Delta V_{SW} < -25$ km/s show the same behavior.

On the other hand, Figure 9.5 for compressive flow shows $\langle \delta z_R^{out} \delta z_T^{in} \rangle$ and $\langle \delta z_R^{in} \delta z_T^{out} \rangle$ increasing for lags shorter than 2000 s but then decreasing for larger lags. The sign is positive for shorter lags, consistent with shear-driven turbulence, but becomes negative at large enough lag. This behavior is not found in all bins with $\Delta V_{SW} > +25$ km/s wherein $\langle \delta z_R^{out} \delta z_T^{in} \rangle$ and $\langle \delta z_R^{in} \delta z_T^{out} \rangle$ are sometimes found to be negative for all lags. Thereby, results for positive ΔV_{SW} bins continue to show inconsistencies with shear-driven turbulent predictions.

In Figures 9.4 and 9.5, power law fits are made to quantities as a function of lag. Fit parameters and lag ranges are given in Table 9.2. The power law index is roughly $3/4$. This is smaller than the expected value of $4/3$ based on Lumley (1967) dimensional analysis of Kolmogorov-like cascade with linear strain (see Section 9.1.1). Departures from the Kolmogorov prediction at 1 AU are also found by Tessein et al. (2009) for the second-order velocity fluctuation structure function, whereas the corresponding structure function for the magnetic field fluctuation does satisfy the prediction. Thus, the results for $\langle \delta z_R^{out/in} \delta z_T^{in/out} \rangle$ may be another manifestation of the velocity fluctuation departure. Potentially, the lack of correspondence with a Kolmogorov cascade indicates that the turbulent state at 1 AU has not yet reached an asymptotic statistically steady state.

The anisotropy of the fluctuation energy is set by free parameters b and c where $a = 1$ without loss of generality, and we now consider how this impacts the energy cascade rate. Here, we limit the discussion to the two bins with $\Delta V_{SW} \leq -50$ km/s, which are the ones that agree best with homogeneous shear-driven turbulence. Moreover, we only consider varying b and maintain $c = 1$. We do this because b gives the anisotropy in the plane of the background velocity and gradient, which is the important one regarding linear shear.

Figure 9.6 plots ϵ_{SH}^T as a function of the free parameter b for the ΔV_{SW} bin from -100 to -75 km/s. A value of $b = 1$ corresponds to isotropy, and the value $b = 2$ corresponds to the $2 : 1$ anisotropy we use in the previous plots. The lower dashed line corresponds to ϵ_{heat} and

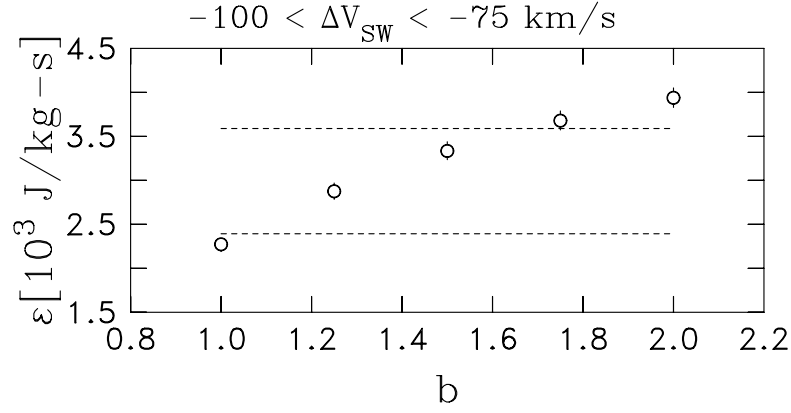


Figure 9.6: Plot of cascade rate versus in-plane fluctuation energy anisotropy parameter b for the leftmost bin in Figure 9.1. Departure of b from 1 indicates the amount of anisotropy. Lower dashed line corresponds to $\epsilon = \epsilon_{heat}$ and upper to $\epsilon = 1.5\epsilon_{heat}$. Figure reproduced from Stawarz et al. (2011).

the upper dashed line corresponds to 50% above ϵ_{heat} , which gives an approximate bound for the additional energy necessary to heat electrons. For this bin, values of b between 1.06 and 1.69 yield cascade rates in the expected range of plasma heating. For the next adjacent ΔV_{SW} bin which ranges from -75 to -50 km/s (not shown), $b = 1$ has ϵ_{SH}^T slightly greater than ϵ_{heat} , while 50% excess is reached for $b = 1.69$. Thereby, for these bins modest amounts of anisotropy are consistent with plasma heating.

9.2.2 Sorting Results by $V_{SW}T_P$

In the present analysis based on the WSOM equations, we model the anisotropy induced by the velocity shear on the fluctuations. Anisotropy associated with the direction of \mathbf{B}_0 is not considered here.

Previous studies (MacBride et al., 2005, 2008; Stawarz et al., 2009, 2010) (see Chapters 6–8) employ data that is selected without regard to shear and, therefore, average over approximately equal amounts of increasing and decreasing shear regions, as is required for this approach. These studies find that the expressions derived from the PP equations give energy cascade rates that account for expected proton heating rates. In order to determine how the results using the WSOM equations compare with these studies, we perform the Stawarz et al. (2009) analysis for bins of $V_{SW}T_P$ using the isotropic MHD third-moment expression. Stawarz et al. (2009) also obtains rates parallel and perpendicular to \mathbf{B}_0 using the hybrid MHD formalism whose sums are in better agreement with the expected total plasma heating than the rates based on the isotropic case. Here, we only compare with the isotropic case since the shear formalism does not yet include additional anisotropy effects associated with \mathbf{B}_0 .

In accordance with Chapter 7, 12 hr intervals are placed into seven overlapping $V_{SW}T_P$ bins based on the average product of the solar wind velocity and the proton temperature within the interval. For each of the $V_{SW}T_P$ bins, we again compute ϵ_{SH}^T with a 2 : 1 anisotropy, ϵ_{NOSH}^T , and ϵ_{heat} using the methods described above.

Figure 9.7 plots these three quantities against the average value of $V_{SW}T_P$ within each

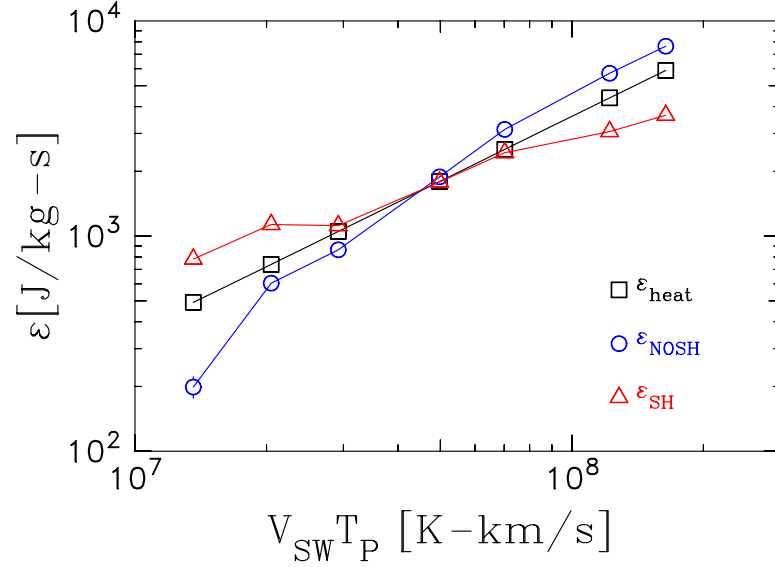


Figure 9.7: Reanalysis of Stawarz et al. (2009) heating analysis from Figure 7.3 plotting the energy cascade rate versus $V_{SW}T_P$ for 12 hr intervals and comparison with the average proton heating rate. Error bars are smaller than symbols. Table 9.3 gives the plotted data values, errors, and sample numbers. Figure reproduced from Stawarz et al. (2011).

bin, and values are given in Table 9.3. Although the shear is considered in calculating ϵ_{SH}^T for each 12 hr interval, values are averaged in Figure 9.7 only by $V_{SW}T_P$ bins. Compressions and rarefactions occur in all bins. Note that due to a small error in the selection of 12 hr intervals in the Stawarz et al. (2009) analysis and new selection criteria in applying the shear formalism, the values for ϵ_{NOSH}^T are slightly different than those shown in Figure 7.3 (see Section 7.3.1). The same conclusions that we draw in Chapter 7 can, however, be inferred from the slightly revised data. All quantities in Figure 9.7 tend to larger rates for increasing $V_{SW}T_P$. The value of ϵ_{SH}^T trends from above ϵ_{heat} in the two lowest $V_{SW}T_P$ bins to below ϵ_{heat} in the highest bins. The value of ϵ_{NOSH}^T deviates from ϵ_{heat} in the opposite sense.

In Chapter 7, we note that the two lowest bins of $V_{SW}T_P$ contain intervals mainly from the lower temperature extremes of the solar wind. Following Vasquez et al. (2007), we

Table 9.3: Rates for Figure 9.7. Table reproduced from Stawarz et al. (2011).

$V_{SW}T_P$ Range [$\times 10^7$ (km/s)K]	# Samples	ϵ_{SH}^T	ϵ_{NOSH}^T [$\times 10^3$ Joules/kg-s]	ϵ_{heat}^T
$0.2 < V_{SW}T_P < 2.0$	978	0.78 ± 0.03	0.20 ± 0.02	0.49 ± 0.00
$1.1 < V_{SW}T_P < 3.0$	1536	1.13 ± 0.04	0.60 ± 0.03	0.73 ± 0.01
$2.0 < V_{SW}T_P < 4.0$	1446	1.12 ± 0.05	0.86 ± 0.04	1.05 ± 0.01
$3.0 < V_{SW}T_P < 8.0$	1851	1.78 ± 0.04	1.89 ± 0.03	1.79 ± 0.01
$4.0 < V_{SW}T_P < 12.0$	1814	2.44 ± 0.04	3.13 ± 0.04	2.52 ± 0.02
$8.0 < V_{SW}T_P < 26.0$	991	3.06 ± 0.07	5.71 ± 0.07	4.39 ± 0.04
$12.0 < V_{SW}T_P < 40.0$	413	3.65 ± 0.15	7.63 ± 0.15	5.88 ± 0.07

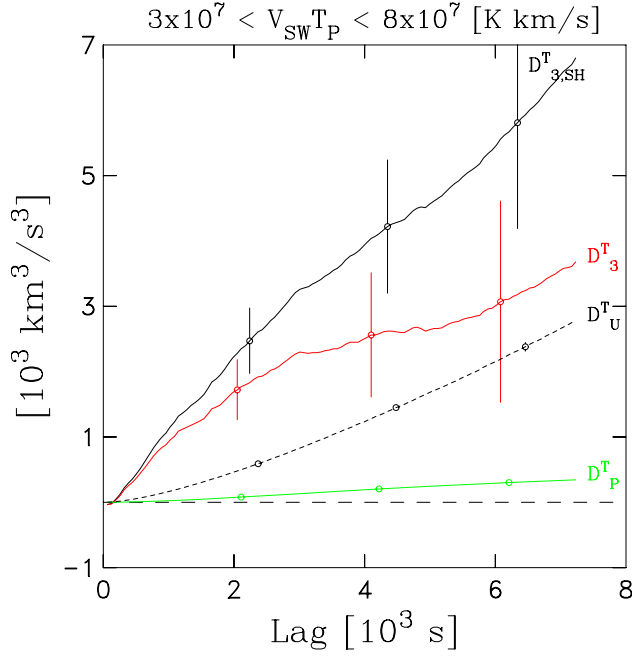


Figure 9.8: Structure function terms versus lag for the shear analysis where $V_{SW}T_P$ is near the middle of the plotted range in Figure 9.7. Corresponding plot quantities are rendered as in Figure 9.2. Figure reproduced from Stawarz et al. (2011).

suggest that ϵ_{heat} may be an overestimate in these lower bins because the analyses for ϵ_{heat} only considers V_{SW} selection to obtain the radial proton temperature gradient. Freeman and Lopez (1985) finds that cold intervals at 1 AU are more consistent with nearly adiabatic behavior. This differs significantly from the average behavior based on V_{SW} . Thereby, the deviations in the lower bins for ϵ_{NOSH}^T are not considered detrimental to the analysis for ϵ_{NOSH}^T , at least with the current knowledge of heating rates.

The two highest bins of $V_{SW}T_P$ have ϵ_{NOSH}^T greater than ϵ_{heat} . The Stawarz et al. (2009) analysis of Chapter 7 finds these intervals mostly come from fast winds that always have high T_P . Electron heating is noted by Pilipp et al. (1990) for fast winds with no discernible heating in slower wind intervals. The trend from ϵ_{NOSH}^T near ϵ_{heat} for the lower bins of $V_{SW}T_P$ to ϵ_{NOSH}^T greater than ϵ_{heat} at the highest bins is then consistent with the expectations for total plasma heating.

Two concerns are evident about the values of ϵ_{SH}^T as a function of $V_{SW}T_P$. For the two lowest $V_{SW}T_P$ bins, ϵ_{SH}^T certainly provides sufficient energization for proton heating. Are these values too high even for total plasma heating? Additionally, in the two highest bins, ϵ_{SH}^T is too small to explain even proton heating.

Figure 9.8 plots D_3^T , D_U^T , D_P^T , and $D_{3,SH}^T$ as a function of lag for the middle $V_{SW}T_P$ bin. As is expected, $D_{3,SH}^T$ is approximately linear with respect to lag. D_3^T provides the dominant contribution to the total $D_{3,SH}^T$. These results are typical of all $V_{SW}T_P$ bins except for the two largest bins where D_U^T begins to dominate the sum at long lags. Recall that D_U^T dominance at longer lags is a feature of $\Delta V_{SW} > 0$ intervals (see Figure 9.3). Combine this with the fact that ϵ_{SH}^T is not well determined for $\Delta V_{SW} > 0$ and that intervals with ΔV_{SW} of both signs are mixed together in $V_{SW}T_P$ bins, we surmise that intervals with $\Delta V_{SW} > 0$ are a likely contributor to the lack of agreement between ϵ_{SH}^T and ϵ_{heat} . Moreover, the highest bins of

$V_{SW}T_P$ contain relatively more intervals of large positive ΔV_{SW} and thus strong compression regions.

9.3 Velocity Shear Discussion

For homogeneous shear flow, the sign of the shear gradient should have no influence on the energy cascade rates. Rather only the magnitude of the shear contributes. This is clearly not found in the analyses of ACE data presented here. Rising V_{SW} intervals do not predict the same cascade rate as the corresponding falling intervals. Moreover, the predicted linear trend of total modified third-moments $D_{3,SH}^T$ in rising intervals is only met on a relatively short range of time lags which is smaller than the expected inertial range.

The most probable reason for the difference is the importance of compressional flow near sharply rising V_{SW} intervals. Corotating interaction regions where slow wind is overtaken by fast wind (see Section 3.2) have been simulated with MHD numerical codes (see Gosling and Pizzo, 1999, for a review). The simulation results show that the velocity is compressional in the interaction region, in that the velocity is deflected from the radial direction and has gradients normal to the stream interface with components along the radial direction, as well as along the tangential and northward directions. This means the background flow near the interaction region is not consistent with a homogeneous shear flow.

The differences between the actual flow and the homogeneous shear flow assumption appear to be too great to apply the present analyses accurately. The linear behavior of the structure functions at small lags for rising intervals suggest, however, that the fluctuations are non-compressive at these same scales. The background velocity may require the most attention and at least involves calculating the shear based on a determination of the actual orientation of the stream interface. In the present analyses, we assume the normal to this surface to be along the $\hat{\mathbf{T}}$ direction so that α is then generally underestimated for rising intervals.

The falling V_{SW} intervals correspond to extensive rarefactions which have rather gentle gradients of background plasma density. Conditions here are closer to ones matching a homogeneous shear flow. We find that $D_{3,SH}^T$ is linear over a considerable range of lags. Cascade rates are determined which are consistent with plasma heating rates. Thereby, the approach of homogeneous shear flow works better with rarefaction intervals.

The difference between rising and falling intervals impacts the analysis of cascade rates versus proton heating as a function of $V_{SW}T_P$. When the analysis is made with regard to shear-dependent terms, the dissipation rates fall below observed proton heating rates for the two largest $V_{SW}T_P$ bins. These bins contain the highest percentages of high speed winds and intervals of large rising V_{SW} . The inconsistency here is likely ascribed to the relative strength of compression in the rising speed intervals and its impact on the shear analysis. On the other hand, third-moment analysis without velocity detrending, which combines rising and falling intervals, finds dissipation rates in accord with observations in these same bins indicating the shear formalism is not necessary when averaging over approximately equal amounts of positive and negative shear. As we discuss in Section 9.1, the PP equations require homogeneity and the inclusion of equal amounts of increasing and decreasing wind speed results in the preservation of this condition. We, therefore, conclude the results of MacBride et al. (2008) and Stawarz et al. (2009, 2010) (see Chapters 6–8), which do not employ the shear formalism, still stand because they utilize large subsets of solar wind data containing approximately equal proportions of positive and negative velocity shear.

Chapter 10

Summary

The solar wind is a variable environment at a variety of length scales and evidence suggests turbulence is an important dynamic within this system. Aside from simply governing the evolution of fluctuations generated both at the Sun and by in situ sources such as shocks, turbulence also provides an energy transport mechanism that can account for the observed in situ heating of the solar wind.

In the solar wind, where magnetic and plasma fluctuations are coupled, turbulence is described by magnetohydrodynamics. In many ways, the magnetohydrodynamic description of a plasma is analogous to the hydrodynamic description of a fluid. In particular, third-moment expressions, of the Kolmogorov (1941b) or Yaglom (1949) forms, for the turbulent energy cascade rate are present. These expressions are among the few “exact” relationships in the field of turbulence study and do not require one to make assumptions on the underlying dynamics of the non-linear turbulent interactions. This is of particular importance in the solar wind, where these turbulent dynamics are still not well understood and appear to be far more complex than the current theories can account for. Previous studies (MacBride et al., 2005, 2008), outline the application of third-moment expressions to single spacecraft solar wind data and demonstrate the viability of such techniques.

In this thesis, we use these third-moment expressions to analyze 10 years of ACE plasma and magnetic field observations from 1 AU. We have 4 main goals motivating our analyses: analyzing the convergence of third-moments in the solar wind (see Chapter 7), determining if turbulence can account for observed proton heating rates at 1 AU (see Chapter 7), determining the dependence of the energy cascade rate on the cross-helicity (see Chapter 8), and determining if large-scale velocity shear has a significant effect when analyzing solar wind data (see Chapter 9).

We perform a third-moment analysis by dividing the 10 years of ACE data into subintervals, which we take to be statistically independent estimates with no intrinsic uncertainty. While we mainly focus our analyses on 12 hr intervals, we also experiment with the 48 hr intervals used by MacBride et al. (2008) in Chapter 7 and 6 hr intervals in Chapter 9. We find that 48 hr intervals introduce problems with convergence and 6 hr intervals are typically consistent with 12 hr intervals. Estimates of the third-moments computed from these intervals are then interpolated to a common wind speed and averaged together to obtain estimates of the third-moments from which energy cascade rates and uncertainties are derived. In Chapter 7, we perform the analyses both with and without shocks and transient drivers removed from the data. In subsequent chapters, we focus on the data with transients removed because these structures represent contaminations to the data, which are outside

the theories we are testing.

To demonstrate convergence, we analyze ACE data starting at the beginning of year 2000 in the above way, using a hybrid MHD formalism. We compute cascade rates and associated uncertainties for data sets that are incrementally increased in size from the start date, to determine how the uncertainty decreases as more data are used. We find that about a year of ACE data at 64-second cadence is needed to reduce the fractional error of an estimate of the relevant MHD third moment to below 30% when using 12 hr intervals. 48 hr intervals introduce unusual jumps in the uncertainty.

To compare proton heating rates with turbulent energy cascade rates, we use three different forms of third-moment analysis (isotropic MHD, hybrid MHD, and isotropic hydrodynamic). The data are divided into seven bins based on the product of the solar wind velocity and the proton temperature and cascade rates and uncertainties are computed. These cascade rates are then compared to proton heating rate values that are computed from Eq. (3.25), using the average $V_{SW}T_P$ value of each bin. The isotropic and hybrid MHD energy cascade rates for all but the lowest values of $V_{SW}T_P$ are consistently greater than the values needed to account for the proton heating rate. At the lowest values of $V_{SW}T_P$, we believe the third-moment energy cascade rates are likely more indicative of the true heating rates than Eq. (3.25). Overall, our results are in good agreement with the proton heating rates derived from radial gradients of proton temperatures. Although we do find a consistent excess of energy, this excess is not more than can be explained through the heating of additional species in the solar wind. Therefore, the third-order structure function analysis appears to be an effective method for measuring the turbulent cascade and in turn the combined heating rate of ions and electrons in the solar wind.

We analyze the dependence of the energy cascade on the normalized cross-helicity using the same methods described above, but this time we divide 12 hr intervals based on the absolute value of the normalized cross-helicity and on the fluctuation energy of the interval. We find the expected general decrease in the energy cascade rate as a function of normalized cross-helicity; however, periods of high cross-helicity display a weak back-transfer of energy from small to large scales within the inertial range of the turbulent spectrum. This result is persistent throughout the data without regard for data selection. It is seen (on a statistical basis) during both solar minimum and solar maximum conditions. We find that the intervals that contribute to high cross-helicity conditions are regions of relative isolation (Roberts et al., 1987) that are often characterized by the analysis of (Belcher and Davis, 1971), but can also be intervals of relatively low wind speed so long as the parcel of solar wind plasma is isolated from regions of shear. Our results are surprising and outside the range of many existing theories that predict a nominal, if small, forward cascade in regions of high cross-helicity.

In the final analysis of this thesis, we consider both the isotropic MHD formalism and newly developed WSOM third-moment expressions that include the effects of large-scale velocity shear (Wan et al., 2009). The non-shear formalism requires the fluctuations to be randomly distributed about a homogeneous mean and the presence of large-scale shears, as are seen in the solar wind, would seem to break this condition.

In order to apply the WSOM expressions to the solar wind, the background solar wind flow is taken to be in the radial direction from the Sun. Gradients across this flow are not directly measured by a single spacecraft. As the solar wind convects passed the spacecraft, different sources of wind pass the spacecraft due to the rotation of the Sun. We determine a velocity gradient from the ratio of the change in a linearly detrended background velocity

for 6 or 12 hr intervals and the distance along a heliocentric circular arc traversed at 1 AU due to solar rotation over the length of the interval. The gradient is assumed to be along the direction of solar rotation. As such, the shear is contained in the RT plane. In this approach, the tilt of the shear out of this plane is neglected, and the flow is assumed to be incompressible.

Fluctuation anisotropy, which cannot be directly assessed using single-spacecraft techniques, is another aspect in the application of the WSOM expressions. We use a set of approximations for the terms in the WSOM equations so that they are re-expressed using observed quantities and free parameters for fluctuation anisotropy. An assumed fluctuation anisotropic energy distribution averaged over lag is developed based on the hydrodynamic concept of vortex stretching of eddies associated with shear-driven turbulence. We take the induced fluctuation anisotropy to follow an ellipsoid geometry.

We apply these concepts using similar techniques to the previous analyses, with an additional linear detrending step in the application of the WSOM equations. We divide data based on the change in the linear velocity trend over the interval length, which is proportional to the magnitude of the shear. We compare isotropic MHD and WSOM cascade rates in these velocity shear bins to proton heating rates from Eq. (3.25). We observe well behaved (linear with lag) WSOM third-moments in negative shear rarefaction intervals, which produce adequate cascade rates with only a modest amount of anisotropy. The WSOM third-moments in positive shear compression regions are not as well behaved and do not match proton heating rates as well. This is likely due to compressional effects violating the assumptions of the theory. When considering shear of a particular sign, the non-shear expressions are dominated by the signal of the shear and do not produce reliable cascade rates.

We also re-perform the proton heating analysis of Chapter 7, which averages over approximately equal amounts of positive and negative shear, using the WSOM formalism. The limitations of the current application of the WSOM theory in compressional intervals, limit its effectiveness in this type of analysis. We further conclude that considering approximately equal amounts of positive and negative shear in this analysis, as well as in the analyses of Chapter 7 and 8, preserves the assumption of homogeneity and allows the non-shear formalisms to produce accurate cascade rates. We are, therefore, confident in the results of the analyses of Chapters 7 and 8.

Bibliography

- Alexandrova, O., J. Saur, C. Lacombe, A. Mangeney, J. Mitchell, S. J. Schwartz, and P. Robert, Universality of solar-wind turbulent spectrum from MHD to electron scales, *Phys. Rev. Lett.*, *103*, 165003, 2009.
- Bale, S. D., P. J. Kellogg, F. S. Mozer, T. S. Horbury, and H. Reme, Measurement of the electric fluctuation spectrum of magnetohydrodynamic turbulence, *Phys. Rev. Lett.*, *94*, 215002, 2005.
- Barnes, A., Hydromagnetic waves and turbulence in the solar wind, in *Solar System Plasma Physics*, vol. 1, edited by E. N. Parker, C. F. Kennel, and L. J. Lanzerotti, pp. 249–319, New York: North-Holland, 1979.
- Behannon, K. W., Observations of the interplanetary magnetic field between 0.46 and 1 AU by the Mariner 10 spacecraft, Ph.D. thesis, Catholic Univ. of Am., Washington, D.C., 1975.
- Belcher, J. W. and L. Davis Jr., Large-amplitude Alfvén waves in the interplanetary medium, *J. Geophys. Res.*, *76*, 3534–3563, 1971.
- Bevington, P. R., *Data Reduction and Error Analysis for the Physical Sciences*, New York: McGraw-Hill, 1969.
- Bhattacharjee, A., C. S. Ng, and S. R. Spangler, Weakly compressible magnetohydrodynamic turbulence in the solar wind and interstellar medium, *Astrophys. J.*, *494*, 409–418, 1998.
- Bieber, J. W., W. Wanner, and W. H. Matthaeus, Dominant two-dimensional solar wind turbulence with implications for cosmic ray transport, *J. Geophys. Res.*, *101*, 2511–2522, 1996.
- Biskamp, D., *Magnetohydrodynamic Turbulence*, New York: Cambridge Univ. Press, 2003.
- Biskamp, D. and W. C. Müller, Scaling properties of three-dimensional isotropic magnetohydrodynamic turbulence, *Phys. Plasmas*, *7*, 4889–4900, 2000.
- Boldyrev, S., On the spectrum of magnetohydrodynamic turbulence, *Astrophys. J.*, *626*, L37–L40, 2005.
- Boldyrev, S., Spectrum of magnetohydrodynamic turbulence, *Phys. Rev. Lett.*, *96*, 115002, 2006.
- Borovsky, J. E., Flux tube texture of the solar wind: Strands of the magnetic carpet at 1 AU?, *J. Geophys. Res.*, *113*, A08110, 2008.

- Breech, B., W. H. Matthaeus, J. Minnie, J. W. Bieber, S. Oughton, C. W. Smith, and P. A. Isenberg, Turbulence transport throughout the heliosphere, *J. Geophys. Res.*, *113*, A08105, 2008.
- Burlaga, L. F. and K. W. Ogilvie, Solar wind temperature and speed, *J. Geophys. Res.*, *78*, 2028–2034, 1973.
- Casciola, C. M., P. Gualtieri, R. Benzi, and R. Piva, Scal-by-scale budget and similarity laws for shear turbulence, *J. Fluid Mech.*, *476*, 105–114, 2003.
- Casciola, C. M., P. Gualtieri, B. Jacob, and R. Piva, The residual anisotropy at small scales in high shear turbulence, *Phys. Fluids*, *19*, 101704, 2007.
- Champagne, F. H., V. G. Harris, and S. Corrsin, Experiments on nearly homogeneous turbulent shear flows, *J. Fluid Mech.*, *41*, 81–139, 1970.
- Coleman, P. J., Jr., Hydromagnetic waves in the interplanetary plasma, *Phys. Rev. Lett.*, *17*, 207–211, 1966.
- Coleman, P. J., Jr., Turbulence, viscosity, and dissipation in the solar-wind plasma, *Astrophys. J.*, *153*, 371–388, 1968.
- Coleman, P. J., Jr., L. Davis, and C. P. Sonett, Steady component of the interplanetary magnetic field: Pioneer V, *Phys. Rev. Lett.*, *5*, 43–45, 1960.
- Dasso, S., L. J. Milano, W. H. Matthaeus, and C. W. Smith, Anisotropy in fast and slow solar wind fluctuations, *Astrophys. J. Lett.*, *635*, L181–L184, 2005.
- Davidson, P. A., *Turbulence: An Introduction for Scientists and Engineers*, New York: Oxford Univ. Press, 2004.
- Dobrowolny, M., A. Mangeney, and P. Veltri, Fully developed anisotropic hydrodynamic turbulence in interplanetary space, *Phys. Rev. Lett.*, *45*, 144–147, 1980.
- Elsässer, W. M., The hydromagnetic equations, *Phys. Rev.*, *79*, 183, 1950.
- Freeman, J. W. and R. E. Lopez, The cold solar wind, *J. Geophys. Res.*, *90*, 9885–9887, 1985.
- Frisch, U., *Turbulence*, New York: Cambridge Univ. Press, 1995.
- Fyfe, D., D. C. Montgomery, and G. Joyce, Dissipative, forced turbulence in two-dimensional magnetohydrodynamics, *J. Plasma Phys.*, *17*, 369–398, 1977.
- Gary, S. P., S. Saito, and H. Lui, Cascade of whistler turbulence: Particle-in-cell simulations, *Geophys. Res. Lett.*, *35*, L02104, 2008.
- Ghosh, S., W. H. Matthaeus, D. A. Roberts, and M. L. Goldstein, The evolution of slab fluctuations in the presence of pressure-balanced magnetic structures and velocity shears, *J. Geophys. Res.*, *103*, 23691–23704, 1998a.

- Ghosh, S., W. H. Matthaeus, D. A. Roberts, and M. L. Goldstein, Waves, structures, and the appearance of two-component turbulence in the solar wind, *J. Geophys. Res.*, *103*, 23705–23715, 1998b.
- Goldreich, P. and S. Sridhar, Toward a theory of interstellar turbulence. II. Strong Alfvénic Turbulence, *Astrophys. J.*, *438*, 763–775, 1995.
- Goldstein, M. L., D. A. Roberts, and C. A. Fitch, Properties of the fluctuating magnetic helicity in the inertial and dissipation ranges of solar wind turbulence, *J. Geophys. Res.*, *99*, 11519–11538, 1994.
- Gosling, J. T. and V. J. Pizzo, Formation and evolution of corotating interaction regions and their three dimensional structure, *Space Science Rev.*, *89*, 21–52, 1999.
- Gualtieri, P., C. M. Casciola, R. Benzi, G. Amati, and R. Piva, Scaling laws and intermittency in homogeneous shear flow, *Phys. Fluids*, *14*, 583–596, 2002.
- Hamilton, K., C. W. Smith, B. J. Vasquez, and R. J. Leamon, Anisotropies and helicities in the solar wind inertial and dissipation ranges at 1 AU, *J. Geophys. Res.*, *113*, A01106, 2008.
- Harris, V. G., J. A. H. Graham, and S. Corrsin, Further experiments in nearly homogeneous turbulent shear flow, *J. Fluid Mech.*, *81*, 657–687, 1977.
- Higdon, J. C., Density fluctuations in the interstellar medium: Evidence for anisotropic magnetogasdynamic turbulence. I - Model and astrophysical sites, *Astrophys. J.*, *285*, 109–123, 1984.
- Hinze, J. O., *Turbulence*, New York: McGraw-Hill Book Co., 1975.
- Horbury, T. S., M. A. Forman, and S. Oughton, Anisotropic scaling of magnetohydrodynamic turbulence, *Phys. Rev. Lett.*, *101*, 175005, 2008.
- Iroshnikov, P. S., Turbulence of a conducting fluid in a strong magnetic field, *Sov. Astron.*, *7*, 566–571, 1964.
- Isenberg, P. A., C. W. Smith, and W. H. Matthaeus, Turbulent heating of the distant solar wind by interstellar pickup protons, *Astrophys. J.*, *592*, 564–573, 2003.
- Kármán, T. von and L. Howarth, On the statistical theory of isotropic turbulence, *Proc. R. Soc. Lond. A*, *164*, 192–215, 1938.
- Kida, S. and M. Tanaka, Dynamics of vortical structures in a homogeneous shear flow, *J. Fluid Mech.*, *274*, 43–68, 1994.
- Kivelson, M. G. and C. T. Russell, *Introduction to Space Physics*, New York: Cambridge Univ. Press, 1995.
- Kolmogorov, A. N., The local structure of turbulence in incompressible viscous fluid for very large Reynolds numbers, *Dokl. Akad. Nauk SSSR*, *30*, 301–305, 1941a. (Reprinted in *Proc. R. Soc. London A*, *434*, 9–13, 1991.)

- Kolmogorov, A. N., Energy dissipation in locally isotropic turbulence, *Dokl. Akad. Nauk SSSR*, 32, 16–18, 1941b. (Reprinted in *Proc. R. Soc. London A*, 434, 15–17, 1991.)
- Kraichnan, R. H., Inertial range of hydromagnetic turbulence, *Phys. Fluids*, 8, 1385–1387, 1965.
- Kundu, P. K., *Fluid Mechanics*, San Diego, CA: Academic Press, 1990.
- Leamon, R. J., W. H. Matthaeus, C. W. Smith, and H. K. Wong, Contribution of cyclotron-resonant damping to kinetic dissipation of interplanetary turbulence, *Astrophys. J. Lett.*, 507, L181–L184, 1998.
- Leamon, R. J., C. W. Smith, N. F. Ness, and H. K. Wong, Dissipation range dynamics: Kinetic Alfvén waves and the importance of β_e , *J. Geophys. Res.*, 104, 22331–22344, 1999.
- Lee, M. J., J. Kim, and P. Moin, Structure of turbulence at high shear rate, *J. Fluid Mech.*, 216, 561–583, 1990.
- Lumley, J. L., Similarity and the turbulent energy spectrum, *Phys. Fluids*, 10, 855–858, 1967.
- MacBride, B. T., M. A. Forman, and C. W. Smith, Turbulence and the third moment of fluctuations: Kolmogorov’s 4/5 law and its MHD analogues in the solar wind, *Proceedings of Solar Wind 11: Connecting Sun and Heliosphere*, ESA SP-592, edited by B. Fleck and T. H. Zurbuchen, 613–616, European Space Agency, The Netherlands, 2005.
- MacBride, B. T., C. W. Smith, and M. A. Forman, The turbulent cascade at 1 AU: Energy transfer and the third-order scaling for MHD, *Astrophys. J.*, 679, 1644–1660, 2008.
- Marsch, E., Kinetic physics of the solar wind plasma, in *Physics of the Inner Heliosphere, volume 2: Particles, Waves, and Turbulence*, edited by R. Schwenn and E. Marsch, pp. 45–133, Berlin-Heidelberg: Springer-Verlag, 1991.
- Matthaeus, W. H. and M. L. Goldstein, Measurement of the rugged invariants of magnetohydrodynamic turbulence in the solar wind, *J. Geophys. Res.*, 87, 6011–6028, 1982a.
- Matthaeus, W. H. and M. L. Goldstein, Stationarity of magnetohydrodynamic fluctuations in the solar wind, *J. Geophys. Res.*, 87, 10347–10354, 1982b.
- Matthaeus, W. H. and M. L. Goldstein, Low-frequency $1/f$ noise in the interplanetary magnetic field, *Phys. Rev. Lett.*, 57, 495–498, 1986.
- Matthaeus, W. H. and Y. Zhou, Extended inertial range phenomenology of magnetohydrodynamic turbulence, *Phys. Fluids B*, 1(9), 1929–1931, 1989.
- Matthaeus, W. H., M. L. Goldstein, and D. A. Roberts, Evidence for the presence of quasi-two-dimensional nearly incompressible fluctuations in the solar wind, *J. Geophys. Res.*, 95, 20673–20683, 1990.
- Matthaeus, W. H., S. Ghosh, S. Oughton, and D. A. Roberts, Anisotropic three-dimensional MHD turbulence, *J. Geophys. Res.*, 101, 7619–7629, 1996a.
- Matthaeus, W. H., G. P. Zank, and S. Oughton, Phenomenology of hydromagnetic turbulence in a uniformly expanding medium, *J. Plasma Phys.*, 56, 659–675, 1996b.

- Matthaeus, W. H., C. W. Smith, and S. Oughton, Dynamical age of solar wind turbulence in the outer heliosphere, *J. Geophys. Res.*, *A103*, 6495–6502, 1998.
- Matthaeus, W. H., C. W. Smith, and J. W. Bieber, Correlation lengths, the ultrascale, and the spatial structure of interplanetary turbulence, *AIP Conf. Proc.*, *471*, pp. 511–514, *Solar Wind 9*, edited by S. R. Habbal, R. Esser, J. V. Hollweg and P. A. Isenberg, Am. Inst. of Phys., College Park, Md., 1999.
- Matthaeus, W. H., A. Pouquet, P. D. Mininni, P. Dmitruk, and B. Breech, Rapid alignment of velocity and magnetic field in magnetohydrodynamic turbulence, *Phys. Rev. Lett.*, *100*, 085003, 2008.
- McComas, D. J., J. L. Phillips, S. J. Bame, J. T. Gosling, B. E. Goldstein and M. Neugebauer, Ulysses solar wind observations to 56° south, *Space Sci. Rev.*, *72*, 93–98, 1995.
- McComas, D. J., S. J. Bame, P. Barker, W. C. Feldman, J. L. Phillips, P. Riley, and J. W. Griffee, Solar wind electron proton alpha monitor (SWEPAM) for the Advanced Composition Explorer, *Space Science Rev.*, *86* (1-4), 563–612, 1998.
- Mininni, P. D., D. C. Montgomery, and A. Pouquet, Numerical solutions of the three-dimensional magnetohydrodynamic α model, *Phys. Rev. E*, *71*, 046304, 2005.
- Moldwin, M. B., G. L. Siscoe, and C. J. Schrijver, Structures of the magnetic field, in *Heliophysics: Plasma Physics of the Local Cosmos*, edited by C. J. Schrijver and G. L. Siscoe, pp. 139–162, New York: Cambridge Univ. Press, 2009.
- Monin, A. S., Theory of locally isotropic turbulence, *Dokl. Akad. Nauk. SSR*, *125*, 515–518, 1959.
- Monin, A. S. and A. M. Yaglom, *Statistical Fluid Mechanics: Mechanics of Turbulence, Volume 2*, Cambridge, Mass.: MIT Press, 1975.
- Montgomery, D. C. and L. Turner, Anisotropic magnetohydrodynamic turbulence in a strong external magnetic field, *Phys. Fluids*, *24*(5), 825–831, 1981.
- Ness, N. F. and J. M. Wilcox, Sector structure of the quiet interplanetary magnetic field, *Science*, *148*, 1592–1594, 1965.
- Neugebauer, M. and C. W. Snyder, Solar plasma experiment, *Science*, *138*, 1095–1097, 1962.
- Nie, Q. and S. Tanveer, A note on the third-order structure functions in turbulence, *Proc. R. Soc. A*, *455*, 1615–1635, 1999.
- Oughton, S., E. R. Priest, and W. H. Matthaeus, The influence of a mean magnetic field on three-dimensional magnetohydrodynamic turbulence, *J. Fluid Mech.*, *280*, 95–117, 1994.
- Parker, E. N., Dynamics of the interplanetary gas and magnetic fields, *Astrophys. J.*, *128*, 664–676, 1958.
- Parker, E. N., *Interplanetary Dynamical Processes*, New York: Wiley-Interscience, 1963.

- Pilipp, W. G., H. Miggenrieder, K. H. Mühläuser, H. Rosenbauer, and R. Schwenn, Large-scale variations of the thermal electron parameters in the solar wind between 0.3 and 1 AU, *J. Geophys. Res.*, *95*, 6305–6329, 1990.
- Podesta, J. J., Dependence of solar wind power spectra on the direction of the local mean magnetic field, *Astrophys. J.*, *698*, 986–999, 2009.
- Podesta, J. J., D. A. Roberts, and M. L. Goldstein, Power spectrum of small-scale turbulent velocity fluctuations in the solar wind, *J. Geophys. Res.*, *111*, A10109, 2006.
- Podesta, J. J., D. A. Roberts, and M. L. Goldstein, Spectral exponents of kinetic and magnetic energy spectra in solar wind turbulence, *Astrophys. J.*, *664*, 543–548, 2007.
- Podesta, J. J., M. A. Forman, C. W. Smith, D. C. Elton, and Y. Malécot, Accurate estimation of third-order moments from turbulence measurements, *Nonlinear Processes in Geophysics*, *16*, 99–110, 2009.
- Politano, H. and A. Pouquet, von Kármán-Howarth equation for magnetohydrodynamics and its consequences on third-order longitudinal structure and correlation functions, *Phys. Rev. E*, *57*(1), R21–R24, 1998a.
- Politano, H. and A. Pouquet, Dynamical length scales for turbulent magnetized flow, *Geophys. Res. Lett.*, *25*, 273–276, 1998b.
- Pope, S. B., *Turbulent Flows*, New York: Cambridge Univ. Press, 2000.
- Pumir, A., Turbulence in homogeneous shear flows, *Phys. Fluids*, *8*, 3112–3127, 1996.
- Pumir, A. and B. I. Shraiman, Persistent small scale anisotropy in homogeneous shear flows, *Phys. Rev. Lett.*, *75*, 3114–3117, 1995.
- Reisenfeld, D. B., S. P. Gary, J. T. Gosling, J. T. Steinberg, D. J. McComas, B. E. Goldstein, and M. Neugebauer, Helium energetics in the high-latitude solar wind: Ulysses observations, *J. Geophys. Res.*, *106*, 5693–5708, 2001.
- Rempel, M., Creation and destruction of magnetic field, in *Heliophysics: Plasma Physics of the Local Cosmos*, edited by C. J. Schrijver and G. L. Siscoe, pp. 42–76, New York: Cambridge Univ. Press, 2009.
- Richardson, J. D. and C. W. Smith, The radial temperature profile of the solar wind, *Geophys. Res. Lett.*, *30*, 1206, 2003.
- Richardson, J. D., K. I. Paularena, A. J. Lazarus, and J. W. Belcher, Radial evolution of the solar wind from IMP 8 to Voyager 2, *Geophys. Res. Lett.*, *22*, 325–328, 1995.
- Roberts, D. A., The evolution of the spectrum of velocity fluctuations in the solar wind, *Eos Trans. AGU*, *88*(52), Fall Meet. Suppl., Abstract SH31B-06, 2007.
- Roberts, D. A., L. W. Klein, M. L. Goldstein, and W. H. Matthaeus, The nature and evolution of magnetohydrodynamic fluctuations in the solar wind: Voyager observations, *J. Geophys. Res.*, *92*, 11021–11040, 1987.

- Rogers, M. M. and P. Moin, The structure of the velocity field in homogeneous turbulent flows, *J. Fluid Mech.*, 176, 33–66, 1987.
- Sahraoui, F., M. L. Goldstein, P. Robert, and Yu. V. Khotyaintsev, Evidence of a cascade and dissipation of solar-wind turbulence at the electron gyroscale, *Phys. Rev. Lett.*, 102, 231102, 2009.
- Sahraoui, F., M. L. Goldstein, G. Belmont, P. Canu, and L. Rezeau, Three dimensional anisotropic k spectra of turbulence at subproton scales in the solar wind, *Phys. Rev. Lett.*, 105, 131101, 2010.
- Sari, J. W. and G. C. Valley, Interplanetary magnetic field power spectra: Mean field radial or perpendicular to radial, *J. Geophys. Res.*, 81, 5489–5499, 1976.
- Saito, S., S. P. Gary, H. Li, and Y. Narita, Whistler turbulence: Particle-in-cell simulations, *Phys. Plasmas*, 15, 102305, 2008.
- Schumacher, J., Relation between shear parameter and Reynolds number in statistically stationary turbulent shear flows, *Phys. Fluids*, 16, 3094–3102, 2004.
- Schumacher, J. and B. Eckhardt, On statistically stationary homogeneous shear turbulence, *Europhys. Lett.*, 52, 627–632, 2000.
- Shebalin, J. V., W. H. Matthaeus, and D. Montgomery, Anisotropy in MHD turbulence due to a mean magnetic field, *J. Plasma Phys.*, 29, 525–547, 1983.
- Shen, X. and Z. Warhaft, The anisotropy of the small scale structure in the high Reynolds number ($R_\lambda \sim 1000$) turbulent shear flow, *Phys. Fluids*, 12, 2976–2989, 2000.
- Shen, X. and Z. Warhaft, Longitudinal and transverse structure functions in sheared and unsheared wind-tunnel turbulence, *Phys. Fluids*, 14, 370–381, 2002.
- Smith, C. W., Turbulence in space plasmas, in *Heliophysics: Plasma Physics of the Local Cosmos*, edited by C. J. Schrijver and G. L. Siscoe, pp. 163–194, New York: Cambridge Univ. Press, 2009.
- Smith, C. W., M. H. Acuña, L. F. Burlaga, J. L’Heureux, N. F. Ness, and J. Scheifele, The ACE magnetic field experiment, *Space Science Rev.*, 86(1-4), 613–632, 1998.
- Smith, C. W., W. H. Matthaeus, G. P. Zank, N. F. Ness, S. Oughton, and J. D. Richardson, Heating of the low-latitude solar wind by dissipation of turbulent magnetic fluctuations, *J. Geophys. Res.*, 106, 8253–8272, 2001.
- Smith, C. W., K. Hamilton, B. J. Vasquez, and R. J. Leamon, Dependence of the dissipation range spectrum of interplanetary magnetic fluctuations on the rate of energy cascade, *Astrophys. J. Lett.*, 645, L85–L88, 2006.
- Smith, C. W., J. E. Stawarz, B. J. Vasquez, M. A. Forman, and B. T. MacBride, Turbulent cascade at 1 AU in high cross-helicity flows, *Phys. Rev. Lett.*, 103, 201101, 2009.
- Smith, E. J., A. Balogh, M. Neugebauer, and D. McComas, Ulysses observations of Alfvén waves in the southern and northern solar hemispheres, *Geophys. Res. Lett.*, 22, 3381–3384, 1995.

- Spangler, S. R., Two-dimensional magnetohydrodynamics and interstellar plasma turbulence, *Astrophys. J.*, 522, 879–896, 1999.
- Sreenivasan, K. R., On the universality of the Kolmogorov constant, *Phys. Fluids*, 7(11), 2778–2784, 1995.
- Stawarz, J. E., C. W. Smith, B. J. Vasquez, M. A. Forman, and B. T. MacBride, The turbulent cascade and proton heating in the solar wind at 1 AU, *Astrophys. J.*, 697, 1119–1127, 2009.
- Stawarz, J. E., C. W. Smith, B. J. Vasquez, M. A. Forman, and B. T. MacBride, The turbulent cascade for high cross-helicity states at 1 AU, *Astrophys. J.*, 713, 920–934, 2010.
- Stawarz, J. E., B. J. Vasquez, C. W. Smith, M. A. Forman, and J. Klewicky, Third moments and the role of anisotropy from velocity shear in the solar wind, *Astrophys. J.*, accepted 2011.
- Stawicki, O., S. P. Gary, and H. Li, Solar wind magnetic fluctuation spectra: Dispersion versus damping, *J. Geophys. Res.*, 106, 8273–8281, 2001.
- Stone, E. C., A. M. Frandsen, R. A. Mewaldt, E. R. Christian, D. Margolies, J. F. Ormes, and F. Snow, The Advanced Composition Explorer, *Space Science Rev.*, 86(1-4), 1–22, 1998.
- Stribling, T. and W. H. Matthaeus, Statistical properties of ideal three-dimensional magnetohydrodynamics, *Phys. Fluids B*, 2, 1979–1988, 1990.
- Stribling, T. and W. H. Matthaeus, Relaxation processes in a low-order three-dimensional magnetohydrodynamics model, *Phys. Fluids B*, 3, 1848–1864, 1991.
- Tennekes, H. and J. L. Lumley, *A First Course in Turbulence*, Cambridge, MA: MIT Press, 1972.
- Tessein, J. A., C. W. Smith, B. T. MacBride, W. H. Matthaeus, M. A. Forman, and J. E. Borovsky, Spectral indices for multi-dimensional interplanetary turbulence at 1 AU, *Astrophys. J.*, 692, 684–693, 2009.
- Ting, A. C., W. H. Matthaeus, and D. Montgomery, Turbulent relaxation processes in magnetohydrodynamics, *Phys. Fluids*, 29, 3261–3274, 1986.
- Toschi, F., G. Amati, S. Succi, R. Benzi, and R. Piva, Intermittency and structure functions in channel flow turbulence, *Phys. Rev. Lett.*, 82, 5044–5047, 1999.
- Totten, T. L., J. W. Freeman, and S. Arya, An empirical determination of the polytropic index for the free-streaming solar wind using Helios 1 data, *J. Geophys. Res.*, 100, 13–17, 1995.
- Townsend, A. A., *The Structure of Turbulent Shear Flow*, Cambridge, UK: Cambridge Univ. Press, 1976.
- Vasquez, B. J., C. W. Smith, K. Hamilton, B. T. MacBride, and R. J. Leamon, Evaluation of the turbulent energy cascade rates from the upper inertial range in the solar wind at 1 AU, *J. Geophys. Res.*, 112, A07101, 2007.

- Verma, M. K., D. A. Roberts, and M. L. Goldstein, Turbulent heating and temperature evolution in the solar wind plasma, *J. Geophys. Res.*, *100*, 19839–19850, 1995.
- Wan, M., S. Servidio, S. Oughton, and W. H. Matthaeus, The third-order law for increments in magnetohydrodynamic turbulence with constant shear, *Phys. Plasmas*, *16*, 090703, 2009.
- Wan, M., S. Oughton, S. Servidio, and W. H. Matthaeus, The third-order law for magnetohydrodynamic turbulence with constant shear, *Twelfth International Solar Wind Conference, AIP CP-1216*, edited by M. Maksimovic, K. Issautier, N. Meyer-Vernet, M. Moncuquet, and F. Pantellini, 172–175, American Institute of Physics, New York, 2010a.
- Wan, M., S. Servidio, S. Oughton, and W. H. Matthaeus, The third-order law for magnetohydrodynamic turbulence with shear: Numerical investigation, *Phys. Plasmas*, *17*, 052307, 2010b.
- Wenzel, K. P., R. G. Marsden, D. E. Page, and E. J. Smith, The Ulysses mission, *Astron. Astrophys. Supp.*, *92*, 207–219, 1992.
- Weygand, J. M., W. H. Matthaeus, S. Dasso, M. G. Kivelson, L. M. Kistler, and C. Mouikis, Anisotropy of the Taylor scale and the correlation scale in plasma sheet and solar wind magnetic field fluctuations, *J. Geophys. Res.*, *114*, A07213, 2009.
- Yaglom, A. M., Local structure of the temperature field in a turbulent flow, *Dokl. Akad. Nauk SSSR*, *69*, 743–746, 1949.
- Zank, G. P. and W. H. Matthaeus, Nearly incompressible fluids. II: Magnetohydrodynamics, turbulence, and waves, *Phys. Fluids*, *5*, 257–273, 1993.
- Zirker, J. B., *Sunquakes: Probing the interior of the Sun*, Baltimore, MD: Johns Hopkins Univ. Press, 2003.